

Epitaxial Growth and Ultrafast Dynamics of GeSbTe Alloys and GeTe/Sb₂Te₃ Superlattices

DISSERTATION

zur Erlangung des akademischen Grades

Dr. rer. nat.

im Fach Physik

Spezialisierung: Experimentalphysik

eingereicht an der

Mathematisch-Naturwissenschaftliche Fakultät

Humboldt-Universität zu Berlin

von

M.Sc. Valeria Bragaglia

Präsident der Humboldt-Universität zu Berlin:

Prof. Dr.-Ing. Dr. Sabine Kunst

Dekan der Mathematisch-Naturwissenschaftliche Fakultät:

Prof. Dr. Elmar Kulke

Gutachter:

(i) Prof. Dr. Henning Riechert

(ii) Prof. Dr. Simone Raoux

(iii) Prof. Dr. David Wright

Tag der mündlichen Prüfung: 13.07.2017

To my Family

Keywords: Phase-Change Materials, GeSbTe, Chalcogenide Superlattice GeTe/Sb₂Te₃, Interfaces, Molecular Beam Epitaxy, Metal-Insulator Transition, X-ray Diffraction, Raman Spectroscopy, Far-Infrared and Terahertz Spectroscopy, Ultrafast Dynamics, X-ray Absorption Spectroscopy.

Abstract

The growth by molecular beam epitaxy of Ge-Sb-Te (GST) alloys resulting in quasi-single-crystalline films with ordered configuration of intrinsic vacancies is demonstrated. It is shown how a structural characterization based on transmission electron microscopy, X-ray diffraction and density functional theory, allowed to unequivocally assess the vacancy ordering in GST samples, which was so far only predicted. The understanding of the ordering process enabled the realization of a fine tuning of the ordering degree itself, which is linked to composition and crystalline phase. A phase diagram with the different growth windows for GST is obtained. High degree of vacancy ordering in GST is also obtained through annealing and via femtosecond-pulsed laser crystallization of amorphous material deposited on a crystalline substrate, which acts as a template for the crystallization. This finding is remarkable as it demonstrates that it is possible to create a crystalline GST with ordered vacancies by using different fabrication procedures. Growth and structural characterization of GeTe/Sb₂Te₃ superlattices is also obtained. Their structure resembles that of ordered GST, with exception of the Sb and Ge layers stacking sequence.

The possibility to tune the degree of vacancy ordering in GST has been combined with a study of its transport properties. Employing global characterization methods such as XRD, Raman and Far-Infrared spectroscopy, the phase and ordering degree of the GST was assessed, and unequivocally demonstrated that vacancy ordering in GST drives the metal-insulator transition (MIT). In particular, first it is shown that by comparing electrical measurements to XRD, the transition from insulating to metallic behavior is obtained as soon as vacancies start to order. This phenomenon occurs within the cubic phase, when GST evolves from disordered to ordered. In the second part of the chapter, a combination of Far-Infrared and Raman spectroscopy is employed to investigate vibrational modes and the carrier behavior in amorphous and crystalline phases, enabling to extract activation energies for the electron conduction for both cubic and trigonal GST phases. Most important, a MIT is clearly identified to occur at the onset of the transition between the disordered and the ordered cubic phase, consistently with the electrical study.

Finally, pump/probe schemes based on optical-pump/X-ray absorption and Terahertz (THz) spectroscopy-probes have been employed to access ultrafast dynamics necessary for the understanding of switching mechanisms. The sensitivity of THz-probe to conductivity in both GST and GeTe/Sb₂Te₃ superlattices showed that the non-thermal nature of switching in superlattices is related to interface effects, and can be triggered by employing up to one order less laser fluences if compared to GST. Such result agrees with literature, in which a crystal to crystal switching of superlattice based memory cells is expected to be more efficient than GST melting, therefore enabling ultra-low energy consumption.

Selbständigkeitserklärung

Ich erkläre, dass ich die Dissertation selbständig und nur unter Verwendung der von mir gemäß §7 Abs. 3 der Promotionsordnung der Mathematisch-Naturwissenschaftlichen Fakultät, veröffentlicht im Amtlichen Mitteilungsblatt der Humboldt-Universität zu Berlin Nr. 126/2014 am 18.11.2014 angegebenen Hilfsmittel angefertigt habe.

Berlin, den

Valeria Bragaglia

List of Peer Reviewed Publications

Structural change upon annealing of amorphous GeSbTe grown on Si(111)

V. Bragaglia, B. Jenichen, A. Giussani, K. Perumal, H. Riechert, R. Calarco; *Journal of Applied Physics* 116, 054913 (2014)

Metal-Insulator Transition Driven by Vacancy Ordering in GeSbTe Phase Change Materials

V. Bragaglia, F. Arciprete, W. Zhang, A. M. Mio, E. Zallo, K. Perumal, A. Giussani, S. Cecchi, J. E. Boschker, H. Riechert, S. Privitera, E. Rimini, R. Mazzarello, R. Calarco; *Scientific Reports* 6, 23843 (2016)

Far-Infrared and Raman Spectroscopy Investigation of Phonon Modes in Amorphous and Crystalline Epitaxial GeTe-Sb₂Te₃ Alloys

V. Bragaglia, K. Holldack, J. E. Boschker, F. Arciprete, E. Zallo, T. Flissikowski, R. Calarco; *Scientific Reports* 6, 28560 (2016)

Epitaxial Ge₂Sb₂Te₅ probed by single cycle THz pulses of coherent synchrotron radiation

V. Bragaglia, A. Schnegg, R. Calarco, K. Holldack; *Applied Physics Letters* 109, 141903 (2016)

[in preparation] – Design of crystalline GeTe-Sb₂Te₃ alloys by tuning phase, composition and vacancy ordering

V. Bragaglia, F. Arciprete, R. Calarco (2017)

[in preparation] – Ultrafast dynamics investigations in MBE grown PCM superlattices

V. Bragaglia, K. Holldack, R. Calarco (2017)

[in preparation] – Thermal annealing studies of MBE grown GeTe-Sb₂Te₃ alloys with multiple interfaces

V. Bragaglia, R. Calarco (2017)

Surface reconstruction induced coincidence lattice formation between two dimensionally bonded materials and a three dimensionally bonded substrate

J. E. Boschker, J. Momand, V. Bragaglia, R. N. Wang, K. Perumal, A. Giussani, B. J. Kooi, H. Riechert, R. Calarco; *Nano Letters* 14, 3534-3538 (2014)

Laser-driven switching dynamics in phase change materials investigated by time resolved x-ray absorption spectroscopy

J. E. Boschker, R. N. Wang, V. Bragaglia, A. Giussani, R. Calarco, L. Le Guyader, M. Beye, I. Radu, K. Holldack, P. Fons, A. V. Kolobov; *Phase transitions* 88, 82-89 (2015)

Intermixing during epitaxial growth of van der Waals bonded nominal GeTe/Sb₂Te₃ superlattices

R. N. Wang, V. Bragaglia, J. E. Boschker, R. Calarco; *Crystal Growth & Design* 16, 3596-3601 (2015)

Sub-nanometre resolution of atomic motion during electronic excitation in phase-change materials

K. V. Mitrofanov, P. Fons, K. Makino, R. Terashima, T. Shimada, A. V. Kolobov, J. Tomi-naga, V. Bragaglia, A. Giussani, R. Calarco, H. Riechert, T. Sato, T. Katayama, K. Ogawa, T. Togashi, M. Yabashi, S. Wall, D. Brewes, M. Hase; *Scientific Reports* 6, 20633 (2016)

Revisiting the Local Structure in Ge-Sb-Te based Chalcogenide Superlattices

Barbara Casarin, A. Caretta, J. Momand, B.J. Kooi, M. A. Verheijen, V. Bragaglia, R. Calarco, M. Chukalina, X. Yu, J. Robertson, F. R. L. Lange, M. Wuttig, A. Redaelli, E. Varesi, F. Parmigiani, M. Malvestuto; *Scientific Reports* 6, 22353 (2016)

Interband characterization and electronic transport control of nanoscaled GeTe/Sb₂Te₃ superlattices

A. Caretta, B. Casarin, P. Di Pietro, A. Perucchi, S. Lupi, V. Bragaglia, R. Calarco, F. R. L. Lange, M. Wuttig, F. Parmigiani, M. Malvestuto; *Physical Review B* 94, 045319 (2016)

Laser induced structural transformation in chalcogenide based superlattices

E. Zallo, R. N. Wang, V. Bragaglia, R. Calarco; *Applied Physics Letters* 108, 221904 (2016)

Chemical and structural arrangement of the trigonal phase in GeSbTe thin films

A. M. Mio, S. Privitera, V. Bragaglia, F. Arciprete, C. Bongiorno, R. Calarco, E. Rimini; *Nanotechnology* 28, 065706 (2017)

Role of interfaces on the stability and electrical properties of Ge₂Sb₂Te₅ crystalline structures

A. M. Mio, S. Privitera, V. Bragaglia, F. Arciprete, S. Cecchi, G. Litrico, C. Persch, R. Calarco, E. Rimini; *Scientific Reports* (2017), under review

Conference presentations and dissemination

[EPCOS 2013 Poster presentation] – **Structural change upon annealing of amorphous GeSbTe grown on Si(111)**

V. Bragaglia, B. Jenichen, A. Giussani, K. Perumal, R. Calarco

Best poster presentation award

[DPG Conference, Dresden (2014) Oral presentation] – **Thermal annealing studies on GeSbTe alloy- films grown on Si(111) by Molecular Beam Epitaxy**

V. Bragaglia, R. N. Wang, J. E. Boschker, R. Calarco

[PSI Summer School on Condensed Matter Research (13th edition), Switzerland (2014) Poster presentation] – **Static and time - resolved investigation of electronic excitation during the phase transformation of epitaxial phase change films**

V. Bragaglia, R. N. Wang, J. E. Boschker, A. Giussani, R. Calarco, L. Le Guyader, M. Beye, I. Radu, K. Holldack, P. Fons, A. V. Kolobov

[PDI Internal Institute Seminar (2014) Oral presentation] – **Annealing of amorphous GeSbTe grown on Si(111) by Molecular Beam Epitaxy**

V. Bragaglia, B. Jenichen, A. Giussani, K. Perumal, R. Calarco

[EPCOS Marseille France (2014) Oral presentation] – **Investigation of free carriers in epitaxial GeSbTe alloys upon crystallization by means of THz spectroscopy and transport measurements**

V. Bragaglia, K. Holldack, T. Flissikowski, R. N. Wang, J. E. Boschker and R. Calarco

[Young Investigator Workshop, HZB virtual Institut, Germany (2015) Oral presentation] – **Toward dynamic investigation of epitaxially grown GeTe-Sb₂Te₃ alloys employing THz spectroscopy**

V. Bragaglia, K. Holldack, T. Flissikowski, R. N. Wang, J. E. Boschker and R. Calarco

[PULSE epitaxy summer school, France (2015) Poster presentation] – **On how to fabricate single crystalline and highly ordered GeTe-Sb₂Te₃ alloys on Si(111)**

V. Bragaglia, F. Arciprete, A. Mio, J. E. Boschker, E. Zallo, S. Cecchi, K. Holldack, S. Privitera and R. Calarco

[MRS (2015) Oral presentation] – **Terahertz and Raman investigations of epitaxial GeTe-Sb₂Te₃ alloys and GeTe/Sb₂Te₃ superlattices**

V. Bragaglia, K. Holldack, T. Flissikowski, R. N. Wang, J. E. Boschker and R. Calarco

[EMIL, Berlin (2016) Invited Talk] – **Investigation of ordering degree in GeTe-Sb₂Te₃ alloys**

V. Bragaglia

[MRS (2017) Oral presentation] – **Metal-Insulator Transition and Carrier Dynamics in GeSbTe Phase Change Materials Investigated via Electrical Transport, Terahertz and Raman Spectroscopy**

V. Bragaglia, F. Arciprete, K. Holldack, A. Schnegg and R. Calarco

List of Peer Reviewed Proposals for Beamtime Application

Title	Year	Beamline	Proposer	Results
Femtosecond dynamics of optical switching in rewritable optical media I	2014	Femtosing (UE56-1-ZPM)	Co-proposer	Chapter 5
Investigation of electronically induced structural rearrangement upon switching of GeSbTe alloys I	2014	THz-beamline	Principal investigator	Chapter 3
Investigation of electronically induced structural rearrangement upon switching of GeSbTe alloys II	2015	THz-beamline	Principal investigator	Chapters 3, 5
THz investigation of Phase Change Materials superlattices	2015	THz-beamline	Principal investigator	Chapter 5
Femtosecond dynamics of optical switching in rewritable optical media II	2016	Femtosing (UE56-1-ZPM)	Principal investigator	Not in this thesis
Time-resolved THz magneto-optical Kerr effect in $\text{Sb}_2\text{Te}_3/\text{GeTe}$ superlattices	2016	THz-beamline	Co-proposer	Not in this thesis

Contents

Acknowledgements	1
Motivation	3
1 Introduction to Phase-Change Materials	7
1.1 Phase-Change Materials Properties	7
1.2 GeSbTe Alloys: The Most Efficient Phase Change Materials	9
1.2.1 Crystalline Phases and Intrinsic Vacancies	9
1.2.2 Metal-Insulator Transition in GeSbTe Alloys	12
1.3 GeTe/Sb ₂ Te ₃ Chalcogenide Superlattices	14
1.3.1 Properties and State of the Art	16
1.4 Ultrafast Dynamics in GeSbTe alloys and Chalcogenide Superlattices	18
2 Experimental Methods and Theory	21
2.1 Thin-Film Fabrication by Molecular Beam Epitaxy	21
2.1.1 Thin-Film Crystallization/Amorphization Methods	25
2.2 Thin-Film Characterization Methods	27
2.2.1 X-Ray Diffraction	27
2.2.2 X-Ray Reflectivity	31
2.2.3 Electrical Characterization	32
2.2.4 Molecular Bonding Investigation by Raman Spectroscopy	33
2.3 Synchrotron Characterization	34
2.3.1 Investigation by Far-Infrared Spectroscopy	35
2.3.2 Experimental set-up of the Optical-pump/Terahertz-probe Experiment at Bessy II	36
2.3.3 Investigation by X-Ray Absorption Spectroscopy	39
3 Fabrication Methods and Structural Properties of Quasi-Single-Crystalline Phase Change Materials	41
3.1 Molecular Beam Epitaxy Growth of GeSbTe Alloys	41
3.1.1 Structural Characterization	42
3.1.2 Tuning of Composition and Ordering Degree	51
3.2 Fabrication of GeTe/Sb ₂ Te ₃ Chalcogenide Superlattices	65
3.3 Crystallization by Thermal Annealing of GeSbTe Alloys	69
3.4 Crystallization by Application of Femtosecond laser Pulses of GeSbTe Alloys . . .	74
3.5 Summary and Conclusions	76

4 Metal-Insulator Transition Driven by Vacancy Ordering in GeSbTe Phase Change Materials	79
4.1 Correlation of Electrical and Structural Properties	79
4.1.1 Electrical Characterization	79
4.1.2 Far-Infrared and Raman Spectroscopy Investigation	81
4.2 Summary and Conclusions	89
5 Time-Resolved Studies of Laser-Driven Dynamics	91
5.1 X-Ray Absorption Spectroscopy for Dynamic Investigations of GeSbTe Alloys . .	91
5.1.1 Determination of the Experimental Limits	96
5.2 Terahertz Spectroscopy for Dynamic Investigations of GeSbTe Alloys and Chalcogenide Superlattices	96
5.2.1 Static Terahertz Contrast between Amorphous and Crystalline GeSbTe Alloys	96
5.2.2 Time-Resolved Ultrafast Dynamics in GeSbTe Alloys	98
5.2.3 Time-Resolved Ultrafast Dynamics in Chalcogenide Superlattices	102
5.3 Summary and Conclusions	106
Conclusion and outlook	109
Appendix	113
List of Samples Prepared by Molecular Beam Epitaxy	113
Bibliography	115

Acknowledgements

Here I would like to thank all the people who supported me during the realization of this PhD work, by providing a large array of complementary skills in several techniques of material fabrication and characterization at the institute Paul-Drude-Institut and at Helmholtz-Zentrum Berlin (BESSY II).

First of all, I would like to thank as director of the Paul Drude Institute and Dr. Lutz Geelhaar as Epitaxy department head, for giving me the opportunity and the privilege to do my PhD at the institute. I would also like to thank Prof. Henning Riechert, Prof. David Wright and Prof. Simone Raoux for reviewing this thesis.

I wish to thank Dr. Raffaella Calarco as my direct supervisor in the phase change material group and Prof. Fabrizio Arciprete as my former supervisor and colleague during the PhD, for their caring leadership, the wise guidance and honest feedbacks which inspired me at both the scientific and human level.

I would like to thank all my colleagues in the phase change material group; Ruining Wang, Dr. Jos E. Boschker, Dr. Eugenio Zallo, Dr. Stefano Cecchi, for all the fruitful and never-ending scientific discussions and for making the working time so pleasant.

I'm largely indebted with Dr. K. Holldack, for introducing and supporting me in the "synchrotron world", for the technical and psychological help during the long days/nights spent for pump/probe realization at the THz beamline, and for the inspiring discussions. Thanks goes also to the UE56/1-ZPM femtoslicing beamline staff for their invaluable time and expertise during the beamtimes, in particular to Dr. Daniel Schick and Dr. Loic Le Guyader for the valuable scientific advices.

In the institute, I would like to thank all technicians in the MBE lab; Carsten Stemmler, Steffen Behnke, and Hans-Peter Schönherr for the incredible feat of keeping the Pharo II MBE machine operational; Claudia Hermann for support in the chemical lab and on the AFM setup; Dr. Bernd Jenichen for X-ray diffractometry at the institute; Dr. Timur Flissikowski and Dr. Manfred Ramsteiner for discussion and support with Raman spectroscopy; Many thanks to Mr. Andreas Hartung and Mrs. Kerstin Arnhold for the support with all the administrative tasks.

For three years of financial support and for the fruitful collaboration, I would like to acknowledge all the members in the FP7 project PASTRY (GA 317746), coordinated by Dr. Andrea Redaelli from Micron Technology Inc.

Acknowledgements

I would like also to acknowledge Prof. R. Mazzarello and W. Zhang from RWTH Aachen University for kindly providing DFT simulations; Dr. A. M. Mio, Dr. S. Privitera and Prof. E. Rimini from IMM-CNR in Catania for the TEM characterization.

Finally, I would like to thank my family and my old friends for their long-distance but very effective support. Thanks to all the new friends I met since I started this wonderful experience in Berlin for discovering and enjoying the city together, and for making my stay here so pleasant and memorable.

Motivation

The diffusion of Internet and Electronics in every aspect of daily life has reached such high levels of omnipresence, that the need of rapidly access data and disseminate information has never been felt that strongly. Although huge progress has been made in data science, revolutionizing how data is acquired, processed, compressed, stored and read, it has not been possible, yet, to condense together all the requirements for an ideal storage device, i.e. non-volatility, fast processing times, scalability, low energy consumption and costs.

The wideness and differentiated fields of applicability for storage devices, has brought to the realization of devices designed to specifically address certain needs, at the expense of other aspects. Within the current state-of-the-art, two mainstream categories of devices can be identified: Primary and secondary storage. The general common principle is that binary information is encoded by employing two physically distinctive and stable states.

The primary storage is directly accessed by the central processing unit and thus has to be very fast, usually for that purpose dynamic random access memories (DRAM) are used. Those devices are based on trapped electric charge, which is volatile and needs to be refreshed periodically with according power consumption.

Secondary storage consists of hard disk drives, optical disk drives and in general removable media. Typically such devices are slower than RAM but non-volatile, meaning that virtually no energy is needed to keep the data intact. One example is given by FLASH memory that exploits the electrical charge in a floating-gate transistor. Recently, a new storage class also called storage class memory (SCM) is targeted to enable overall performance in between that of DRAM and FLASH. Phase-change-material (PCM) based memory has gained its ground as the ideal candidate being able to fill this gap and to be used as SCM.

The PCM working principle is based on the switching between two well distinct phases, i.e. *amorphous* and *crystalline*, which are characterized by a striking change both in optical and electrical properties. Therefore these materials have been exploited during the past two decades in optical data storage applications such as rewritable CDs, DVDs, and now Blue-Ray discs, fulfilling the non-volatile requirement. More recent efforts have also been invested to utilize specifically the change in electrical properties of such materials in non-volatile electronic memory devices.

Memory cells based on PCMs (PCRAM) also benefit from a simple and straightforward architecture; the active material only needs to be connected to selector electrodes. This facilitates the integration of PCRAM into three-dimensional memory devices such as the 3D XPoint technology, which has been recently announced by Intel and Micron, introducing a fundamental step forward that might turn planar device designs obsolete in the long term.

Motivation

First production and commercialization of PCRAM has been started by Samsung in 2010. Meanwhile also Micron and IBM companies established their trade on implementations and commercialization of PCM based electrical memories.

The most technologically relevant PCMs are GeTe-Sb₂Te₃ (GST) alloys, which present an amorphous and two crystalline phases: A metastable cubic (which is the one technologically relevant), and a stable trigonal one. The alloy contains enormous number of intrinsic vacancies (up to 25 % depending on composition). The two crystalline phases, however, are similar to each other: They fundamentally consist of alternately stacked Te and Ge/Sb layers. Differences arise from these vacancies configuration depending on the phase. In the cubic crystal, they are randomly distributed in the Ge/Sb layers, while in the trigonal one, they are organized into periodic van der Waals gaps in between two adjacent Te layers^[1]. Stacking in respect of the Te atoms is cubic or rhombohedral, depending on metastable and stable phases, respectively. Vacancies configuration in respect to Ge/Sb atoms affect the total energy of the system. In addition they strongly influence conduction properties in GST and might be responsible for metal-insulator transition (MIT) attributed to disorder in the crystalline phase.

The established understanding of the GST switching process is based on melting of the metastable disordered crystal phase to obtain the amorphous one. The recrystallization is generated by annealing the amorphous phase above the crystallization temperature^[2]. In addition to this simple idea, an atomistic understanding of the switching has been for long time matter of controversy, and has found its most accredited explanation in terms of change in bonding nature between the two phases. The amorphous phase has covalent-like bonds as covalent semiconductors, whereas the crystalline phase presents a resonant bonding network. In other terms, switching is seen in terms of loss and formation of resonant bonding^[3,4], which happens on ultrafast timescales. Apart from the fascinating bonding mechanism, it is important to note that the limiting factor of PCRAM performances is the high thermal budget or the high programming current required to achieve the amorphous phase that has several implications on cost, performance and reliability.

In recent years, it was shown that PCRAM based on GeTe/Sb₂Te₃ superlattices (SLs) show enhanced switching performances in terms of power consumptions and speed. The hypothesis at the base of such low programming power is that a new switching mechanism, which circumvents pure mass melting is at play, as SLs switch between two different crystalline states: one conducting and the other highly resistive^[5]. However, the physical mechanism responsible for this low power switching is not well understood. Such chalcogenide SLs (CSLs) resemble in their structure the ordered stable GST phase, characterized by the presence of periodic vdW gaps in between building blocks alternating Te, Sb and Ge layers. The structural similitude of ordered GST alloys and CSLs shows how critical it is to better understand the fundamental role of vacancies in both conduction and switching phenomena.

Inspired by this aim, a fundamental advance in the fabrication of GST with out-of-plane stacking of ordered vacancy layers is achieved in this thesis. The degree of vacancy ordering is assessed, tuned and explicitly correlated with the MIT. Furthermore, time-resolved study of ultrafast dy-

namics in GST and CSLs are performed, in order to investigate whether it is possible to identify similarities and differences with the established switching mechanism of disordered metastable GST.

Aim and organization of this thesis

The work presented in this thesis has been carried out with two major objectives:

- Assess vacancy configuration in GST alloys, tune their ordered arrangement and contribute to the comprehension of their role in GST conduction properties.
- Access and study the ultrafast dynamics in both GST and CSLs in order to address the different physical phenomena involved in the switching.

The thesis is organized as follows:

Chapter 1 introduces PCMs with particular focus on GST and CSL heterostructures, discussing the state of research at the time of this thesis in the extent necessary to understand the results presented in this work.

Chapter 2 offers an overview of the physical background of the experimental techniques employed in the present work.

Chapter 3 deals with the fabrication of quasi-single crystalline GST achieved by employing three distinct methods such as molecular beam epitaxy (MBE), annealing treatments and application of pulsed laser beam. Structural properties of the GST are assessed through X-ray diffraction measurements (XRD), XRD simulations and electron transmission microscopy (TEM) allowing for the identification of the vacancy configuration for each produced GST sample. Particular effort is invested in the MBE fabrication method, for which a growth phase diagram is obtained.

Chapter 4 shows how electrical conduction properties of GST samples, measured by conventional low temperature transport technique, are directly compared with their structural properties. Furthermore, a combination of Raman and Far-Infrared (FIR) spectroscopy is employed to investigate vibrational modes and carrier behavior. A MIT is identified and studied.

Chapter 5 is dedicated to the description of synchrotron based pump/probe experiments accomplishment, which aimed at assessing ultrafast dynamics in both GST and CSLs. In the first part a not successful but highly instructive XAS experiment will be presented. The second part of the chapter focuses on the Terahertz spectroscopy-based investigation, in which both GST and CSLs ultrafast dynamics have been successfully accessed.

Conclusions and outlook reports the summary and the conclusions of the entire work as well as a short outlook.

1 Introduction to Phase-Change Materials

1.1 Phase-Change Materials Properties

PCM denote a class of materials that can be switched reversibly between at least an amorphous and an crystalline phase. Due to a difference in the bonding nature and atomic arrangement, a striking change in the optical and electrical properties occurs between the amorphous phase with low reflectivity and high resistance (*reset state*), and the crystalline phase with high reflectivity and low resistance (*set state*)^[2,3,6,7]. Thus information in technological applications can be stored associating a binary code to the values of optical reflectivity or resistivity of the one or the other phase.

The transition between the two phases is accomplished by heating the material by laser or current pulses leading to Joule heating^[2]. The reversible process is schematically shown in fig. 1.1 a). In the *reset state*, the amorphous phase is obtained by melting (T_m = melting temperature) the crystalline material and quenching it fast so that it lacks long-range order. The transition from crystalline to amorphous phase requires a high and short current or laser pulse that leads to a temperature higher than T_m [as shown in fig. 1.1 a)]. This is the *power limiting* process. For the opposite phase transition to the *set state*, the stable crystalline phase is obtained by heating the material above its crystallization temperature ($T_x < T_m$) for the time necessary to restore the long-range order. This requires a lower and long current or laser pulse, and this limits the *data rate* [fig. 1.1 a)].

Switching between the two phases can be triggered on a very short timescale (nanoseconds), and at a reasonable energetic cost^[9]. It is therefore not surprising that these materials have been exploited during the past two decades in optical data storage applications such as rewritable CDs, DVDs, and now Blue-Ray discs^[10]. More recent efforts have also been invested to utilize more specifically the change in electrical properties of such materials in non-volatile electronic memory devices^[11,12]. In all these applications, the most commonly used materials, as well as the most promising future candidates, are chalcogenides^[10]; this term simply refers to the chemical compounds containing one or more elements from the sixth column of the periodic table (excluding oxygen).

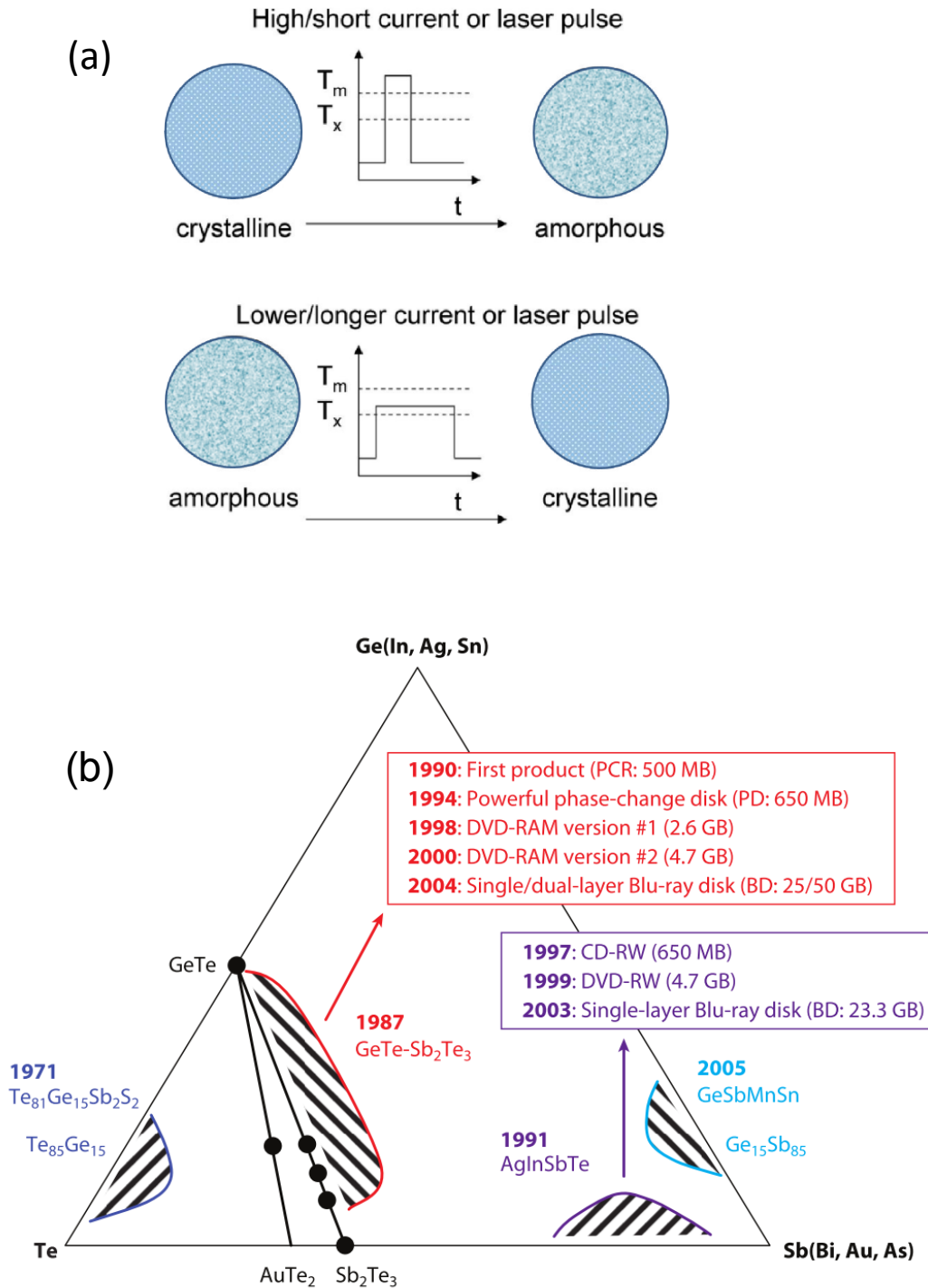


Figure 1.1: a) Schematic showing the crystallization and amorphization processes in phase change materials^[2]. b) Ternary diagram of chalcogenide compounds. Several alloys used in phase change data storage applications are indicated^[8].

1.2 GeSbTe Alloys: The Most Efficient Phase Change Materials

The technologically relevant chalcogenide alloys are gathered in one single ternary alloy diagram^[8] shown in fig. 1.1 b). Amongst different compounds exhibiting PCM properties the most interesting are Te-based alloys, typified by GeTe-Sb₂Te₃ (GST), with their different nominal compositions, as they possess at the same time all requirements needed upon switching: Large optical contrast over a wide range of wavelengths, good cyclability and short crystallization times (nanoseconds)^[2]. They lie on the pseudobinary line connecting germanium telluride (GeTe) and antimony telluride (Sb₂Te₃) binary compounds.

1.2.1 Crystalline Phases and Intrinsic Vacancies

GST alloys present an amorphous (a-) and two crystalline (x-) phases: A metastable cubic (c-GST), which is the one technologically relevant, and a stable trigonal one (t-GST). The alloy contains enormous number of intrinsic Ge/Sb-vacancies (up to 25 % depending on composition)^[13]. Cubic rocksalt structure^[14] ($Fm\bar{3}m$ space group) is usually obtained by crystallizing the amorphous thin film, grown by techniques such as sputtering. One sublattice is fully occupied by Te atoms, and the other one by a random distribution of Ge, Sb and vacancy sites (v). The stable configuration of the x- phase belongs to the rhombohedral space group ($P\bar{3}m1$ or $R\bar{3}m$)^[15].

The two x- phases, however, are similar to each other: They fundamentally consist of alternately stacked Te and Ge/Sb layers along the [111] direction. Differences arise from the vacancies configuration depending on the phase. In the cubic crystal, they are randomly distributed in the Ge/Sb layers, while in the trigonal one, they are organized into periodic van der Waals gaps (vdW) in between two adjacent Te layers^[1]. Another difference between the cubic and the trigonal phase is the stacking of the layers (with reference to the Te sublattice), which means ABCABC for c-GST and ABCBCA for t-GST.

Ab-initio calculations have suggested that spatial separation and vacancies configuration in respect to Ge/Sb atoms affect the total energy of the system^[16,17]. Further density functional theory (DFT) calculations confirmed that different metastable cubic and trigonal phases can be achieved depending on the vacancy distribution in the Ge/Sb layers^[16]. Cubic phases with partially depleted Ge/Sb layers are therefore labeled as "ordered".

In fig. 1.2 the crystal structures of cubic disordered and ordered as well as trigonal phase of GST225 are shown (see labels). The corresponding cubic and trigonal stackings are reported on the side. An intermediate ordered cubic phase is shown for seek of clarity, in order to underline the different degrees of vacancy ordering. In particular, t-GST presents the highest degree of vacancies which are distributed in such a way to form vdW gaps (see next paragraph for an explanation on the vdW gaps formation). This topic will be extensively discussed in the experimental section 3.1.1.

1 Introduction to Phase-Change Materials

The presence of vacancies strongly influence electronic properties in GST and might be responsible for the MIT attributed to disorder in the crystalline phase^[16]. The high concentration of Ge vacancies is responsible for the p-type conduction with high carrier concentration ($\sim 10^{20} \text{ cm}^{-3}$) in x-GST, which displays small band gap of $\sim 0.5 \text{ eV}$ compatible with a self-doping behavior and the Fermi level shifted close to the valence band. The a-GST instead, displays larger band gap of 0.7 eV with a Fermi level lying in the middle of the gap. In addition a-GST is characterized by a large concentration of localized states in the gap^[2], for this reason also called mobility gap.

It is worth mentioning that even if PCMs are already at the heart of optical storage technologies since many years, the fast phase change switching is subject of investigation by different dynamic experiments accessing the ultrafast time scale. A state of the art about the different studies and models can be found in the dedicated section at the end of this chapter (see section 1.4).

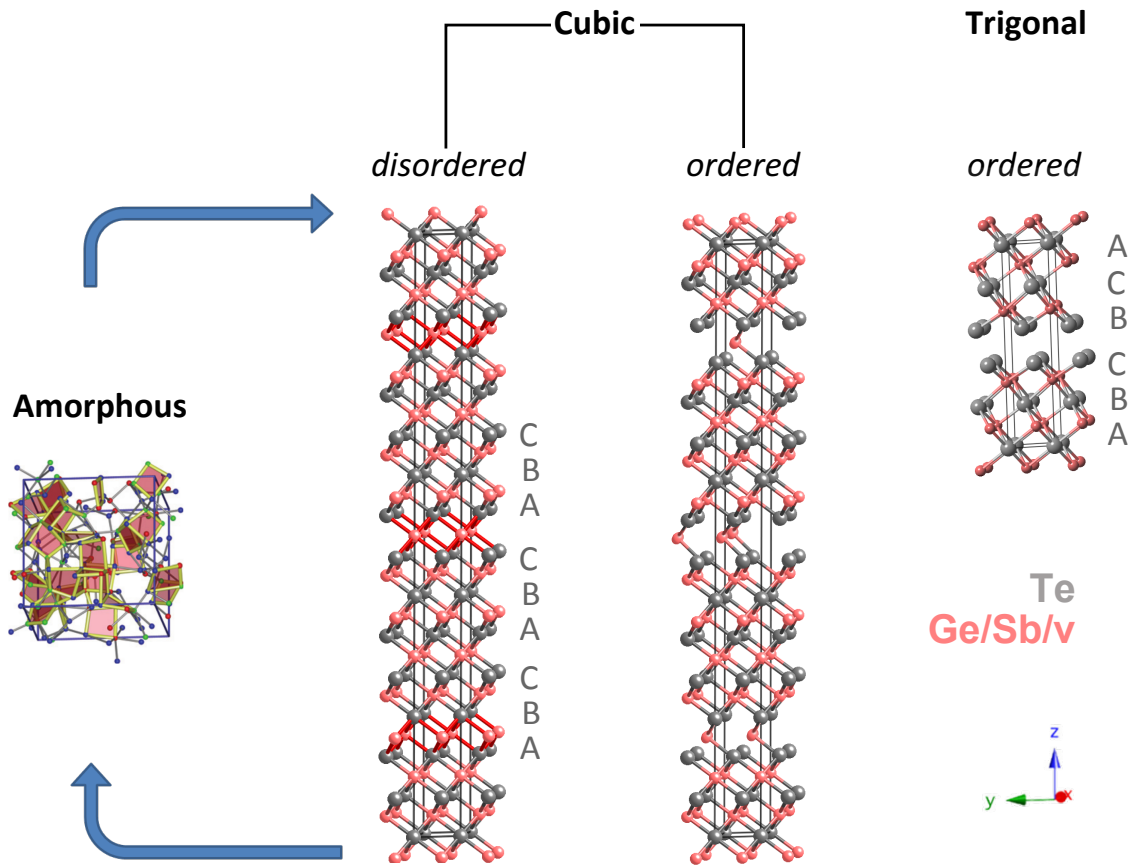


Figure 1.2: Schematic showing the crystal structures of a-^[18], c- disordered and ordered (see labels) and t-GST225. Cubic and trigonal stacking is reported on the side. The reversible a- to c-disordered GST switching is the technological employed process (blue arrows).

Regarding Resonant Bonding

Several studies based on XRD^[19] and Extended X-Ray Absorption Fine Structure spectroscopy^[19] (EXAFS) have underlined how a- and x- phases in GST present completely different bonding nature. What emerged is that a-GST shows a covalent nature of bonding (8-N rule, N being the valence). In contrast, the coordination numbers of the crystalline phases are higher than expected from the 8-N rule, and are based on the distorted, six-fold-coordinated A7 rhombohedral structure of GeTe^[3,20]. The A7 structure is a distorted NaCl structure also adopted by Sb.

To have a clear picture of the scenario, a schematic about Sb structure is used as an example (see fig. 1.3), which shows the (001) plane of a hypothetical simple cubic crystal of Sb. In this structure, each Sb atom has six nearest neighbors, but only three average p-electrons to facilitate covalent bonding between adjacent Sb atoms. On the left and right of the illustration two extreme cases can be found, but in reality, a superposition of these configurations is observed, which is schematically shown in the middle of this figure. This electron configuration has been coined as resonance bonding by Pauling. The same kind of rule applies to GeTe and GST, in which Ge, Sb, Te use electrons in their outer p-shell to create bonds, and between them they possess average number of electrons per atom which is not sufficient to create covalent or hybrid bonds with neighbors^[3]. The pronounced electron delocalization, which characterizes resonant bonding, is the cause of the significantly large increase of the electronic polarizability which is observed in many crystalline IV–VI compounds^[21]. This phenomenon is one of the fingerprints of resonance bonding.

Crystalline GST itself is characterized by this unique bonding of the p-electrons, leading to a high static dielectric constant ($\epsilon_{\infty} \sim 33$) and thus very weak effective electron interactions if compared to the amorphous phase ($\epsilon_{\infty} \sim 16$)^[3,22].

It is worth to mention that in GST, the high concentration of randomly arranged vacancies on the Ge/Sb sublattice, as well as a statistical distribution of Ge and Sb atoms on this sublattice and significant atomic displacements away from the sites of a perfect lattice (Peierls distortions^[13]) affect the overlap between adjacent p-orbitals, which impacts the electronic properties of the material^[3,13].

With this in mind, the formation and existence of vdW gaps present in the ordered crystalline structures (see fig. 1.2) can be understood by considering the resonantly bonded nature of x-GST. An ideal resonantly bonded network possesses an average of three p-electrons per atom, distributed on the resonant orbitals p_x , p_y , and p_z in all three dimensions. Therefore, a simple arithmetic argument can be applied to all the ordered stoichiometric GST compounds, taking into account the number of atoms and of p-electrons per each constituent elements in the alloy, i.e. 2, 3 and 4 p-electrons for Ge, Sb and Te, respectively. As an example, $\text{Ge}_1\text{Sb}_2\text{Te}_4$ has an average of $(1 \cdot 2 + 2 \cdot 3 + 4 \cdot 4) / 7 = 3.429$ electrons per atom; there is a surplus of 0.429 electrons per atom. After seven atomic layers, the amount of electrons in surplus amounts to three. Which means that there are enough spare electrons to fill the resonant state without the necessity for an extra layer of atoms. Therefore the vdW gap is created. $\text{Ge}_2\text{Sb}_2\text{Te}_5$ has an average of 3.33 electrons per atom, in other words a surplus of 0.33 electrons per atom. Therefore there is one vdW gap after each 9 atomic layer ($9 \times 0.33 \approx 3$). Finally, $\text{Ge}_3\text{Sb}_2\text{Te}_6$ has 3.27 electron per atom, a surplus of

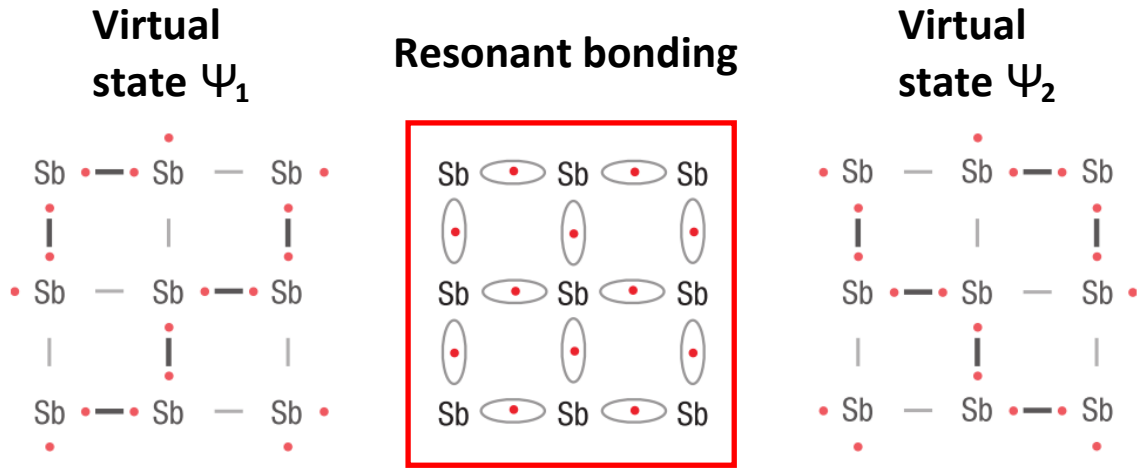


Figure 1.3: Schematic model of crystalline Sb, with its resonant bonds originating from the superposition of the two virtual states Ψ_1 and Ψ_2 [3].

0.27, therefore one vdW gap after each eleven atomic layers ($11 \times 0,273 \approx 3$). In the metastable configuration, the formation of intrinsic vacancies^[13] can be explained in a similar fashion: In a resonantly bonded network, it is favorable for the crystal to have no more than an average of three electrons per lattice site. The formation of vacancies could thus be understood as a mechanism to get rid of excess electrons.

1.2.2 Metal-Insulator Transition in GeSbTe Alloys

During the MIT, condensed phases transform from the metallic to the insulating state upon changing thermodynamic parameters such as temperature, pressure or composition, with the electrical conductivity changing by factors of 10^3 to 10^{14} over a small range of the thermodynamic parameters.

A wide range of condensed matter systems undergo the MIT. These include doped semiconductors, transition metal oxides, metal alloys and superconducting cuprates.

Different models exist to describe MIT in these materials. A part from those invoking a change of the crystal structure at the transition^[23], here we consider those describing the transition without a change in crystallographic phase. According to Anderson^[24], if the randomness in electronic state energies at different sites is large enough, electrons do not diffuse within the system, but remain localized at potential fluctuations. In general, from a semi classical point of view, we could say that electronic states involved in charge transport (i.e. those near the Fermi energy) are spatially extended or delocalized in the metal, and are localized in the insulator.

An important concept is the mobility edge, defined as the energy separating localized and delocalized states. In fig. 1.4 the density of states distribution as a function of energy for an amorphous material is shown and the mobility edges are indicated as well. The localized states tend to be on the tails of the density distribution and in these energy regions, the electronic conduction is zero at 0 K. As the disorder increases, so the mobility edges move inwards toward the center of the

band. When the Anderson criterion is reached the mobility edges meet and all states are localized. The material is then an insulator regardless of where the Fermi energy lies in the band. In other words, increasing disorder turns the delocalized electronic states at the Fermi energy into localized states^[24].

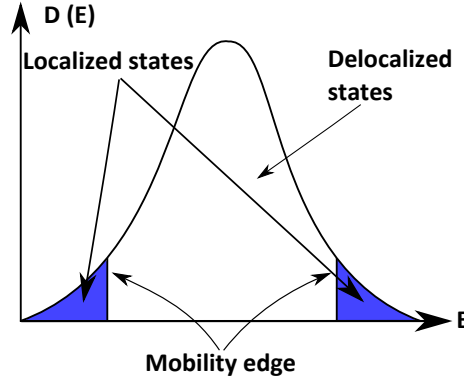


Figure 1.4: A schematic density of states in an amorphous material, showing the mobility edges separating localized and delocalized states.

A second route for the MIT to occur has been identified by Mott. His theory focuses on the electron interaction energy, such as short-range electron correlation and long-range Coulomb interactions, and disorder effects are completely neglected. MIT arises if correlation exceeds the Fermi energy^[25]. Two important concepts were first predicted by Mott and are the existence of a critical conductivity (or resistivity) for the metals at the MIT transition point, and a vanishing conductivity (diverging resistivity) in the limit of 0 K. For real systems, it is often the case that in the same system, both correlations and disorder are significant, making a clear distinction between the two cases not straightforward.

In GST alloys, in addition to the fast and reversible switching from a- to x- phase, experimental results on polycrystalline GST (poly-GST) films have evidenced a MIT^[26] in the crystalline state. In the study of Siegrist *et al.*^[26], the change of resistivity as function of temperature has been studied, and evidence of a MIT has been given. The latter has been attributed to disorder (Anderson MIT) based on theoretical considerations combined to specific assumptions on the material system. Subsequently, *ab initio* simulations based on DFT and molecular dynamics (MD), have indicated that the insulating behavior stems from the localization of electronic states around vacancy clusters, whereas the transition to the metallic state is induced by the ordering of vacancies into layers^[16].

So far, only poly-GST has been investigated and no experimental evidence of the influence of formation of vdW gaps through vacancy ordering on the MIT has been given. In addition, although the phase transformation between c- to t-GST has been excluded as cause of the MIT, the experimental evidence was not enough to unequivocally understand in which crystalline phase MIT takes place has not been given.

One of the goals of this thesis has been to fabricate quasi-single-crystalline material that facilitates the direct experimental observation of different degrees of vacancy ordering, to investigate the MIT in GST, as will be shown in chapters 3.1.1 and 4.

1.3 *GeTe/Sb₂Te₃ Chalcogenide Superlattices*

CSL have been shortly mentioned in the motivation to this thesis work, and deserve to be presented in more detail.

The concept behind a superlattice structure is to stack different materials of few nanometer thickness on top of each other in order to combine their existing properties, or give rise to new superior properties that are not found in the separate materials, as for instance bandgap engineering. For CSL, the goal is that of improving memory performance.

In recent years it has been shown that memory cells based on CSLs with alternating layers of GeTe and Sb₂Te₃ layers display dramatically improved performance in terms of reduced switching energies (up to one order of magnitude if compared to PCMs), improved write-erase cycle lifetimes (more than an order of magnitude compared to PCMs), and faster switching speed^[5], if compared to conventional PCM based memories.

Although the properties of Sb₂Te₃ and GeTe are not specifically investigated in this thesis work, these compounds are still relevant as one of the component of the superlattice structures.

Antimony Telluride

Sb₂Te₃ lies on one of the extremities in the pseudo-binary line shown in fig. 1.1 b), encompassing most of the technologically relevant phase change materials. But by itself, Sb₂Te₃ is not considered to be one of them: Its low crystallization temperature (~ 70 °C) makes the amorphous phase unstable and unreliable for technological applications.

Sb₂Te₃, like GST, is a resonantly bonded material. It belongs to the $R\bar{3}m$ space group. The structure of Sb₂Te₃ is illustrated in fig. 1.5. In the densely packed (111) planes (in cubic notation), each molecular block of five atomic layers [also called quintuple layers (QL)] is separated from the neighbor blocks by an empty layer on the Sb sublattice. The facing Te atoms on each side of the vacant layer are separated by vdW gaps. The Te sublattice follows an hexagonal stacking in the out-of-plane axis (ABCBCACAB).

As already discussed for GST, the presence of vdW gaps can be easily understood by considering that Sb₂Te₃ is indeed a resonantly bonded material. The average number of p-electrons in Sb₂Te₃ is 3.6 electrons per atom, i.e. 0.6 electrons surplus per atom. This means that each five atomic layers gives 3 surplus electrons, therefore there are enough spare electrons to fill the resonant state, without the necessity for an extra layer of atoms and to create a vdW gap.

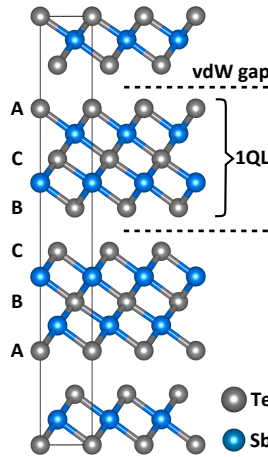


Figure 1.5: Scale model of the crystalline Sb₂Te₃ structure. The stacking sequence for the Te sublattice is indicated on the left-hand side. vdW gaps and the size of one QL is highlighted.

The Sb-Te bond lengths are not uniform in Sb₂Te₃: The bonds at the edge of the block, closer to the vdW gaps, are shorter than those near the middle of the block. Since the bonds distortion is symmetrical at both edges of the blocks, Sb₂Te₃ is not a ferroelectric material.

Sb₂Te₃ possess interesting properties, such as the thermoelectric effect. In addition, because of the vdW gaps, the thermal conductivity is highly anisotropic and the heat conduction via phonons in the out-of-plane direction is very low^[27]. It has also been proposed that the resonant bonds themselves contribute to the low thermal conductivity^[28]: The atoms interact with each other on a longer range within the resonant network, but because they are not perfectly periodically spaced, it induces anharmonic phonon scattering.

Low thermal conduction is also beneficial for phase change memory applications, because it ensures that heat is confined in the active area, and minimizes cross-talk between neighboring cells. From this point of view, ordered GST structures or CSLs have a clear advantage over GeTe or disordered metastable GST because of the presence of vdW gaps.

Germanium Telluride

Despite its very simple stoichiometry, GeTe is a quite complex compound from the fundamental point of view. In its amorphous phase, a-GeTe is covalently bonded as commonly found for amorphous semiconductors^[29]. It reflects also in its electrical and optical properties. Instead, if we consider its crystalline phase (x-GeTe), it presents extraordinary properties.

Two crystalline phases can be found: A cubic one existing at high temperature (~ 720 K), called β -GeTe phase; and a rhombohedral structure called α -GeTe at lower temperature.

1 Introduction to Phase-Change Materials

GeTe has attracted a lot of attention both from a fundamental and technological perspective as a thermoelectric^[30,31], ferroelectric^[32,33], and phase-change material^[34,35]. Recently, it has been demonstrated that it owns a giant bulk Rashba effect that paves the way towards novel spintronic devices^[36].

All this properties can be related to two main phenomena which characterize the crystalline structures: The resonant bonding (see paragraph "Resonant bonding" in 1.2.1), and the Peierls distortion. The last one implies the formation of alternated short strong bonds and longer weaker ones^[22,37] in the GeTe cell. It has been shown to be favorable for these short and long bonds to be distributed in an ordered fashion, into layers in the [111] direction^[38]. As a result, the crystal is elongated in the [111] direction, leading to a rhombohedral distortion of the cubic rocksalt unit cell. All details about growth and optimization of epitaxial GeTe films by our group can be found in R. Wang *et al.*^[39,40].

1.3.1 Properties and State of the Art

As opposed to conventional PCM, in which the transformation occurs between two phases (amorphous and crystalline), in CSLs it happens between two states within two different crystalline states: One conducting and the other highly resistive, that will be labeled as low resistance state (*LRS*) and a high resistance state (*HRS*), respectively, in order to avoid confusion with the *set* and *reset* states of conventional PCMs. The key point here, is that the electrical switching in CSLs happens on a "non-thermal" fashion, meaning that no melting process is involved, as confirmed by the maintained SL structure after several cycles shown experimentally^[5]. However, the physical mechanism responsible for this low energy switching is not well understood.

Chong *et al.*^[41] were the first reporting about SLs. They tested amorphous GeTe/Sb₂Te₃ SLs after annealing, with optical data storage applications in mind. They found shorter crystallization time under optical excitation, compared to the homogeneous GST alloy of the same average composition. Similar experiments were conducted by Cao and Quiang,^[42] where lower activation energy for crystallization were obtained by differential scanning calorimetry. Chong *et al.*^[43] argued that the decrease of the switching energies has to be ascribed to a decrease of thermal conductivity, which effectively increases the temperature in the memory cell.

Later, Simpson *et al.*^[5] suggest that there may be more than just thermal conductivity at play. Using physical vapor deposition, CSLs with 1 nm thin amorphous GeTe sublayers sandwiched between 4 nm thick crystalline Sb₂Te₃ blocks were grown and fully crystallized by annealing. Such structures showed reduced switching energies, improved write-erase cycle lifetimes, and faster switching speeds. These improvements are attributed to the natural tendency for the intercalated Sb₂Te₃ layers to texture themselves in the out-of-plane direction, offering a template for the crystallization of GeTe. Thus, the configurational entropy difference between the two phases is reduced, enabling the switching between them without undergoing melting. The device-damaging long-range atomic diffusion^[44,45] is also greatly suppressed.

Interesting appears the possibility of a "non-thermal" route in the optical switching process. With "non-thermal" it is meant excitation process that induces a negligible temperature change, differently from a melting process. One of several examples^[46–49] is the study of Makino *et al.*^[50] in which crystallization of the above mentioned CSLs has been induced by using two optical pulses which coherently excite optical phonons. In other words, the phase change from amorphous into crystalline states can be manipulated by controlling atomic motions through selectively exciting a vibrational mode that involves Ge atoms, under specific pump pulses conditions^[50,51]. "Non-thermal" switching is expected to be by far more efficient than melting and to enable ultra-low energy consumption, at least one order of magnitude less than conventional PCM memories.

A consistent breakthrough in the realization of CSLs with high degree of structural order, leading to a reduction of entropic losses during switching, has been done by our group, which has pioneered the growth of epitaxial CSLs consisting of alternating layers of GeTe and Sb₂Te₃, with the smallest layer thickness of about 1 unit cell of GeTe and of Sb₂Te₃ in the [111] direction with interface and surface roughness of 1.4 and 1 nm, respectively. Single out-of-plane and in-plane orientation was achieved^[52–54]. From High-Angle Annular Dark Field Scanning Transmission Electron Microscopy (HAADF-STEM) measurements^[54] it has been demonstrated that GeTe-Sb₂Te₃ superlattices are actually a vdW heterostructure of Sb₂Te₃ and rhombohedral GST, which is in striking contradiction with the previously proposed models in the literature^[48]. These GST layers are formed due to the bonding dimensionality of the superlattice sublayers, as GeTe prefers to be 3D bonded within the Sb₂Te₃ block and not adjacent to a vdW gap. In other words, GeTe and Sb₂Te₃ undergo intermixing which lowers the system energy. The question of intermixing is very important because there are several models describing how switching occurs in the CSL, and some of them are based on the assumption that there is a well defined interface between GeTe and Sb₂Te₃.

A very important point to underline, which goes behind the different mentioned studies of the switching mechanism, is that so far the atomic structures of the *LRS* and *HRS* are still not fully agreed by different groups producing CSLs.

The four leading atomic models describing CSL structures are reproduced in fig. 1.6^[48]. All four proposed structures can be seen as vdW gaps (formed between Te-Te layers) separating blocks of Ge, Sb and Te layers. Differences arise in the layers distribution and block sizes. As a common feature, Sb layers tend to be at the extremes of the unit cell (black rectangle) in order to form Sb₂Te₃ block, and Ge layers in the center, forming GeTe block. It is important to point out that based on our previous studies^[52,54], the model that best corresponds to the CSLs samples grown and studied in this thesis work is the Kooi model^[15,54], with its characteristic -[Te-Sb-Te] endpoints encapsulating the GeTe layers. Structures similar to the ferro-GeTe model cannot be excluded in proximity of defective vdW layers but the Kooi structure remains the more representative one.

Therefore, it is not surprising that interpretations of the results concerning the switching of CSLs can in some cases be in disagreement between groups. For instance, it has to be considered that different fabrication methods or recipes could lead to CSLs which are better described by a model structure among the four depicted in fig. 1.6.

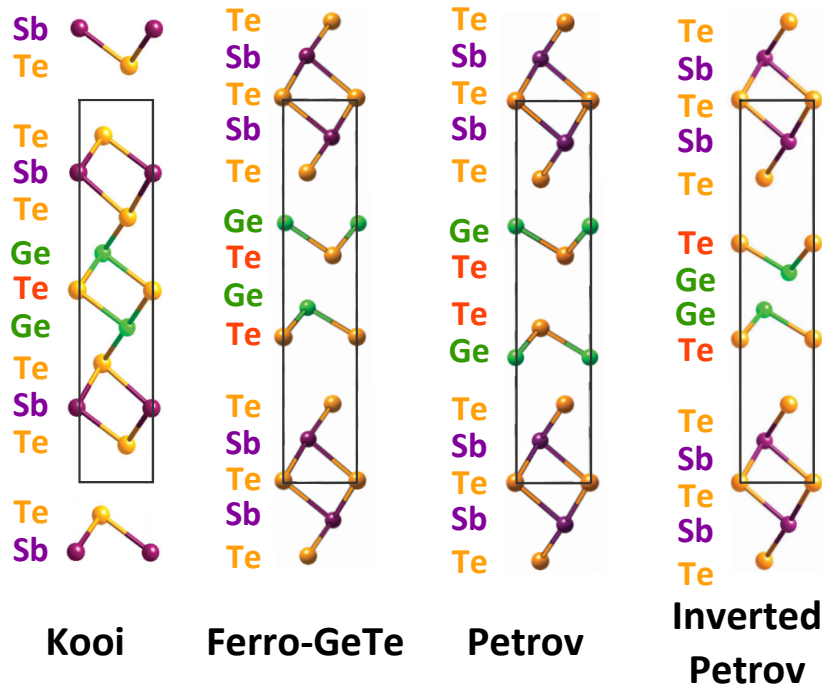


Figure 1.6: Proposed structures for CSL with 2 bilayers of GeTe between Sb_2Te_3 blocks. Figure are adapted from Tominaga *et al.*^[48].

As an example of the last point, in a recent study by Yu and Robertson^[49] a further investigation describing the motion of an atomic layer between the *LRS* and *HRS* in CSLs has been proposed. It is based on the two most accredited switching models proposed in the PCM community: Model 1 is proposed by Tominaga *et al.* and happens between a Ferro *LRS* and an Inverted-Petrov structure in *HRS*^[48]. Model 2 is proposed by Ohyanagi *et al.* and is a transition between a Petrov *LRS* and an Inverted-Petrov *HRS*^[47]. As a result of this study, it has been shown that the main transition is actually a vertical flip of a Ge layer through a Te layer, followed by a lateral motion of GeTe sublayer to the final, low energy structure^[49].

On the other hand, a very recent study based on EXAFS and TEM^[55] prospects a more complex switching mechanism than an oversimplified atomic Ge flipping for epitaxial CSLs interfacial structures. The observed distortion of the lattice, the vdW gap shift and the Ge(Sb) intermixing should be considered as worthwhile features of these SLs, since they would possibly affect the phase-change performances in terms of electrical switching and activation energy.

1.4 Ultrafast Dynamics in GeSbTe alloys and Chalcogenide Superlattices

Even if PCMs have been at the heart of optical storage technologies since many years, the phase change mechanism driving the reversible transformation from the crystalline to the amorphous state has been matter of controversy in the literature.

It has to be clarified that in electrical memories, the switching process is achieved by the applica-

tion of electrical pulses (nanosecond range)^[2,56]. Nevertheless, different mechanisms contributing to the switching, such as the threshold switching^[2,57], which is at the base of PCM electrical switching, is occurring in the a-phase and prior to the a- to c-phase transition, and is governed by electron-phonon coupling and relaxation processes occurring on the timescale of several hundred femtoseconds (fs)^[57]. Such processes are clearly "non-thermal" and are too fast for an electrical probe. Therefore, the established understanding of the switching process, based on melting of the c- phase to obtain the a- one and recrystallization by annealing of the a-phase above the crystallization temperature^[2] presents limitations and does not account for the bonding nature of PCM and others possible ultrafast "non-thermal" switching paths which may act as precursors to the thermal one, or even happen independently from one each other.

Therefore, dynamical studies on an ultra-fast timescale result necessary.

Possibilities to access ultrafast timescales are given by full optical-pump/probes or optical-pump/X-ray probe schemes and can be found in the literature^[4,58–60] and lead to the formulation of different switching mechanisms. Two mainstream explanations can be distinguished.

It has been suggested that the Ge ions coordination changes through an "umbrella flip" transition, which modifies both the structure and optical properties^[61]. As only a subset of bonds would change, this type of mechanism has the potential to be very fast and non-thermal. However, the thermal stability of the umbrella flip model has been questioned and later work has shown that coordination changes alone are insufficient to explain the observed changes in the optical properties^[3,62].

The latest alternative and most accredited explanation of the optical contrast upon switching has been explained in terms of resonant bonds in the crystalline state^[3,62].

In a recent work of L. Waldecker *et al.*^[4] a direct measurements of the structural and optical dielectric properties during the photo-triggered amorphization of GST using a combination of time-resolved femtosecond optical spectroscopy and electron diffraction in the single-shot regime, has been provided. It has been demonstrated that femtosecond optical excitation of x-GST directly removes electrons from resonantly bonded states as evidenced by the immediate decrease in the dielectric function. This non-thermal femtosecond change in the optical properties does not coincide with a change in crystallinity. Therefore resonant bonding perturbation has been proposed as a non-thermal cause of the switching, in line with previous studies^[3,62].

Our approach within the mentioned scenario, is based on the unique capability to grow epitaxial phase change materials. Epitaxial PCM with respect to those produced by sputtering offer decisive advantages. They display high structural quality and single out-of-plane and in-plane orientation, thus reducing the effect of imperfections at grain boundaries; a further advantage is that ideally a material with such high perfection facilitates the interpretation of experimental results, that can be directly associated to the grown structure, through an atomistic picture.

Optical switching process of GST epitaxial films using picosecond laser pulses has been investigated and it has been found that the amorphization process takes place in a single or in multiple steps, while the re-crystallization process always takes place in multiple steps^[63]. It was clearly demonstrated, by employing nanofocus high-resolution XRD on the samples before and after ap-

1 Introduction to Phase-Change Materials

plication of femtosecond laser pulses^[64], that it is possible to reversibly switch back and forth the epitaxial layers. Furthermore, epitaxial GST has been studied and coherent phonons (CPs) generated by laser pulses on the fs-scale have been proposed as a means to achieve ultrafast, non-thermal switching in PCM^[59].

Another possibility to access ultrafast timescales is given by employing pump/probe schemes exploiting THz radiation, which is particularly sensitive to conductivity changes in the materials. Only few dynamic THz studies on poly-GST alloys have been conducted so far^[60,65]. In Shu *et al.*^[60], time-resolved ultrafast electric field-driven response of c- and a-GST films has been measured all-optically, pumping with single-cycle THz pulses. Field-induced heating of the carrier systems has been observed within picosecond-time-scale (0-10 ps).

Similar arguments hold for epitaxial CSLs, which only undergo switching through "non-thermal" path. The understanding and control of non-thermal switching triggered by different excitation stimulus is of fundamental importance for technological applications, since it is expected to be by far more efficient than melting and to enable ultra-low energy consumption (at least one order of magnitude less than conventional PCM memories). CSLs high degree of structural quality^[52,53,55] might facilitate the interpretation of experimental results (see paragraph 1.3.1), together with the comparison to the switching of ordered GST, that presents similitudes in the structure in terms of vdW gaps presence in between building block alternating Te, Sb and Ge.

2 Experimental Methods and Theory

The current chapter presents a description of the different samples fabrication methods, with focus on molecular beam epitaxy (MBE). The characterization techniques of interest for static structural investigation such as Raman and Far-Infrared (FIR) spectroscopy, X-ray diffraction (XRD) and electrical measurement are discussed. Eventually, the synchrotron based experiments for time-resolved investigations are presented. They are based on X-ray absorption (XAS) and Terahertz (THz) spectroscopy.

2.1 *Thin-Film Fabrication by Molecular Beam Epitaxy*

MBE is a deposition technique which allows the oriented growth of a crystal on the single crystal surface of a different material. The process of oriented growth of a crystal starting from a crystalline template, is defined as epitaxy.

The major characteristic of MBE operation consist in the evaporation of atomic or molecular beams from highest purity effusion sources, on a heated substrate under ultrahigh vacuum (UHV) conditions of about 10^{-11} Torr. The UHV condition ensures clean growth environment, and high mean free path of the atomic/molecular beam that far exceeds the dimensions of the chamber, which results in working state of *free molecular flow* regime. In such regime, only interaction of the evaporated species and the substrate are relevant, while interaction within atoms and molecules in the fluxes are ideally neglectable. To initiate the deposition, the substrate surface is simply exposed to the flux of material emitted by the cells.

MBE enables the growth of very high purity and high quality crystalline structures in a controlled fashion. It is therefore a method most successful in the fabrication of low-dimensional structures such as quantum dots, nanowires, quantum wells, and thin films. The applications for these structures in optoelectronics are innumerable^[66–68].

MBE deposition is usually performed at elevated substrate temperatures, where the atoms become more mobile on the surface. Atomic or molecular species impinging on the hot substrate might get chemisorbed or physisorbed on the surface and different phenomena can be considered happening: desorption, adsorption, incorporation and diffusion. The interplay between these mechanisms is regulated by rate equations which take into account the growth kinetics. In non obvious fashion, specific free energy conditions for the system determine the equilibrium of the mentioned phenomena^[69].

2 Experimental Methods and Theory

The success in an MBE growth strongly depends on careful choice of the sources fluxes, the heating of the substrate, and the preparation of the substrate. A fine control of the mentioned parameters allows, in most of the cases, that the impinging atoms or molecules diffuse on the surface and find a preferred site to be adsorbed. Using a crystalline substrate, the position of these favorable sites will be defined by its crystalline structure at the exposed surface. If the deposited material is also crystalline, its orientation will be inherited from the substrate: An epitaxial relationship is established between the film and the substrate. With enough heat supplied to the substrate, the rejected atoms are desorbed and captured by the cryogenically cooled chamber shroud, ensuring low UHV background pressure.

Two distinct cases of epitaxial growth can be distinguished: If the crystalline film is grown on a substrate of the same material, therefore with the same lattice parameter, then the process is called *homoeptitaxy*; instead, when the two crystals are not the same material, and the lattice parameters differ, the process is called *heteroeptitaxy*. In the latter case, a lattice *mismatch* can be defined depending on the lattice parameters of substrate and grown film (a_{sub} and a_{film}):

$$m = \frac{a_{\text{sub}} - a_{\text{film}}}{a_{\text{sub}}}$$

When lattice mismatch is reasonably low ($\leq 7\%$), the first few atomic layers of the deposited film will strain themselves to adapt to the substrate lattice, growing pseudomorphically. As the thickness of deposited material increases, elastic energy is accumulated due to the stress in the film. After a certain critical thickness, the epilayer starts to release stress by the formation of misfit dislocations. The value of the critical thickness is roughly inversely proportional to the mismatch. Instead, when the mismatch between the substrate and the film is too large ($\geq 8\%$), the critical thickness for misfit dislocation formation approaches the order of one single atomic layer^[70]. In this case, the two lattices cannot be matched anymore, and misfit dislocations are formed directly at the interface, in order to immediately relax the film. Another case, named domain matching epitaxy, occurs when the epilayer attempt to match an integer number of its unit cell with more distant lattice points of the substrate, to form epitaxial domains. As a result, the film is not fully relaxed; there is generally some residual domain mismatch, but it is typically much smaller compared to the lattice mismatch ($\leq 1\%$).

Mismatch and interaction between atoms determines different growth processes: If the interactions between atoms in consecutive layers is stronger than the one between atoms in the same layer, then a two-dimensional (2D) layer-by-layer Frank-van der Merwe growth is favorable. In contrast, nucleation and coalescence of isolated three-dimensional islands are more likely when interactions between atoms in the same material layer are dominant (Volmer-Weber process). In this case the forming film is much rougher. The third possibility is the so-called Stranski-Krastanov process, where growth initially starts in a layer-by-layer fashion, until three-dimensional (3D) islands are formed on top of the epilayer, due to the accumulated strain in the film once a certain critical thickness is reached^[69]. A schematic of the three scenarios is illustrated in fig. 2.1.

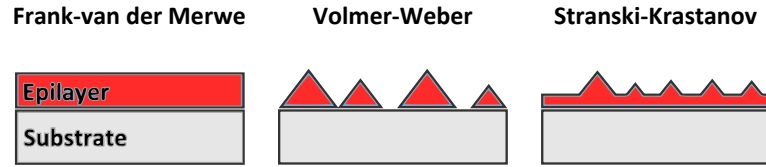


Figure 2.1: Schematic diagram showing the Frank-van der Merwe, Volmer-Weber, and Stranski-Krastanov growth modes for heteroepitaxy.

The MBE system used in the framework of this thesis was custom-built by CreaTecFischer & Co. GmbH. This system is composed of three vacuum chambers of progressive quality. The first chamber is the load-lock, used for transferring samples in and out of the system. This chamber is pumped down to 10^{-8} mbar and the stage can be heated for degassing. Furthermore, it is equipped with a RF sputtering unit that can be used to apply protective capping layers (Si_3N_4 , ZnS-SiO_2 , TiN , or W) on the samples before exposing them to the atmospheric pressure. The second part is the transfer chamber, where the substrate can be further baked and degassed, at a pressure of 10^{-9} mbar. It also acts as a buffer zone before the substrate is introduced into the UHV growth chamber at 10^{-10} mbar. The growth chamber hosts several ports occupied by Ge, Sb, and Te cells. For flux calibration and desorption studies, the chamber is equipped with a molecular beam flux monitor, an atmospheric quadrupole mass spectrometer (QMS), and an line-of-sight QMS. Unfortunately, the QMS was out of commission and could not be used for this thesis. A reflection high-energy electron diffraction (RHEED) system is also integrated allowing the *in situ* study of the crystal growth.

High-Energy Electron Diffraction

In this thesis work, RHEED has been particularly useful to monitor in real-time and *in situ*, the substrate reconstruction state prior to the growth and the different growth stages in terms of crystalline quality.

RHEED equipment is composed of a 5-20 keV electron gun which provides an electron beam focused on the sample surface at grazing angles (1° - 3°). The beam is diffracted by the surface and collected by a phosphor-coated screen on the opposite side of the electron gun. The visible patterns are useful for analyzing the surface symmetries and reconstructions, detecting a transition in the dimensionality of the growth and measuring growth rates. The small effective penetration depth of the impinging electrons, due to the grazing incidence angle, makes RHEED a surface sensitive investigation technique.

The working principle is based on the scattering of the impinging electrons with the electron cloud of the nuclei on the sample surface, which lead to waves interference effects that are constructive only in certain directions depending on the crystalline structure of the surface. RHEED patterns are produced on the screen allowing to deduce properties about the reciprocal space lattice (and therefore the direct) by employing an Ewald sphere construction (fig. 2.2). Ewald sphere construction and reciprocal-direct lattice relations for ideal bulk crystals are discussed in

section 2.2. In this specific case, the reciprocal lattice of a crystal surface consists of a series of infinite rods perpendicular to the surface, having their origin in the lattice points [see fig. 2.3 a)]. Corresponding 3D Ewald construction is illustrated in fig. 2.2.

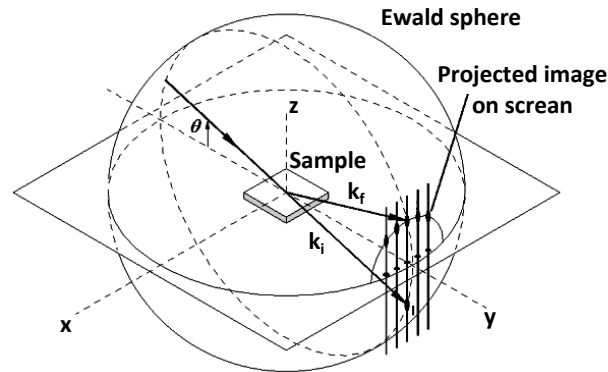


Figure 2.2: Ewald construction for electron scattering from a real surface. Difference between incoming and outgoing wavevectors \mathbf{k}_i and \mathbf{k}_f is a reciprocal vector only if the Laue condition is fulfilled. Semicircle is the zero order Laue zone.

A sphere of radius k is centered at the start of the incident wavevector \mathbf{k}_i . The diffraction conditions are fulfilled when the lines of the reciprocal space intersect with the Ewald sphere and produce diffraction spots arranged in concentric semicircles, called Laue zones. In reality, thermal vibrations, lattices imperfections and electron beam divergence determine a finite thickness of the ideal reciprocal rods and Ewald sphere, turning the spots into streaks with modulated intensity even for 2D surfaces. See fig. 2.3 b). If 3D structures are present on the surface, the RHEED pattern consists of a series of bright spots regularly arranged^[71], as illustrated in fig. 2.3 c).

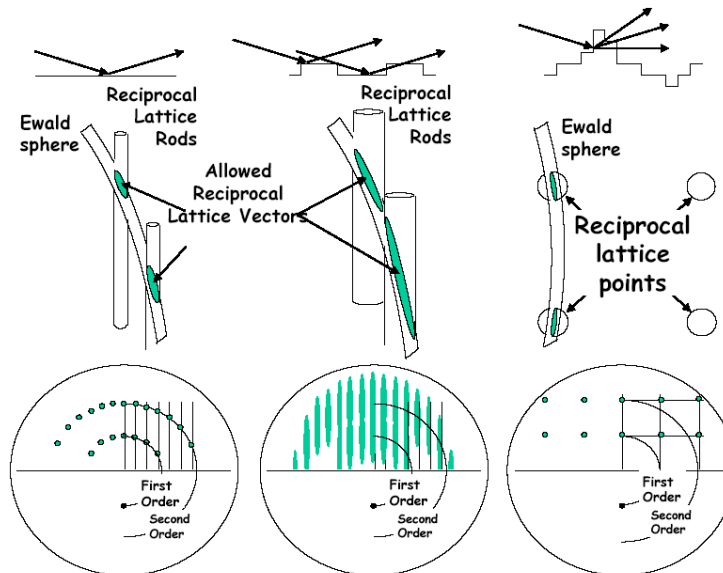


Figure 2.3: Illustrated diffraction pattern for: a) Perfectly flat surface with consequent ideal pattern; b) a real surface with reciprocal rods; c) real surface with 3D features and consequent regularly arranged spots.

Flux Calibration

Accurate calibration of source fluxes is a necessary operation before planning any growth experiment. For material systems which exhibit layer-by-layer growth such as GaAs, the flux calibration might be done by measuring the intensity oscillations of the specular beam as observed by RHEED^[72]. Nevertheless, other possibilities can be adopted, such as the use of a beam flux monitor. For our material system, we optimized a method based on performing amorphous growth of the different elements namely Ge, Sb and Te at very low substrate temperatures (<10 °C). For such temperatures it is reasonable to assume that all the impinging fluxes have sticking coefficient equal to one and no desorption occurs. The deposited layers are amorphous. Growths of samples are performed by varying the source fluxes and the thicknesses are measured by X-ray reflectivity XRR. It is worthwhile to clarify that what is actually measured is a growth rate (GR) for amorphous samples, obtained dividing the thickness of each sample by the growth time. Therefore in this thesis, fluxes will be expressed in nm/min, instead of conventional atom/cm²/s units. It is necessary to check the GR periodically to prevent depletion of the sources and appropriately increase the temperature of the effusion cells to compensate for the decrease in flux.

2.1.1 Thin-Film Crystallization/Amorphization Methods

Thermal Annealing

Samples of x-GST were also produced performing rapid thermal annealing (RTA) on a-GST previously grown by MBE.

RTA is a process used in semiconductor device fabrication which consists of heating a single wafer at a time in order to obtain different effects. For example wafers can be heated to activate dopants, effect film-to-film or film-to-wafer substrate interfaces, change the density of deposited films and for many other purposes. Those processes are performed in RTA furnaces. The one used in this thesis work is a JetFirst100. The wafer in the chamber is heated up by halogen bulbs fixed on the top of the chamber. Desired gases are inlet at specific locations through valves. A cooling water system allows the effective rapid cooling of the sample after the treatment. Temperature control is achieved by a thermocouple directly in contact with the wafer.

The annealing process is operated as follows: The GST sample is loaded into the furnace chamber on a Si wafer, then the chamber door is closed and locked. The annealing treatment recipe is implemented via computer introducing the set point temperature of annealing, the ramp rate and the gas flux. Considering that the GST sample is loaded on the Si wafer and that the thermocouple is directly in contact with the latter, the real temperature of the GST sample is actually lower than the measured one, which corresponds to that of the Si wafer. Details on the crystallization experiments are presented in section 3.3.

Application of Femtosecond Laser Pulses

Crystallization of a-GST layers and amorphization of x-GST previously grown by MBE has been performed by application of a *pulsed laser*.

Pulsed laser refers to any laser not characterized by continuous wave emission, so that the optical power appears in pulses of some duration at some repetition rate, defined as number of emitted pulses per second. An extensive review of pulsed lasers can be found in dedicated literature^[73].

Laser system used in the laboratory at PDI is the same as the one employed at the synchrotron for the optical-pump/X-ray probe and optical-pump/THz probe experiments described in chapter 5 and section 2.3.

To achieve the goals of this thesis, the employed laser should fulfill the following requirements:

Pulse duration: fs-laser pulses are desirable to investigate effects in the non-thermal time domain.

High pulse power: In pump-probe experiments, to enable the detection of the laser switched regions of the sample, it has to be ensured that only laser altered material contributes to the detected signal. Therefore, the spot size of the pump laser must exceed the one of the probe. In this thesis work pump-probe experiments have been performed employing X-ray and THz probes, with spots diameters of $30\ \mu\text{m} \times 150\ \mu\text{m}$ and $300\ \mu\text{m}$, for X-ray and THz spot, respectively. Furthermore, since the fluence of a laser, defined as the optical energy delivered per unit area (mJ/cm^2), is inverse proportional to spot size and repetition rate, high energy pulses lasers in the range of mJ/pulse are desirable. This allows to cover a wide range of fluences during the switching experiments.

Repetition rate: The high power laser must have a high repetition rate. In time-resolved laser-pump/X-ray-probe experiments, the number of available X-ray photons is very limited (see chapter 2.3.3), thus, a high repetition rate must compensate the low number of photons per single shot, to obtain a significant signal to noise ratio. This repetition rate is used later in the time-resolved X-ray study.

In this thesis work, the pulsed laser is a COHERENT Micra-Legend Elite tandem system. A Micra Ti:Sa oscillator is used as seed laser to supply the pulses for the regenerative amplifier. The Micra emits pulses at 800 nm wavelength at a pulse duration of less than 100 fs. The pulse power amounts to several nJ. The natural free running repetition rate is 80 MHz. The pulses are selectively coupled into the regenerative Legend Elite amplifier. The amplifier emits 800 nm and 3 mJ pulses at a repetition rate of 1 kHz. The pulse duration amounts to 150 fs FWHM with temporal Gaussian pulse shape. These laser pulses are used in the laboratory for crystallization and amorphization of GST samples, which represents preliminary fluence calibration for synchrotron based experiments (see chapter 5).

The laser pump pulse induced change of the reflectivity of the GST film is monitored continuously by the reflection of the light of a continuous wave He-Ne laser that emits at 632 nm wavelength. That signal is recorded by a fast photodiode connected to a GHz oscilloscope. Details about the conducted experiments and their specific set-up scheme are given in chapters 3.4 and 5.

2.2 Thin-Film Characterization Methods

2.2.1 X-Ray Diffraction

XRD is a non destructive consolidate technique for the study of the atomic scale structure of materials. In particular, it allows to gather information on the average spacings between layers or row of atoms, to determine orientation of a single crystal or grain, to find the crystal structure of an unknown material and to measure the size, shape and internal stress of small crystalline regions. Due to the relatively high transmittance through matter of X-rays, their penetration depth of 10-100 μm into the sample and the lateral size of the spot of 100 μm range, XRD is considered as an averaging bulk technique. The diffractometer used for XRD characterization in this thesis was the triple-axis Panalytical X'Pert PRO MRD system with Ge(220) hybrid monochromator, employing a monochromated Cu-K α 1 radiation ($\lambda = 1.54 \text{ \AA}$).

When the X-ray hits an atom, the electrons around the atom start to oscillate at the same frequency of the beam. In almost all directions destructive interference appears, meaning that waves are out of phase. Due to atoms periodicity, only in few directions constructive interference occurs. The wave then will be in phase and diffracted X-ray beams. The problem can be described considering X-ray reflection from the aforementioned series of parallel planes inside the crystal. The orientation and interplanar spacings d are defined by the Miller indices h, k, l . If we consider an X-ray beam incident on a pair of parallel planes P1 and P2, separated by interplanar spacing d , as shown in fig. 2.4, condition of maximum intensity beam or constructive interference will occur when the difference in path length between the waves 1 and 1' as well as 2 and 2' is an integral number of the radiation wavelengths λ . This means that 1 and 2 are two in phase waves. This can be analytically expressed by the so called Bragg law:

$$2d \sin \theta = n \lambda. \quad (1)$$

where θ is the incident angle of λ and n is an integer which gives the order of diffraction. This means that experimentally by using X-ray of known wavelength λ , and measuring θ , it is possible using eq. (1) to determine the spacing d .

For diffraction studies, it is important to consider the reciprocal lattice. Given three primitive vectors a, b, c in the direct space, we can define three primitive vectors $\vec{a}^*, \vec{b}^*, \vec{c}^*$ in the reciprocal space as follows:

$$\vec{a}^* = 2\pi \frac{\vec{b} \times \vec{c}}{\vec{a}(\vec{b} \times \vec{c})}, \vec{b}^* = 2\pi \frac{\vec{c} \times \vec{a}}{\vec{b}(\vec{c} \times \vec{a})}, \vec{c}^* = 2\pi \frac{\vec{a} \times \vec{b}}{\vec{c}(\vec{a} \times \vec{b})}. \quad (2)$$

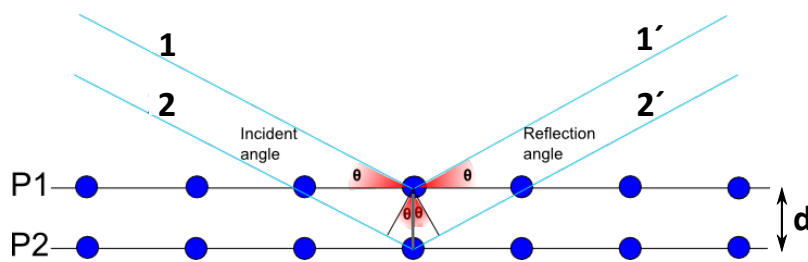


Figure 2.4: Bragg law.

The reciprocal space lattice is build up considering all the vector points \vec{G} of the form $\vec{G} = \vec{a}^*h + \vec{b}^*k + \vec{c}^*l$. The concept of reciprocal lattice was introduced by Ewald and his geometrical construction is reported in (fig. 2.5). If the difference between the incoming \vec{K} and outgoing \vec{K}_o vectors is equal to a reciprocal lattice vector \vec{G} (connecting the two lattice points A and P in reciprocal space), then constructive interference occurs and Bragg peak appears at the corresponding θ position. Each reciprocal space vector correspond to an infinite number of parallel, equally spaced lattice planes in real space. The normal vector of these planes has the same direction as the corresponding reciprocal space vector \vec{G} and the spacing of the lattice planes is given by $d_{hkl} = 2\pi/G$. As already mentioned, in XRD experiments direct information on reciprocal lattice space is obtained, thus keeping in mind the properties and the relations between the two geometrical spaces, it is possible to translate in the direct lattice space the information obtained into the reciprocal space.

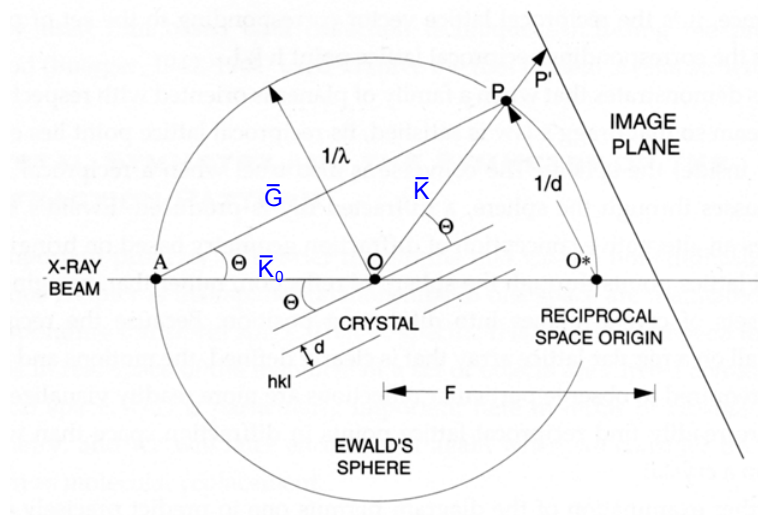


Figure 2.5: Ewald construction of Bragg condition. \vec{K}_0 and \vec{K} represents the wave vectors of the incoming and outgoing X-ray beam respectively. "A" and "P" are two points of the reciprocal lattice.

X-Ray Diffraction Measurements of Thin Epitaxial Films

In XRD measurements first the illumination of the sample by an incoming X-ray beam takes place, the beam is then diffracted by the sample mounted on a holder and further on the detection of the diffracted beam by a detector in a known orientation with respect to the incident beam is accomplished. Using a triple axis XRD spectrometer, the orientation of the sample can be changed with respect to the incident X-ray beam, and the orientation of the detector can be changed with respect to the sample.

Before measurement the sample has to be aligned to optimize the signal to noise ratio. Different mechanical assembly of the X-ray tube, sample holder and detector can be used, but the most common is the θ - 2θ Bragg Brentano configuration^[74].

The source does not move, whereas the sample rotates around its axis at a speed θ , the detector meanwhile is moving at a speed 2θ along the circle centered in the sample and referred as the goniometric circle. In this configuration different types of experiments can be performed. In the present work, specular θ - 2θ scans, ω scans, ϕ scans and X-ray reflectivity (XRR) measurements were performed.

ω - 2θ scan

The so called ω - 2θ scan is one of the most common measurement in XRD. The sample is positioned in the center of the instrument and both the X-ray source and the detector can rotate around the sample so that the probing X-ray beam and the out-coming beam form an angle ω and θ with the sample surface respectively^[74].

A particular case of ω - 2θ scan is the specular θ - 2θ scan in which case the analyzer rotates at a velocity that is the double of that of the detector. Thus ω is always equal to θ . Contribution to the diffraction is only due to regions of the sample having planes which are parallel to the surface and separated by a constant lattice spacing $d(\theta)$. Therefore this measurement provides information about the sample only in the *out of plane direction*.

In fig. 2.6 is presented a scheme of specular θ - 2θ scan in the sample reference view indicated by the unity vectors \vec{s}_1 and \vec{s}_3 . \vec{Q} represents the scattering vector and has the dimensionality of an inverse length, while its direction points along the bisection of \vec{K}_0 and \vec{K} which are respectively the wave vectors of the incoming and scattered beam. The relation $|\vec{Q}| = \frac{4\pi \sin(\theta)}{\lambda}$ holds for the scattering vector magnitude. In specular θ - 2θ scans $\vec{K}_0 = \vec{K}$ holds.

Diffraction occurs when $\vec{Q} = \vec{K}_0 - \vec{K}$ is a vector of reciprocal space \vec{G} and it is always normal to the sample surface.

In our study, lattice parameters c in the *out of plane direction* have been determined by using the following formula which relates peak positions and distances in the XRD profiles (in $|\vec{Q}_z|$) with periodicities in the crystalline structures:

$$c = \frac{2\pi}{\Delta|\vec{Q}_z|}. \quad (3)$$

where $\Delta|\vec{Q}_z|$ is the distance between two peaks in the XRD profile (see chapter 3.1.1).

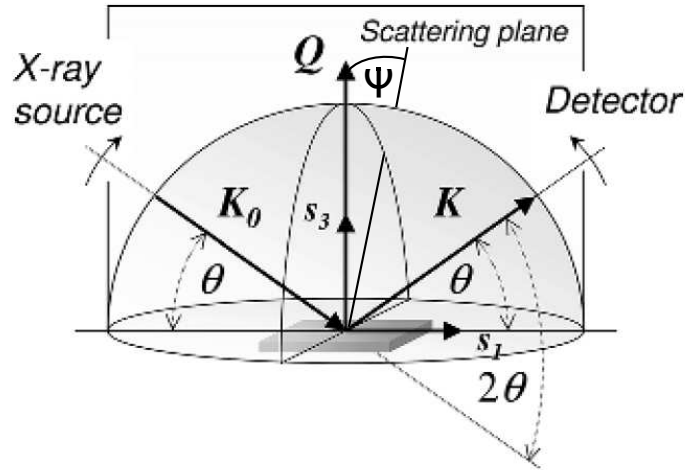


Figure 2.6: θ - 2θ scan configuration from the point of view of the sample reference frame $[\vec{s}_i]$ ^[74].

ω scan

The detector is fixed at an angle $2\theta_0$ which corresponds to the center of the Bragg peak under investigation, whereas the sample is rocked on the θ circle in the vicinity of θ_0 . The full width at half maximum (FWHM) of the peak obtained in the ω scans provide information about the quality of the crystalline structure. The rocking curve measurement can also be performed for any ω - 2θ pair of angles within a certain range, yielding a reciprocal space map (RSM), to get a more complete picture of the crystalline state in the sample. By imaging a wider section of the reciprocal space, including multiple reflections, their relative position can be used to determine the state of strain in the film in respect to the substrate or to other layers^[75].

ϕ scan

This kind of measurement is complementary to the θ - 2θ as it allows to obtain information on the crystallographic orientation in-plane or in any direction other than the out-of-plane. It is necessary to investigate the in-plane orientation to determine the degree of twist or the possible presence of rotational domains. In this case, another family of planes $\{h' k' l'\}$ is put in diffraction conditions such that its intersection with the $\{h k l\}$ planes is a characteristic crystallographic direction. This is performed by setting the tilt angle ψ of the diffractometer to a constant value in respect to the sample normal \vec{s}_3 . Choosing as a reference the angular position of the $\{h k l\}$ plane and known the angle between the two directions, it is possible to determine the incidence angle in order to be in the Bragg diffraction for the $\{h' k' l'\}$. The scan consists then in a measurement of the intensity as a function of ϕ for constant ω , 2θ and ψ , where the latter accounts for the rotation of the sample around the substrate normal. If the corresponding measurement shows peaks it means that also in the $[h' k' l']$ direction the film is oriented. If no preferential directions are

present in the azimuthal direction, then the graph shows an uniform distribution of intensity and this is the case of the patterns from a fiber.

2.2.2 X-Ray Reflectivity

XRR is a method which allows the investigation and characterization of surface layers and thin films. In this method the diffractometer is operating in the symmetric θ - 2θ configuration as shown in fig. 2.6, but with much smaller θ angles than in the θ - 2θ diffraction case^[74].

For incident X-rays, the refractive index of a material is slightly less than 1 and can be expressed as:

$$n = 1 - \delta - i\beta$$

where δ is the dispersion and β the absorption and are defined by

$$\delta(\lambda) = \frac{\rho_e \cdot r_e \cdot \lambda^2}{2\pi}, \quad \beta(\lambda) = \frac{\mu \cdot \lambda}{4\pi}$$

and

ρ_e : electron density (Z electrons/atoms)

r_e : classical electron radius = e^2 / mc^2

μ : linear absorption coefficient for energies far from X-ray threshold

The quantities $\delta(\lambda)$ and $\beta(\lambda) \sim 10^{-6}$ describe the dispersion and absorption terms respectively^[74].

When an X-ray beam impinges at a grazing angle on to an ideal flat surface of a material, total reflection occurs below α_c , and the incident X-rays do not penetrate into the material. X-ray reflectivity signal decrease rapidly with increasing incident angle θ above α_c .

But at low angle, reflection and refraction events can thus occur multiple times at each interface in the sample. If a refracted beam is able to escape the thin-film, it will recover the same direction and velocity as the directly reflected beam, owing to the conservation of momentum. However, because of the beam travels a longer path at slower speeds in the material, it could be out of phase from the main specular reflection, and therefore it interferes with it. By increasing the incident angle, the path-length is gradually reduced, making the phase-shift alternate between a constructive and a destructive interference. Plotted with respect to the incident angle, the total reflected intensity will therefore show periodic oscillations, which were first observed in 1931 by Kiessing and therefore called Kiessing fringes. They depend on the film thickness, and the thicker the film the shorter the period of the oscillations. The amplitude of the oscillation and the critical angle α_c for total reflection provide information on the density of films. The amplitude of the oscillation depends on the difference between the densities of the film and its substrate, the larger the difference, the higher the amplitude of the oscillation.

2 Experimental Methods and Theory

Furthermore, for increasing densities of the film there is a shift in the total reflection edge towards higher angles since the density ρ is directly proportional to the square of the critical angle α_c . Another important structural parameter that affect the measurement is the roughness (superficial and interfacial), which causes a decrease of the reflected X-rays.

Therefore, from a X-ray reflectivity curve, structural parameters like thickness, density and roughness can be obtained combined to fit of the curves. This method is of course an averaging technique, the rather large collimated X-ray spot being additionally spread out in the incident direction because of the small incidence angle. XRR can be performed indiscriminately on amorphous and crystalline material, since it does not rely on diffraction, but only on the contrast in electron density. The theory behind this phenomena is well known, but the addition of many free variables in a complex case should however be considered carefully since different sets of parameter could yield similar fits.

XRR has been routinely employed to characterize all the grown samples.

2.2.3 Electrical Characterization

Temperature dependent electrical transport properties of the GST samples have been measured by employing van der Pauw method. Such method has been introduced in 1948^[76] and is based on a theorem which holds for a flat sample of arbitrary shape, if the contacts are sufficiently small compared to the sample size and they are located at its edges. Furthermore, the sample should have an uninterrupted coherent area, i.e. no holes should be present.

Fig. 2.7 shows how to measure the sheet resistance (R_s) of a sample. Meanwhile current I_{12} flows through the adjacent contacts named 1 and 2, the voltage V_{34} is measured between the opposite contacts named 3 and 4; the Van der Pauw resistance is then calculated according to the Ohm law:

$$R_{3421} = \frac{V_{34}}{I_{21}}$$

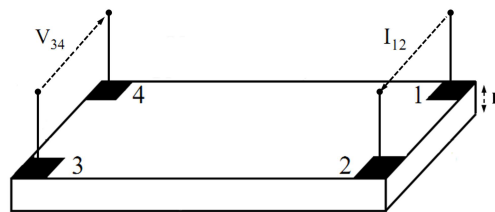


Figure 2.7: Van der Pauw arrangement to measure the sheet resistance R_s .

In order to eliminate possible voltage offsets due to temperature gradients or sample asymmetries (such as non-symmetric contacts, irregular shape etc.), "reciprocity theorem" is applied^[76]: The measurement is repeated by reversing the direction of the current and by applying it to the

contacts previously used to measure the voltage; the Van der Pauw resistance is then calculated as an average of the two values obtained. These steps are repeated again including the remaining two contacts permutations, giving the following result:

$$R_{\text{vertical}} = \frac{R_{3421} + R_{1243}}{2}$$

$$R_{\text{horizontal}} = \frac{R_{4132} + R_{2314}}{2}$$

Van der Pauw found that R_{vertical} and $R_{\text{horizontal}}$ are connected to the sheet resistance R_s by the equation:

$$\exp\left(\frac{-\pi R_{\text{horizontal}}}{R_s}\right) + \exp\left(\frac{-\pi R_{\text{vertical}}}{R_s}\right) = 1$$

This equation can be solved numerically obtaining R_s , otherwise, assuming $R_{\text{vertical}} = R_{\text{horizontal}} = \tilde{R}$, it is possible to write:

$$R_s = \frac{\pi \tilde{R}}{\ln 2} = \frac{\pi (R_{3421} + R_{1243})}{2 \ln 2}$$

Conventional laboratory low temperature Hall measurement set-up has been employed. GST samples with thicknesses of ~ 30 nm were cut in square shapes of 5×5 mm². Indium balls and Au bonds were used for the contacts and the above mentioned van der Pauw measurement has been performed in a range of temperature between 4-300 K. From the measurement, estimation of carrier concentration and Hall mobility at room temperature (RT) were also obtained, by applying a magnetic field (B) perpendicular to the sample^[76]. Electrical and magnetic field of 10 mA and 0.25 T were used, respectively.

2.2.4 Molecular Bonding Investigation by Raman Spectroscopy

Changes in bonding as well as in symmetry for GST are perfectly suited to be investigated by Raman scattering. While XRD is based on diffraction phenomena, related to periodicity and long range order in a crystal, Raman spectroscopy uses the inelastic interaction between optical laser radiation and electron orbitals to probe the bonding and conformation of atoms in the short range. If ν_0 is the wavenumber associated with the incident radiation, the system after the interaction will be characterized by $\nu = \nu_0 \pm \nu_M$ where ν_M is called Raman shift and lie principally in the ranges of energy associated with transitions between rotational, vibrational and electronic levels^[77]. Depending on the wavelength of the chosen laser power, and samples materials, the penetration depth can vary in a range from few nanometers to few micrometers. Using a focusing objective

2 Experimental Methods and Theory

lens, a laser spot as small as 1 μm can be obtained. To a certain extent, Raman spectroscopy, even if very sensitive to short range, can be considered as an averaging bulk characterization method. This method can be applied indiscriminately to amorphous and crystalline materials.

Generally speaking^[77], the electromagnetic field of the incident photons excites the electron densities present around the molecules. Depending on how susceptible these orbitals are to polarization, they are prompted to oscillate in unison with the monochromatic light, turning the molecule into an oscillating dipole. In most cases, the emitted and impinging light have the same wavelength, no energy is exchanged (Rayleigh scattering).

In Raman scattering cases, the coupling of the oscillating dipole with vibrational modes in the molecule, is such that the wavelength of the emitted light differs from the impinging one. If energy is taken away from the oscillating dipole, to send the molecule into a higher excited vibrational state, the emitted radiation will have less energy (Stokes Raman scattering). The other possibility is that the energy of the excited state is added to the emitted radiation, and a shorter wavelength is observed (anti-Stokes Raman scattering). At room temperature, the vibrational ground states are more dominantly populated, making the Stokes scattering more likely^[77]. For general purposes, and in the scope of this thesis, only the Stokes scattered Raman is measured.

The setup used for the Raman measurements in the framework of this thesis was the HORIBA LabRAM HR Evolution. Measurements were taken in backscattering $z(x, xy)\bar{z}$ geometry, meaning that incident light is polarized in the x direction, while the polarization of the backscattered light is not selected. The 632.8 nm line of a He-Ne laser was used to excite the material, and the scattered light was analyzed using a spectrometer equipped with an LN_2 -cooled charge-coupled device detector. For the temperature dependent measurements a heating stage (THMS600 by Linkam) was employed during Raman spectra acquisition.

2.3 Synchrotron Characterization

A consistent part of this work has been performed in a collaboration with Helmholtz-Zentrum Berlin (BESSY II) at the Femtoslicing beamline (UE56-1-ZPM)^[78] and THz beamline^[79]. The main objective of the collaboration was the realization of the first ultrafast dynamic investigation of PCM in an optical-pump/THz-probe scheme. In order to achieve this goal, static far-infrared (FIR) spectroscopy has first been performed on GST and CSL samples in order to test the suitability of the measurement for our material system. This led to a series of optimization of both sample preparation and beamline set up in order to maximize the signal-to-noise ratio of the outputs. Furthermore, the static measurements resulted to be very well suited to investigate fundamental open questions regarding the GST material system (see chapter 4).

Prior to the THz study, two beam times dedicated to the XAS investigation applied to PCM have been also performed.

2.3.1 Investigation by Far-Infrared Spectroscopy

Infrared absorption spectroscopy, such as Raman, belongs to the category of vibrational spectroscopies. When IR light (10000 to 10 cm^{-1} in the electromagnetic spectrum) interacts with a sample, absorption occurs at resonant frequencies, which match the vibrational frequency of a bond or collection of bonds in the sample. What differentiate IR from Raman spectroscopy, are the selection rules. In the IR case, the selection rule is that the electric dipole of a molecule must change during vibration, in order to be IR active; this implies that symmetric vibrations modes are forbidden, while the asymmetric ones are IR active. The Raman spectroscopy, instead, dealing with the change of polarizability (see paragraph 2.2.4), can present Raman active modes also when a molecule is stretched symmetrically, if this implies a change of polarizability. Hence, IR and Raman spectroscopy are considered complementary^[80]. The application of IR spectroscopy to organic chemistry is well established, nevertheless, its use for investigation of thin films such as Si, GaAs and others used in microelectronics has become also very popular and can be found in dedicated books^[80].

The commonly used measurement technique that allows to record infrared spectra is Fourier transform infrared (FTIR) spectroscopy. Infrared light is guided through a spectrometer, essentially working as a Michelson interferometer^[80] and then on the sample. A moving mirror inside the apparatus alters the distribution of infrared light that passes through the interferometer. The signal directly recorded, called an "interferogram", represents light output as a function of mirror position. A Fourier transform data-processing technique turns this raw data into the sample absorption spectrum as a function of the IR wavenumber.

Static investigations for this thesis work were carried out under vacuum conditions using the high-resolution Fourier transform infrared spectrometer (BRUKER IFS 125HR) of the THz beamline at Helmholtz-Zentrum Berlin (BESSY II)^[79]. Measurements have been performed in both transmission and reflection geometries of the impinging IR beam in respect to the sample. The spectral range in the presented experiments covered wavenumbers between 30 and 650 cm^{-1} , therefore in the Far-Infrared region, and was limited by the selected source (internal Hg-lamp), the $6\text{ }\mu\text{m}$ multilayer-mylar beamsplitter and the detector, a 4.2 K Si-Bolometer. A copper block heating stage was employed during *in situ* temperature dependent FIR measurements.

In this frequency range of the spectrum, mainly optical phonons, impurities and free carriers contribute to the spectrum^[81]. In addition the included THz range (from 3 to 300 cm^{-1}), which is highly sensitive to the presence of free mobile carriers, makes the ultrafast THz probe an ideal tool to study ultrafast carrier dynamics in the systems, where the carrier transitions between the conducting (i.e. strongly THz absorbing) and localized (and thus not making significant contribution to the THz loss) states is of interest^[82].

2.3.2 Experimental set-up of the Optical-pump/Terahertz-probe Experiment at Bessy II

For the dynamic investigations, THz pulses obtained from coherent synchrotron radiation are employed as probe. Their frequency spectrum between 10 and 150 cm^{-1} is included in the aforementioned FIR range employed for static characterization. The generation method of such pulses is presented below.

Generation of Single Cycle THz Pulses of Coherent Synchrotron Radiation

For the generation of THz pulses in the storage ring and optical excitation of the samples, a 800 nm fs-laser (COHERENT Legend Elite PRO, 1.8 mJ pulse energy and 45 fs FWHM-pulse length) routinely operated at 6 kHz repetition rate, was employed^[83]. THz probe pulses are emitted as a result of the interaction between a laser and a relativistic electron bunch, according to fig. 2.8 a). THz generation is accomplished by a resonant energy modulation of a slice of the 1.72 GeV electron bunch along its propagation in a wiggler (see fig. 2.8). The first harmonic radiation of the latter is tuned to the laser wavelength of 800 nm^[84]. After passing dispersive elements along its track, the laser-excited electrons move longitudinally out of their initial excitation region (the slice) leaving a dip in charge density behind. This dip (with side lobes)^[85] gives rise to intense ultrashort single cycle THz pulses at subsequent bending magnet sources in our case at the THz-beamline. Using a crosscorrelation method depicted in fig. 2.8 b), a signal proportional to the field transient as well as its temporal arrival time jitter in the time domain [fig. 2.8 c)] was determined. The length of the dip in the electron bunch determines the frequency spectrum of the emitted THz pulse (see fig. 2.9) and via the Fourier limit also the minimum pulse length (inset in fig. 2.9). In addition, much weaker but broad band incoherent synchrotron radiation, approaching also the THz range, is emitted by the electron bunch.

For time-slicing with a laser pulse length of σ_L (here given in root mean square, *rms*) in a storage ring, the average power spectrum $P_{\text{coh}}(\omega)$ of a laser-induced THz pulse on a bunch of length σ_B as plotted normalized to the total incoherent emission $P_{\text{inc}}(\omega)$ from the storage ring in fig. 2.8 is given by:

$$P_{\text{coh}}(\omega) = \frac{f}{e} \left[\frac{\sigma_L I_{\text{SB}}}{\sigma_B \nu_R} \right]^2 \frac{\nu_L}{I_{\text{tot}}} P_{\text{inc}}(\omega), \quad (2.1)$$

where the form factor f is the normalized square of the Fourier transform of the longitudinal shape of the density modulation along the electron bunch, $\nu_L = 6$ kHz and $\nu_R = 1.25$ MHz are the repetition frequencies of laser and bunch, respectively. The bunch currents are $I_{\text{SB}} = 4$ mA for the sliced bunch and $I_{\text{tot}} = 300$ mA total current at BESSY II, e is the elementary charge. Inserting the relevant values one finds that $P_{\text{coh}}(\omega)$ from one single slice exceeds the average power from all other bunches.

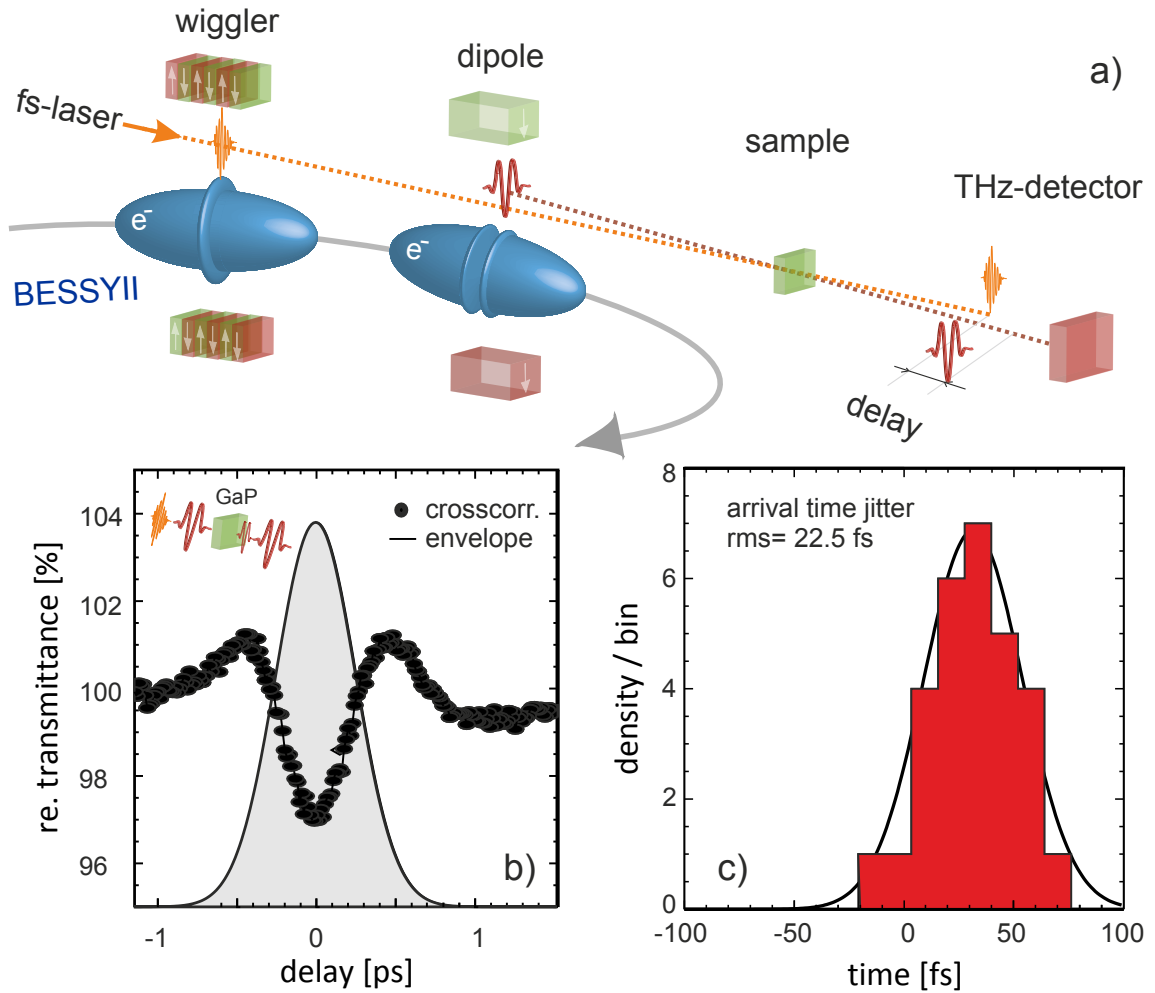


Figure 2.8: a) Experimental setup of the optical-pump/THz-probe experiment at BESSY II: THz-CSR is emitted by a slice in the electron bunch (blue ellipsoid) in the storage ring after 800 nm laser energy modulation in a wiggler. Optical and THz pulses are indicated by orange and wider red electric field traces, respectively. The resulting THz pulse is used to probe changes in a sample exposed to the same laser pulse. b) A sub-ps time resolution is derived from a THz-THz cross-correlation experiment in a 0.1 mm GaP(110) sample b) and the measured arrival time histogram of such pump-probe delay scans is depicted in c). Reprints from^[113]

2 Experimental Methods and Theory

This is confirmed by the measurement in fig. 2.9 where the laser induced P_{coh} and reference spectra P_{inc} taken at time-averaged detection are simply divided one by the other. The observed peak is at around 70 cm^{-1} (i.e. at about 2 THz), but it can be tuned by changing laser parameters (chirp) and by detuning the so called free electron laser (FEL) resonance condition^[84] given by the wiggler gap setting as shown in fig. 2.9. The advantage of this is that the probe shape can be tuned in order to be resonant with eventual probed samples broad minimum in the static frequency response. An application of that to the GST case will be treated in details in chapter 5.2

Concerning the pump/probe set up for our dynamic experiments, the sample is excited with the same 800 nm laser pulse that generated the THz pulse in the wiggler. To detect the fs-laser-induced dynamics changes, the probe pulse was sampled using digital boxcar averaging (UHFLI, Zürich Instruments) of the THz signal (with a 4.2 K bolometer) triggered to 3 kHz, a phase-locked sub-harmonic of the laser repetition frequency (6 kHz) [see fig. 2.8 a)]. Since the pump pulse of 100 fs pulse duration has to pass a chopper wheel that blocks it every second shot, the pumped and unpumped sample transmittance can be acquired in separate channels but simultaneously. The delay between laser and THz pulse is varied by an optical delay stage in the laser path. The time resolution of the experiment is given by the pulse length of the THz pulse rather than the laser. It is determined by the initial sub-ps density modulation (inset in fig. 2.9) on the electron bunch, but also by lengthening effects given by two z-cut quartz windows that separate the THz beamline from the storage ring vacuum system. An upper limit of 0.7 ps [FWHM] was obtained in fig. 2.8 b), using a GaP(110) single crystal in transmittance as cross-correlator to probe a signal proportional to the THz electric field transient \vec{E}_{THz} . The gray shaded area depicts the corresponding intensity envelope of $|\vec{E}_{\text{THz}}|^2$.

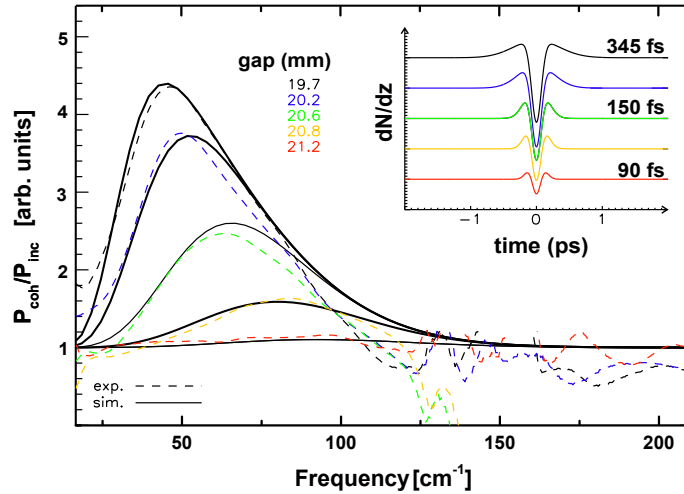


Figure 2.9: THz spectra of the probe pulse measured for different gap settings of the wiggler (modulator, U139) with corresponding sub-ps electron density modulations from simulations (inset). The probe pulse spectra are normalized to the incoherent background spectrum, as emitted from all the other bunches in the laser-OFF case. Reprints from^[113]

2.3.3 Investigation by X-Ray Absorption Spectroscopy

XAS is a widely used technique for determining the local geometric and/or electronic structure of matter. The experiment is usually performed at synchrotron radiation sources, which provide intense and tunable X-ray beams. A typical normalized X-ray absorption cross-section as a function of energy is given in fig. 2.10 for a compound with a perovskite structure, La_2CuO_4 , measured at the Cu K-edge^[86]. The X-ray near-edge absorption and X-ray extended absorption regions are pointed out and labeled XANES and EXAFS, respectively. The absorption cross-section, $\mu(E)x$ is measured by determining the attenuation of X-rays by a sample with thickness x :

$$\ln \frac{I_0}{I} = \mu(E) \cdot x$$

where I_0 and I represent the incident and transmitted beam intensity measured by using ionization chambers.

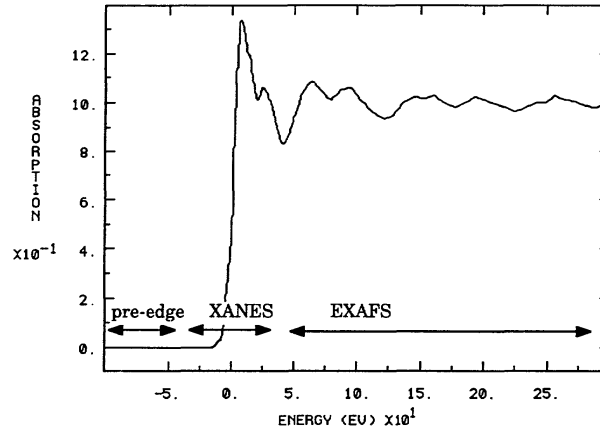


Figure 2.10: Normalized absorption cross section of La_2CuO_4 as a function of energy near the Cu K-edge ($E = 8979$ eV). XANES and EXAFS regions are pointed out. The zero of the energy is with respect to Cu K-edge position^[86].

In the XANES, X-ray absorption process is the result of an excitation of an inner level electron to a higher energy level by an incident photon. Since it involves an electronic transition it can be best represented by a transition matrix element coupling the initial state $|i\rangle$ to the final state $\langle f|$:

$$\mu(E) \approx | \langle f | \epsilon \cdot r | i \rangle |^2$$

where ϵ is the polarization vector of the electric field of the photon, and r is the position vector of the photoelectron. Since the operator coupling the two states is an electric dipole operator, the selection rules apply and determine the allowable final states for a given initial state. For example, when a $1s$ level electron is excited, the lowest-lying empty p -states will be occupied and

2 Experimental Methods and Theory

the process is called K-edge absorption. Each element has a characteristic energy level structure and therefore can be studied separately. The empty energy levels above the Fermi level in a compound are also sensitive to the nature of the chemical bond and valence.

EXAFS is an interference effect caused by the interaction of the outgoing photoelectrons ejected from inner core levels by the resonant radiation, and the backscattered electrons from the near neighbor atoms, modulating the final state wavefunction of the absorbing atom. It was correctly interpreted by Sayers *et al.*^[87] to be related to the radial distribution function around the central absorbing atom. EXAFS yields information about the interatomic distances, near neighbor coordination numbers, and lattice dynamics.

Within our study, optical-pump/XAS-probe has been realized in a transmittance configuration tuning the X-ray probe near the Ge L3 edge (1.216 eV), therefore in the XANES energy region. The optical pump is an 800 nm fs-laser with a pulse length of 50 fs and a repetition rate of 3 kHz. The transmitted X-rays were measured by an avalanche photo-diode detector. The X-ray spot size of 30 mm x 150 mm was smaller than the 300 mm x 300 mm laser spot size, ensuring a homogeneous excitation of the probed area. The X-ray pulse length for the experiment is ~ 50 ps full width half maximum (FWHM). The time-dependent change in X-ray absorption was measured by changing the delay time between the X-rays-probe and the optical-pump (see fig. 2.11). The X-ray repetition rate was 6 kHz, allowing for the measurement of the sample in a pumped and unpumped state, the latter used as a reference signal. When the beamline is operated in "slicing mode" like in our case, the number of photons per X-ray pulse is 10. Considering the repetition rate, and other parameters of the beamline such as spectral bandwidth (BW) and the electron current (4 mA), a the average number of detected photos is ca. $6 \cdot 10^5$ ph/sec/0.1%BW/4mA, which is the unit of the photon flux as described elsewhere^[78]. The sample inside the chamber was monitored using a charge-coupled device (CCD) camera for inspection by eye.

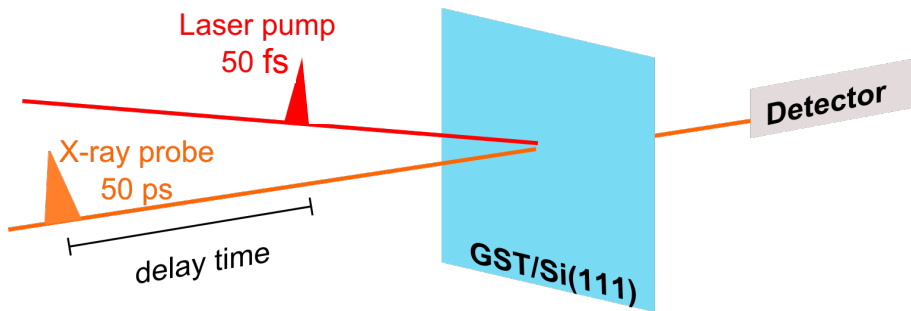


Figure 2.11: Schematic illustration of the pump-probe configuration. Experiment is performed in transmittance. X-ray probe with energy near the Ge L3 edge and 50 ps pulse duration is overlapped with the 800 nm fs-laser pump on a PCM sample. Change of the delay time between pump and probe pulses allows for time-resolved absorption measurements.

3 Fabrication Methods and Structural Properties of Quasi-Single-Crystalline Phase Change Materials

This chapter is dedicated to the fabrication of the epitaxial samples employed for the static and dynamic investigations performed in this thesis (see chapters 4 and 5). A fundamental advance in the fabrication of GST and GeTe/Sb₂Te₃ based superlattices through MBE resulting in as-deposited quasi-single-crystalline films is presented. Such high perfection material is expected to simplify the interpretation of the experiments, such as the direct observation of vacancy configurations, therefore opening the possibility to tune the degree of vacancy ordering in the material, which was so far only predicted (see chapter 1.2.1). Most interestingly, such tuning of vacancy ordering combined with low temperature transport measurements, allows to correlate the ordering degree in GST with the MIT, as will be discussed in chapter 4.

The first section 3.1 of the chapter is dedicated to the growth by MBE. It is shown how a structural characterization based on XRD simulations, DFT, and TEM microscopy, allowed to unequivocally assess the vacancy ordering in the GST samples. The understanding of the ordering process enabled the realization of a fine tuning of the ordering degree, which is also presented, together with the discussion on the interplay between composition, crystalline phase and vacancy ordering in GST alloys. A phase diagram with the different growth windows of GST follows.

Growth of CSLs is also briefly discussed in section 3.2.

In the third section 3.3, a more simple fabrication method based on annealing of a-GST is presented. Information gathered from annealing experiments, allowed to properly choose the samples for the most relevant experiments of this thesis work (see chapters 4 and 5).

In the fourth section 3.4, crystallization by application of fs-laser pulses is presented. Advantages and disadvantages of each technique are discussed in the following summary and conclusions.

3.1 Molecular Beam Epitaxy Growth of GeSbTe Alloys

Growth of GST on Si(111)-(7 × 7) surface was investigated by Karthick et al.^[88], nevertheless, many aspects concerning the growth and structural properties of the material were not yet explored or interpreted. Within the current work, an explanation is offered for uninterpreted

findings: The presence of additional peaks in the XRD profiles, their origin and their role in the electrical properties of the material. In addition, the ordering in the GST was tuned properly by changing the MBE growth parameters, which was never done before. Furthermore, improvements in the growth of GST are obtained in terms of suppression of rotational domains, texture and control of compositions and crystalline phases. A phase diagram of the growth conditions is finally proposed.

3.1.1 Structural Characterization

Regarding the out-of-plane and in-plane Epitaxial Relationship

Before going through the mentioned study, few clarifications have to be done concerning the choice of the Si(111) surface reconstruction, which resulted to strongly affect the in-plane quality of GST. In order to put the present work into its context, part of the old mentioned results are first reproduced here. Furthermore, an explanation is offered for some of their uninterpreted findings, in light of more recent data. Despite the large mismatch of $\sim 11\%$, a single c- and t-GST [00.1] \parallel Si [111] out-of-plane epitaxial relationship is achieved. However, in-plane twisted domains are observed at $\pm 6^\circ$, as illustrated by the ϕ -scan (see chapter 2.2.1) in fig. 3.1 (black curve), when growth is performed on the Si(111)-(7 \times 7) surface. If instead the GST film is grown on a different surface, i.e. Si(111)-($\sqrt{3} \times \sqrt{3}$)R30°-Sb, the twisted domains in GST results suppressed (blue curve). The latter surface is obtained by passivation of the Si(111)-(7 \times 7) surface which presents dangling bonds (see scheme in fig. 3.1), as reported in Boschker et al.^[89]. In this study we have shown that when a 2D material such as Sb₂Te₃, which is only weakly bound by vdW forces, is grown on a passivated surface like Si(111)-($\sqrt{3} \times \sqrt{3}$), the epitaxial registry is dictated by vdW epitaxy (2D/2D epitaxy, see scheme in fig. 3.1)^[89,90]. Because the formation of twisted domains is a strain relaxation process, it is no longer needed when the influence of the substrate lattice is drastically weakened. The epitaxial relationship is then mainly guided by the symmetry of the substrate. Note that the material grows fully relaxed as will be clearly shown in the dedicated study on strain effects in following section. In addition to the twisted in-plane domains, GST films grown on both Si reconstructions present in-plane twinned domains that can be recognized by the presence of peaks each 60° (i.e. repetition of the same peaks in fig. 3.1 every 60°, not shown), while they should be spaced by 120° as in the silicon substrate. In fact, both GST and silicon are characterized by a 3-fold symmetry around the out-of-plane direction, and no twinned domain should in principle be expected. However, if the interaction between the material and the substrate at the interface is relatively weak, only the topmost atomic layer of the substrate, characterized by its $6mm$ point symmetry, dictates the epitaxial relationship and allows the formation of twins. Details can be found elsewhere^[89,91]. All the studies described in this thesis work deals with GST grown on Si(111)-($\sqrt{3} \times \sqrt{3}$)R30°-Sb if not mentioned otherwise.

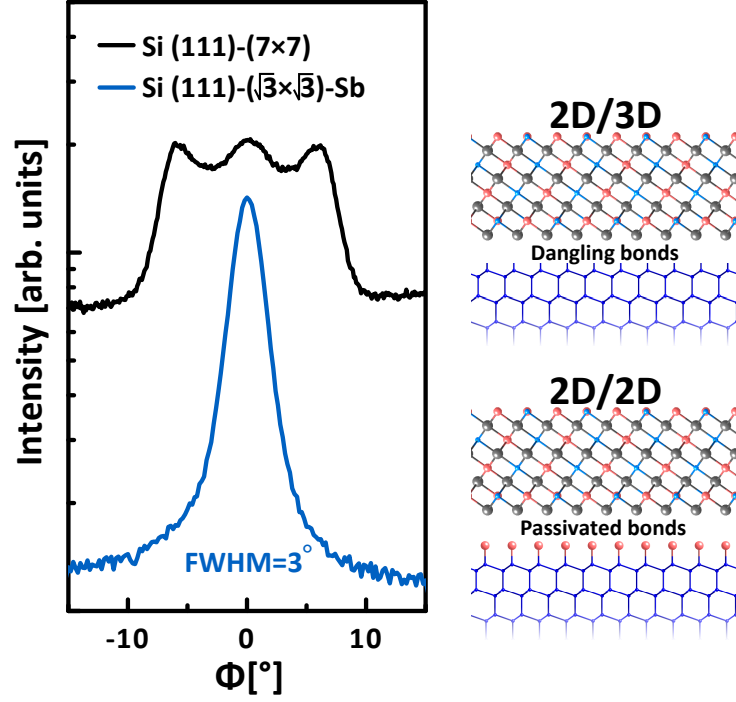


Figure 3.1: ϕ -scan around the GST (01.13) diffraction peak for a film grown on Si(111)-(7 × 7) (black curve) and on the Si(111)-($\sqrt{3} \times \sqrt{3}$)R30°-Sb (blue curve).

We now focus on the structural characteristics of highly textured GST (details about growth conditions will be discussed in section 3.1.2). In fig. 3.2 a) the XRD profile (symmetric ω -2 θ scan along the [00.1] direction, as introduced in chapter 2.2.1) of a GST sample is presented. Peaks at $Q_z = 2.00, 4.01 \text{ \AA}^{-1}$ are attributed to the Si substrate while two narrow peaks ($Q_z = 1.81, 3.61 \text{ \AA}^{-1}$) are ascribed to the GST epilayer. The latter are multiple order Bragg reflections of the GST epilayer corresponding to the (00.15) and (00.30) planes, respectively and therefore give rise to the periodicity of the Te-Te sublattice in fig. 3.6 (see methods 2.2.1). Note that for convenience the GST unit cell is described with hexagonal axes (details follow in "XRD simulation" paragraph). In cubic indexing, they would correspond to first (111) and second order (222) peak, respectively. Interestingly, three additional broader peaks ($Q_z = 1.44, 3.27, 4.00 \text{ \AA}^{-1}$) appear, which are not Bragg reflections of the GST unit cell (not integer order reflections of the first peak). Analysis of peak position and intensities excludes phase separation, atomic segregation or other crystallographic orientations.

Investigation of Strain Effects

In order to take into account a possible effect of strain as cause of such peaks, a dedicated XRD study was performed and discussed in the following. In fig. 3.3 a reciprocal space map (RSM) around the asymmetric Si(224) Bragg peak in coplanar configuration is shown. The axes are reported in reciprocal space units with $Q_z \parallel \text{Si [111]}$ and $Q_x \parallel \text{Si [-1-12]}$. From the coordinates of the GST(01.13) peaks it is possible to extract both the in-plane (a_{\parallel}) and out-of-plane (d_{GST}) periodicity-

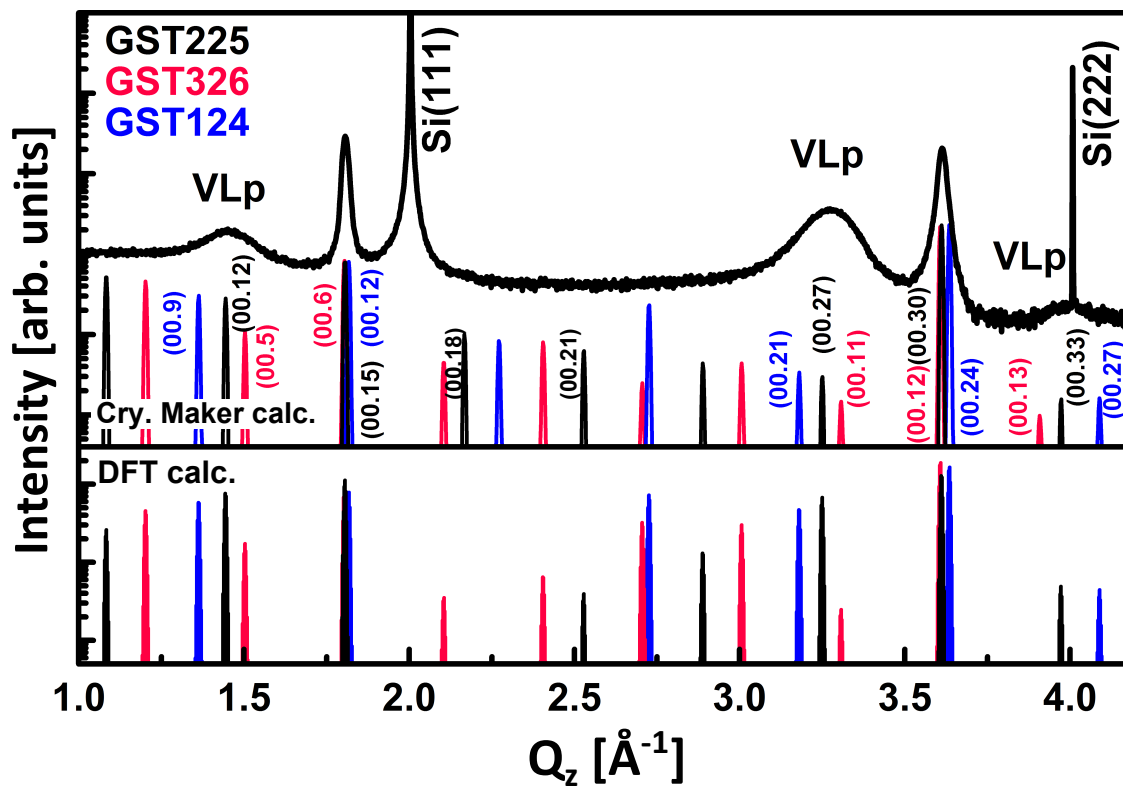


Figure 3.2: Superimposed ω - 2θ scan for crystalline GST grown by MBE (black curve) and simulations of the GST225 (326) [124] in black (red) [blue] performed by using Crystal Maker^[92] and DFT calculations. DFT calculations by courtesy of Dr. W. Zhang.

ties of the GST epylayer. In particular a_{\parallel} is 4.24 Å while d_{GST} is 3.53 Å, which corresponds to the distance of two Te-Te layers in the Te sublattice in the [00.1] direction. The values compare fairly good with the theoretical data reported by Da Silva *et al.*^[93]. From the relative distance between the Si(224) and the GST peak it is possible to estimate the degree of relaxation of the film. In fact the black line in fig. 3.3 represents the pseudomorphic case, while the magenta line was drawn using a literature reference for totally relaxed GST film (lattice constant $a_{\parallel} = 4.26$ Å)^[14]. The grown GST film clearly matches the magenta line and this indicates that it grows relaxed. The effect of strain is therefore not the cause of such additional broader peaks in the XRD profile of fig. 3.2.

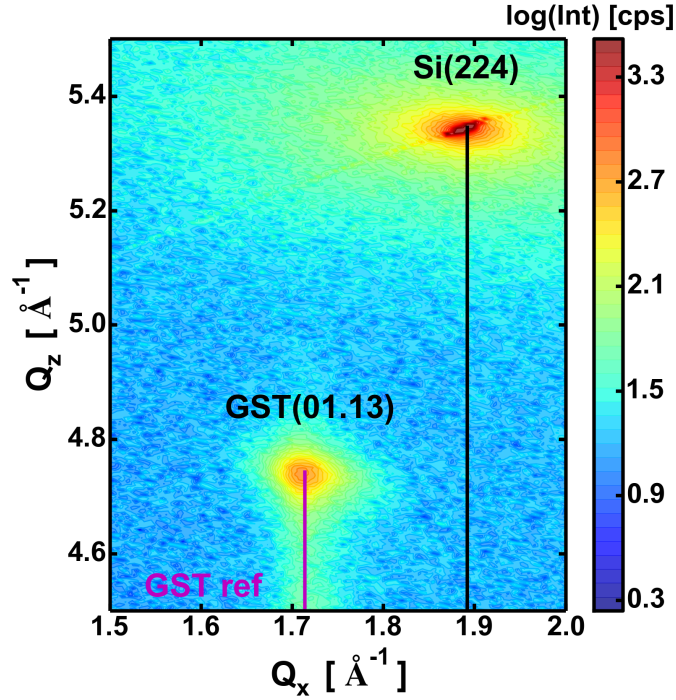


Figure 3.3: RSM around the asymmetric Si(224) Bragg peak with $Q_z \parallel$ Si [111] and $Q_x \parallel$ Si [-1-12]. The intensity is given in arbitrary units according to the logarithmic scale on the side. Reprints from^[94].

Growth on Substrates with Different Crystallographic Orientations

To further investigate the nature of the additional peaks, GST was also grown on almost lattice matched InAs with (001) and (111) orientations to discard effects related to mismatch and crystal orientation (see fig. 3.4).

Out-of-plane XRD of GST grown on substrates with crystallographic orientations different than the [111] does not show any additional peaks. In particular in fig. 3.4 a comparison of symmetric XRD scans for GST grown on InAs(001) and (111) substrates is shown. GST and InAs present a very low lattice mismatch $\sim 0.77\%$ if compared with the Si substrate ($\sim 11\%$), for this reason in the XRD profiles the peaks corresponding to the substrate and to the GST almost superimpose. For the GST grown on the InAs(001) (black curve) two sharp peaks at $Q_z = 2.04$ and 4.13 Å⁻¹

can be identified, which are attributed to the substrate first and second order of the [001] orientation, and two resolved peaks with slightly higher scattering angles at $Q_z = 2.08$ and 4.17 \AA^{-1} . They are attributed to the GST(20.5) and (40.10) Bragg reflections respectively. The small bump at $Q_z = 3.58 \text{ \AA}^{-1}$ which is ~ 3 order of magnitude smaller than the main reflection is attributed to GST(00.30) as already reported^[95,96]. In the blue curve corresponding to the GST grown on the InAs(111), the GST and substrate peaks are less resolved. However, similarly to the case of GST grown on Si(111), two additional features are visible at $Q_z = 1.61$ and 3.41 \AA^{-1} . No correspondence with any crystallographic orientation other than the [00.1] was found.

Therefore, we assume that the appearance of such peaks indicates the presence of occupational modulation of the individual Ge, Sb atoms or vacancies in the Ge/Sb sublattice, for instance, along the [00.1] direction.

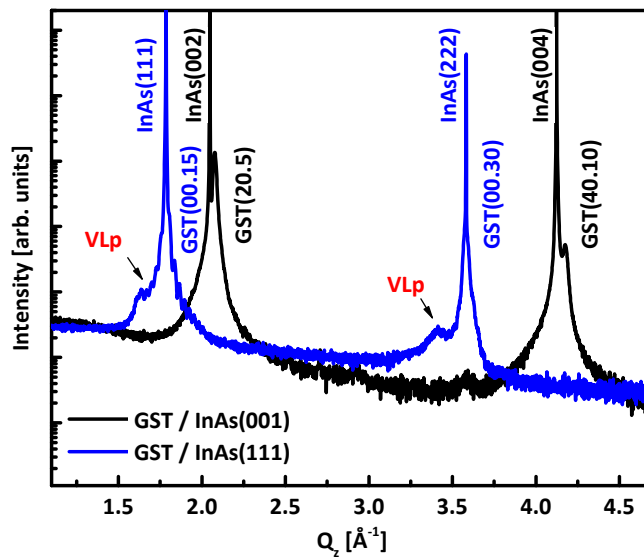


Figure 3.4: Symmetric ω - 2θ XRD scans for GST grown on InAs(001) (black curve) and InAs(111) (blue curve). Reprints from^[94].

To clarify this last assumption, within a collaboration with Prof. F. Arciprete, a series of simulations of the XRD data by using the Crystal Maker and Crystal Diffract software packages^[92] were carried out. Symmetric ω - 2θ scans along the [00.1] direction were calculated. Starting from the cubic phase, several model structures were considered, differing in the distribution and ordering of the vacancies.

XRD Simulations

From the distance between GST(222) and the broad peak at $Q_z = 3.27 \text{ \AA}^{-1}$ in the XRD profile (fig. 3.2), the lattice parameter along the c axis has been determined [formula (3) in chapter 2.2.1]. This gives $c_0 = 17.39 \text{ \AA}$, the building block in between vacancy layers (VLs), defined as a fully depleted Sb/Ge layer without structural rearrangement (see the model structure in fig. 3.6). The obtained c_0 value agrees perfectly with the experimental value given in literature for the metastable

225 phase^[14]. Note that according to Zhang *et al.*^[16], the Te-Te distance at the two sides of a VL decreases significantly with increasing degree of ordering (depletion degree of the gaps), till vdW gaps are formed in the most ordered trigonal phase. Therefore, in order to simulate our XRD spectra for the 225, 326 and 124 phases of GST, by using the Crystal Maker^[92] software package, several metastable cubic phases, depending on the distribution and ordering of the vacancies, were considered. The first considered structure was the metastable rocksalt cubic phase for the GST225, where Sb, Ge and vacancies are randomly distributed in the cation sublattice (see chapter 1.2.1).

The average occupancy for Ge and Sb is 0.392 while the vacancy concentration is 21.6 %. The simulated XRD spectrum exhibits the three Bragg reflections (111), (222), and (333) and no other additional peaks. In fig. 3.5 a) the simulation is reported in the Q_z region around the GST (222)-peak after a fine tuning of the GST cubic lattice parameter to fit the experiment, this giving $c = 6.01 \text{ \AA}$.

The next step consisted of introducing a more ordered distribution of vacancies, simulating the formation of VLs. If we consider the cubic structure along the [111] direction, the vacancy planes can be achieved by moving the vacancies (v) from every Sb/Ge/ v plane to each fifth Sb/Ge/ v plane until it is a complete vacancy plane. In fig. 3.5 b) the new structure is represented in the conventional trigonal lattice (the unit cell containing 3 formula units) where we can observe a sequence of Te and Sb/Ge/ v planes along the [00.1] direction with a VL every four Sb/Ge layers (VL model 1). The new structure can be considered as a superlattice of Sb_2Te_3 and GeTe in which the stacking sequence is still ABCABC as in the rocksalt structure. The simulated XRD is reported in fig. 3.5 a). The diffraction maxima are now indexed as (00. n) according to the trigonal unit cell reported in fig. 3.5 b). The XRD maximum (00.30) coincides with the (222) peak of the cubic rocksalt structure. However, the simulation's most important result is the appearance of a series of new maxima with $n = 3p$ (p is an integer), i.e. only diffraction peaks with n equal to a multiple of three appear. This is due to the fact that the unit cell is composed of three building blocks, stacked along the [00.1] direction and separated by the VLs, which are identical in the symmetric diffraction geometry. The presence of the vacancy planes gives rise to a superstructure from which additional maxima in the simulated XRD arise, and for this reason labeled as VLps. As in the cubic structure, the lattice parameter c of the model structure was adjusted to fit the (00.30) reflection of the simulated spectrum to the experimental peak, this producing $c = 52.19 \text{ \AA}$, where c is the whole trigonal cell for GST 225 ($c_0 \cdot 3$ unit blocks). The reflections at 3.27 and 4.00 \AA^{-1} in the experimental spectrum can be identified as the reflections (00.27) and (00.33) in trigonal notation, respectively; they can also be viewed as the satellite peaks of the superstructure containing the vacancy planes. Furthermore, the full width at half maximum (FWHM) of the VLps is very large if compared to the basic GST peak [(00.30) reflection].

To understand this point we simulated a new structure where we introduced a stacking fault of the vacancy layers by exchanging one of the vacancy planes with one of the adjacent Sb/Ge planes. In such a model a new periodicity along the c axis is introduced and the selection rule allowing only the (00.3 p) reflections is removed. The new simulated spectrum [VL model 1 SF in fig. 3.5 a)] exhibits two equally spaced peaks in between the peaks of the unfaulted structure. The model structures in fig. 3.5 b) represent ideal crystals while the simulations in fig. 3.5 a)

represent the XRD from ideally ordered phases. Therefore, the observed differences between the simulations and the experimental results can be explained if we assume a certain statistical disorder in the layer sequence which includes a distribution of stacking faults. This explains the observed FWHM of the VLps as well as the strong reduction of the higher order satellite peaks. In previous models an average occupation for Sb and Ge atoms in the planes in between the Te layers (with the obvious exception of the vacancy planes) was considered. This does not affect significantly the simulation of symmetric XRD along the $[00.1]$ direction. As an example of this aspect, a specific structure for the GST225 was modeled, in which the vacancy planes are fully depleted, the Sb/Ge planes are fully occupied and each Sb (Ge) atom is coordinated by four Ge (Sb) atoms, as in the model proposed by Da Silva *et al.*^[93]. The simulated XRD is shown in fig. 3.5 a) (VL model 2); no significant difference can be observed with respect to the VL model 1, with the exception of only tiny differences in the intensity of some reflections.

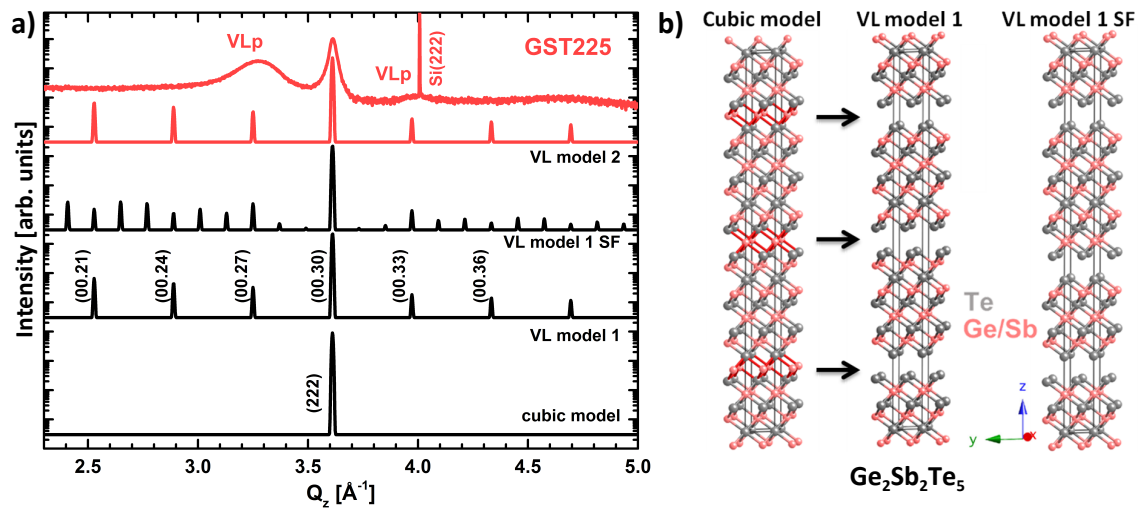


Figure 3.5: a) Experimental scan of the second order for crystalline GST225. The simulations performed by Crystal Maker are based on different models, as reported (see labels). b) Corresponding crystal structures for the several VL models employed. Reprints from^[94]

It is very important at this point, to remind that the introduction of stacking fault in the distribution of the vacancy layers can be seen as changing the size of the GST building blocks, i.e. introducing the periodicity of a new composition. This concept is clearly visible in the three reported model structures in fig. 3.6.

With this in mind, we can continue the general discussion on the interpretation of the additional peaks present in XRD profile in fig. 3.2. In particular, the simulated XRD profile for the three model structures of GST326, 225 and 124 are shown in fig. 3.6, where perfectly ordered distributions of vacancies were introduced to simulate the formation of fully depleted VLs for the phases 225, 326 and 124 of GST, as in the structures proposed by Da Silva *et al.*^[93]. The VLs generate a superstructure from which additional maxima in the simulated XRD profile emerge, henceforth called VLps. The reflections at $Q_z = 1.44, 3.27$ and 4.00 Å^{-1} in the GST experimental profile [black curve in fig. 3.2 a)] can be identified, respectively, as the reflections (00.12), (00.27) and (00.33)

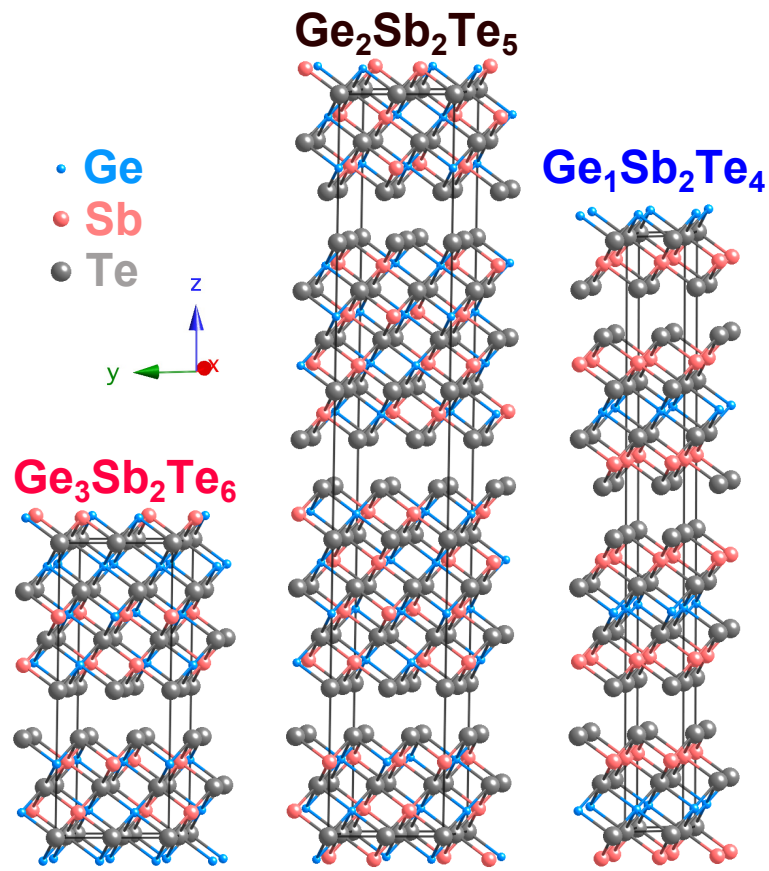


Figure 3.6: Crystal structures of GST326 (225) and [124].

of GST225 in trigonal notation. They can be viewed as the first order satellite peaks of the VL superstructure. By filling the VLs with Sb and Ge atoms, the VLps' intensity in the simulated profile were reduced and disappeared when the concentration of vacancies for each plane was less than 25 %. The full width at half maximum (FWHM) of the experimental VLps is very large if compared to the basic GST peak [(00.15) and (00.30) reflections]. The observed differences between the simulations (ideal crystals) and the experimental results can be explained if we assume a certain statistical disorder in the layer sequence, which includes a distribution of stacking faults (variable number of planes in between the VLs-as discussed in "XRD simulation" section) and a random distribution of vacancies among the planes. The stacking sequence of atomic (00.1)GST layers and the VLs are the main features that directly affect the symmetric XRD along the [00.1] direction. On the other hand, the presence of stacking faults and fluctuations in the vacancies occupation can be viewed as the coexistence of GST compositions other than 225 (see the structures in fig. 3.6). The first order satellite peaks of the various compositions (225, 326, 124) are very close to each other, explaining the observed FWHM of the VLps as well as the strong intensity reduction of the higher order satellite peaks. To take into account the relaxation of atoms at the VLs, DFT calculations by W. Zhang and R. Mazzarello were performed on the same GST structures of fig. 3.6. The two simulations (lower panel of fig. 3.2) agree very well in terms of the peaks position while they differ in the intensity (in particular of the (00.18) and (00.21) reflections).

A further upgrade in the simulation of XRD profiles which allows to take into account the compositional disorder, is obtained by the use of a Monte Carlo based method. In this case, random stacking of GST124, GST225 and GS326 blocks along the growth direction (as determined by STEM analysis on our samples)^[97] can be generated. The methods also allows to take into account in-plane disorder within the area probed by the X-ray beam. An example of this can be found in Zallo *et al.*^[98].

Courtesy of Dr. A. M. Mio, Dr. S. Privitera and Prof. E. Rimini (IMM-CNR Catania, Italy), the studied GST films were investigated using high-angle annular dark field scanning transmission electron microscopy (HAADF-STEM), corroborating the assumptions of our simulations.

A clear example of stacking faults and mixed phases is evident in fig. 3.7 where a HAADF-STEM image of a GST sample is presented. The film consists of domains with a (00.1) out-of-plane orientation with evident intensity modulations (dark lines), consistent with the presence of stacking faults associated with VLs and is observed every 7, 9 and 11 atomic planes (fig. 3.7). For GST225, 9 atomic planes are expected to form between two subsequent VLs, 11 for GST326 and 7 for GST124 (see fig. 3.7). From the intensity modulation in the profile the layers occupied by Te are clearly evidenced, while the intensity occupied by cations, indicates a mixed Sb/Ge occupancy. The STEM data corroborate the conclusions that our highly ordered samples are constituted by a GST alloy with 225 average composition reconciled with the 124 and 326 phases. Furthermore, both cubic and rhombohedral stacking can be identified (red and light blue boxes, respectively, in fig. 3.7). Both stacking coexist across the VLs and show a different degree of Sb/Ge depletion: atomic inclusions are visible in the gap in case of the cubic stacking. Te-Te layer distance upon the gap differs for the cubic (3.3 Å) and trigonal (3.0 Å) case, in accordance with Zhang *et al.*^[16]. In case of

the rhombohedral stacking, the VLs can more appropriately be called vdW gaps. This indicates that the cubic to trigonal transition is a continuous process where both cubic and rhombohedral stacking coexist with a high degree of vacancy ordering.

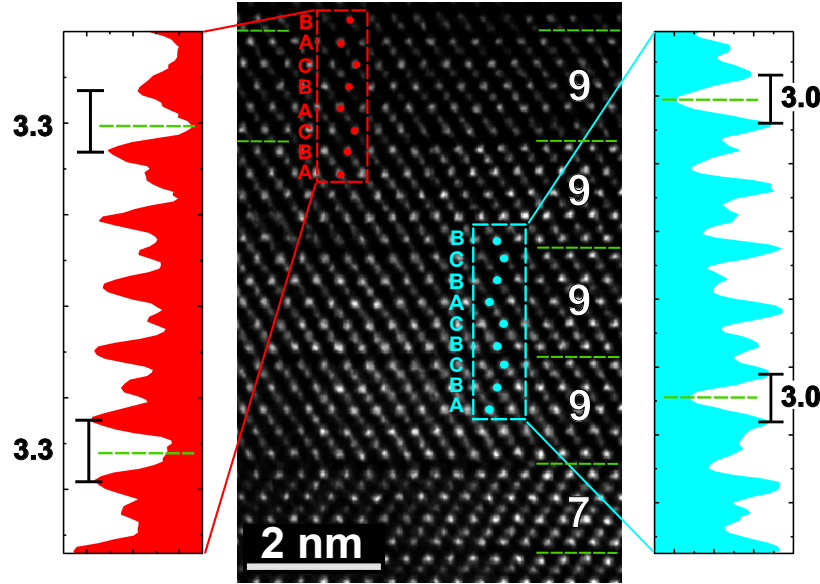


Figure 3.7: Cross-view [11.0] high resolution HAADF STEM micrograph of epitaxial (00.1)GST; VLs (dashed green lines) occur every 7-9 atomic layers. Cubic (red) and rhombohedral stacking (light blue) in respect to the Te sublattice is highlighted and corresponding integrated line profiles along the [00.1] direction are shown. Courtesy of Dr. A. M. Mio.

To summarize and conclude, through a combination of different experimental techniques combined to XRD simulations and DFT, highly ordered GST crystalline phase with vacancies arranged on (00.1) planes is achieved by MBE growth, which was so far only theoretically predicted^[16,93]. The possibility to assess vacancy ordering by a technique like XRD, presents the advantage that structural properties of GST can directly be compared to those of other large scale measurement techniques, facilitating the interpretations of physical phenomena (see for example chapter 4). Another important advantage, consists in the fact that it allows for exploration of different growth condition in order to tune the composition and the vacancy ordering. This aspect will be discussed in the following section.

3.1.2 Tuning of Composition and Ordering Degree

The understanding of the ordering process presented in previous the section, allows for the realization of a fine tuning of the ordering degree, which is presented in the following. Free parameters such as the fluxes of the Ge, Sb and Te constituent elements (Φ_{Ge} , Φ_{Sb} and Φ_{Te}) and the substrate temperature (T_{sub}) are varied. The interplay between composition, crystalline phase and ordering in GST grown on Si(111) is also discussed.

Considering the very low vapor pressure of Ge^[99] with respect to Te^[100] and Sb, Ge thin films are comparatively stable at temperatures where sticking of Te and Sb on the substrate is almost negligible. We thus expect GeTe to be easily incorporated into the alloy and not being the limiting species. A series of samples increasing Φ_{Ge} has been prepared, and all the other parameters were kept constant ($T_{\text{sub}} = 250\text{ }^{\circ}\text{C}$, $\Phi_{\text{Sb}} = 0.196\text{ nm/min}$ and $\Phi_{\text{Te}} = 0.37\text{ nm/min}$). In fig. 3.8 a superposition of XRD profiles around the GST(222) is shown. Each curve corresponds to a sample grown for different Φ_{Ge} , as given in the label, where the fluxes are normalized to the lowest one of 0.069 nm/min. Each curve presents a very sharp and intense GST peak around 3.6 \AA^{-1} attributed to the main Te-Te periodicity, and a second one much broader attributed to the VL periodicity (see 3.1.1). The VLp shifts toward lower Q_z for decreasing Φ_{Ge} , indication of a change in the main composition. From the distance between the two peaks, the lattice parameter c_0 is extracted and plotted in fig. 3.8 b). It is clear that within the Φ_{Ge} range explored, composition is varied from GST225 to GST326. Bulk values are reported as reference^[14]. In fig. 3.8 c) the nominal growth rate (GR) is compared to the experimental one for each used flux. Nominal GR is the sum of all the fluxes of the constituents, available from the calibration curves obtained as described in section 2.1. The experimental GR, is obtained by dividing the total thickness of each sample after deposition (as evaluated by XRR), by the growth time. Nominal and experimental GR are different due to desorption effects. Nominal GR increases linearly with Φ_{Ge} , instead the experimental GR decreases. This trend is not trivially linear. GST225 shows the highest experimental GR even if the lowest Φ_{Ge} is used. A possible reason might be a composition dependence of the GR. Unfortunately, a calculation of the effective GR taking into account the different compositions is not possible due to the fact that within our experiment it is not possible to know how much of each element flux is really incorporated in the film. QMS studies are needed for a better understanding of the effect.

Interestingly, the green curve in fig. 3.8 a) corresponding to the lowest Φ_{Ge} , presents not only a different composition, but also a more pronounced VLp if compared to the others, and even a second VLp at about $Q_z = 2.9\text{ \AA}^{-1}$ is detected. This is a clear indication that at low Φ_{Ge} , ordered vacancy layers between Te-Te layers can easily be formed (see fig. 3.6). A representative STEM micrograph (by Dr. A. M. Mio and Dr. S. Privitera) is shown in fig. 3.9 a) and displays the presence of vdW gaps having width of 2.7 and 2.9 Å, as indicated in the integrated profile. The shown micrograph is only an example of hundred micrographs showing in average the same result, indication of the fact that the sample (green curve) is in its t- phase. Please remember that in the ordered cubic phase, the vacancy gaps between Te-Te layers have larger width (3.3-3.5 Å) and therefore defined as VL since they are not yet vdW gaps (see fig. 3.7).

In order to investigate the phase of the grown samples, Raman spectroscopy is a very efficient characterization tool. A detailed Raman study of GST upon crystallization is presented and discussed in chapter 4.1.2, here, only the modes used for the identification of cubic and trigonal phases are considered. The most evident differences between c- and t-GST consist in modes appearing in the low energy range (30 to 50 cm^{-1}) and in the highest one (160 to 175 cm^{-1}). From literature it is calculated and observed^[101] that in the low range t-GST shows two distinct modes, while c-GST only one broad one; in the highest energy range instead, in the trigonal phase the characteristic cubic mode at $\sim 160\text{ cm}^{-1}$ turns off and a higher energy mode at $\sim 170\text{ cm}^{-1}$ turns

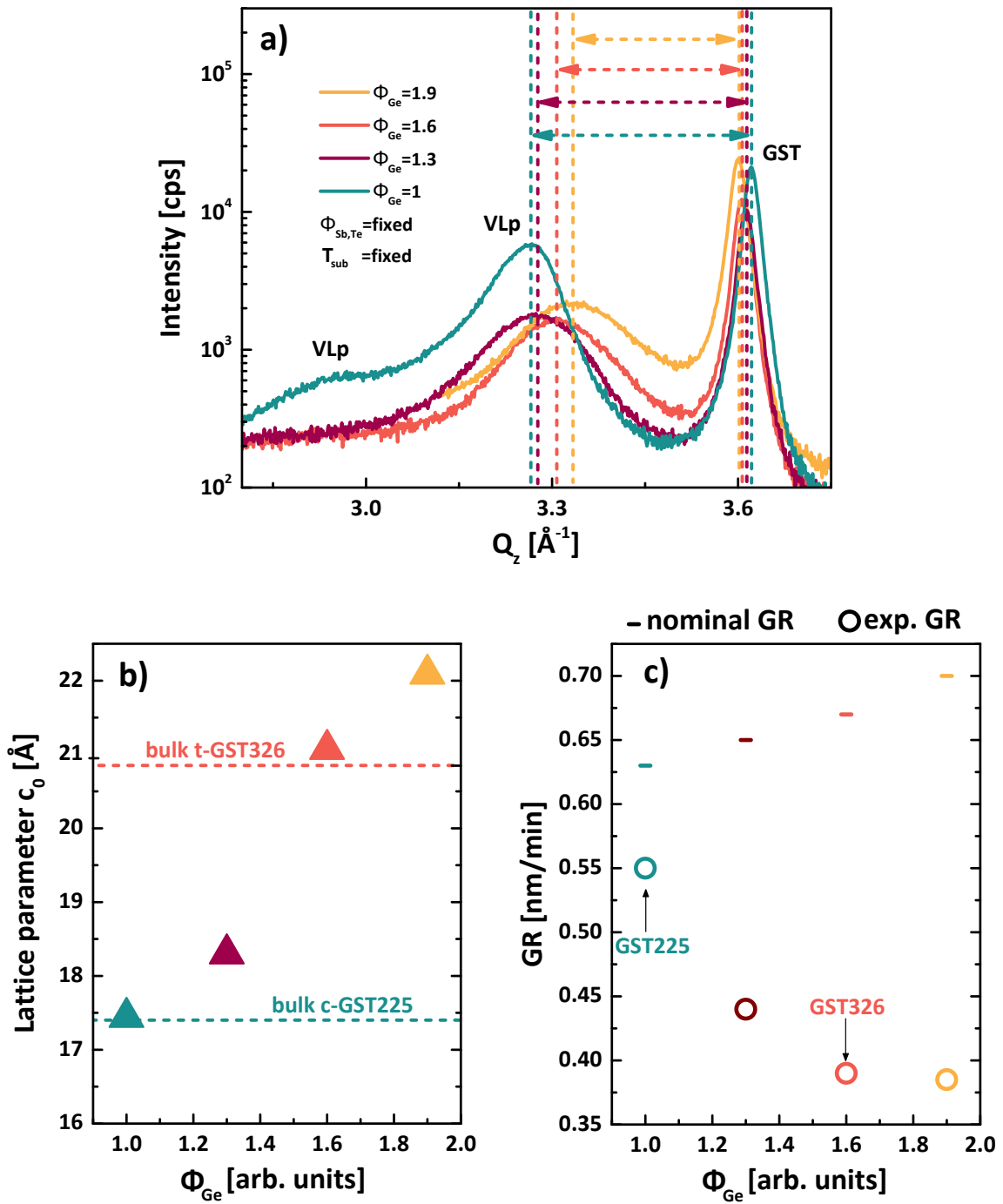


Figure 3.8: GST samples grown at different Φ_{Ge} : a) Superimposition of XRD profiles around second order GST peak; b) Lattice parameter as a function of Ge flux, bulk references can be found elsewhere^[14]; c) Nominal and experimental GR.

on^[102]. In fig. 3.9 b) Raman spectra of the different samples of fig. 3.8 a) are shown. By comparison it emerges that the yellow and green curve, which correspond to the highest and lowest Φ_{Ge} used, can be assigned to c- and t-GST, respectively^[101,102]. The red curve presents both characteristic modes, indication of the fact that the sample has mixed phases, which is often the case during MBE growth.

In a ternary alloy the three constituent elements are interdependent. Indeed, by varying the Φ_{Ge} , the flux ratios between the elements ($\Phi_{\text{Te/Ge}}$ and $\Phi_{\text{Sb/Ge}}$) are changing consequently. In the former experiment, $\Phi_{\text{Te/Ge}}$ changes from 2.8 to 5.4, while $\Phi_{\text{Sb/Ge}}$ changes from 1.5 to 2.8. $\Phi_{\text{Te/Sb}}$ remains constant at 1.9. From a more specific growth theory point of view, we can say that the epitaxial growth is performed at substrate temperatures (T_{sub}) high enough to ensure good crystalline quality of the deposited film. This is achieved if the impinging atoms have enough surface mobility to arrange on energetically favorable lattice positions. Together with surface diffusion mechanisms, also adsorption or desorption of the impinging atoms is possible. And the interplay between all these fundamental growth mechanisms is influenced by the flux ratios (see section 2.1).

These results suggest that the excess of Te which is not necessary for the compositional arrangement, play an important role in the ordering process, especially if we recall (see chapter 1.2) that the formation of vacancies in resonantly bonded compounds is a mechanism to get rid of excess electrons. In order to validate this assumption, a series of samples are grown at different Φ_{Te} keeping the other parameters fixed ($T_{\text{sub}} = 250\text{ °C}$, $\Phi_{\text{Sb}} = 0.196\text{ nm/min}$ and $\Phi_{\text{Ge}} = 0.37\text{ nm/min}$). In fig. 3.10 a) a superposition of symmetric ω - 2θ scans for such samples is shown. Curves are displayed with an offset for clarity. Φ_{Te} are normalized to the lowest one of 0.18 nm/min. By increasing Φ_{Te} (red to light blue curve), XRD curves visibly change; if we focus on the second order of the profiles ($2.8\text{--}3.8\text{ Å}^{-1}$), the VLp shape, i.e. FWHM and intensity, is different. A clear shift toward lower Q_z for increasing Te flux is visible, with consequent change of sample composition, as reported in fig. 3.10 b). Compositions from GST225 to GST124 are obtained varying Φ_{Te} . In addition the VLp looks more or less symmetric with increasing Φ_{Te} ; this is attributed to the relative height of the composing peaks related to the three different compositions (124, 225, 326), indication of compositional disorder (see discussion in section 3.1.1). Expected positions of VLp are shown as guide to the eye for GST326, 225 and 124 from higher to lower Q_z . When the VLp is asymmetric, the main composition is evaluated by fitting the VLp with multi-gaussian peaks fixed at the expected positions for the three compositions, and choosing the one contributing the most.

A clear example of mixed composition are the samples grown with $\Phi_{\text{Te}} = 1.3$ and 2.3, where the wide VLp clearly results as a Fourier envelop of a main peak and a second one appearing as a shoulder on the right. The change in FWHM and intensity of the VLp with increasing Φ_{Te} indicates an increase in vacancy ordering degree, which is particularly evident in the curve corresponding to the highest flux [light blue in fig. 3.10 a)], characterized by multiple orders of VLps. Also the sharp GST peak around 3.6 Å^{-1} consistently shifts toward higher Q_z , indication

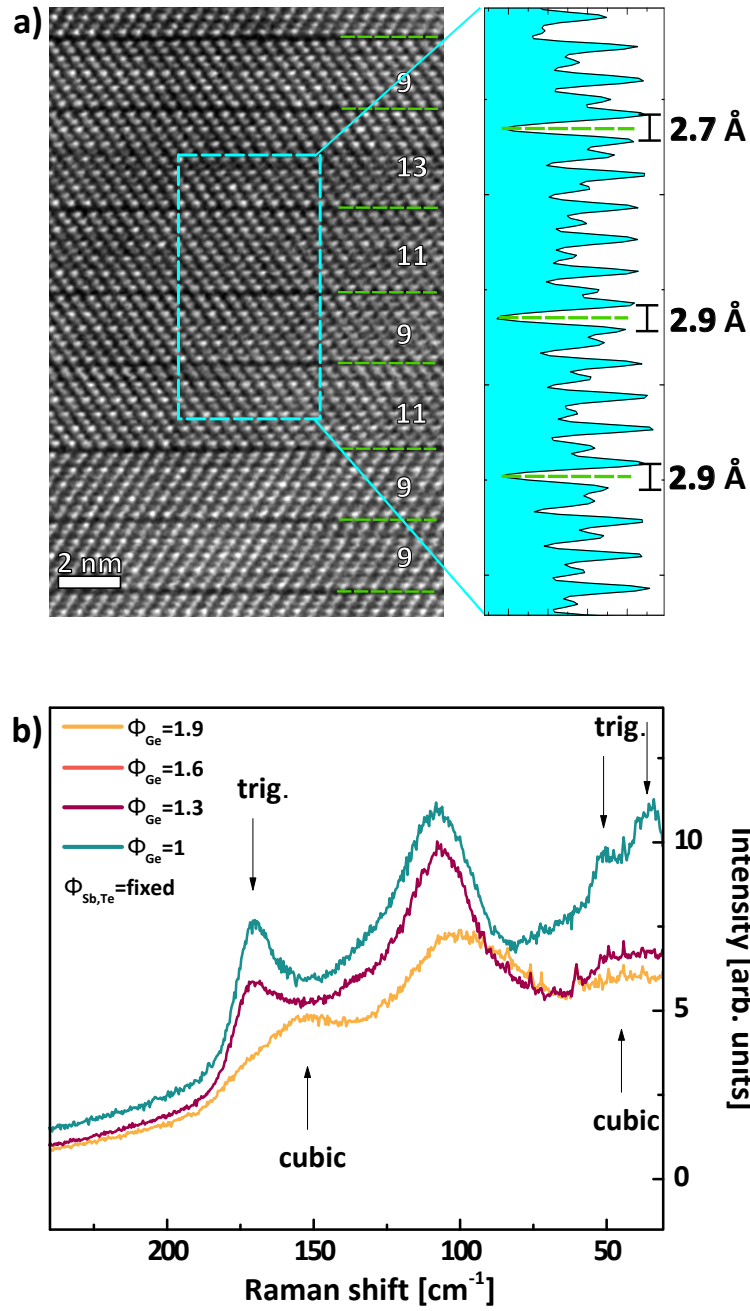


Figure 3.9: a) Cross-view [11.0] high resolution HAADF STEM micrograph of epitaxial (00.1) GST, vdW gaps (dashed green lines) occur every 9-13 atomic layers, integrated line profiles along the [00.1] direction is shown with highlighted vdW gaps spacing. Courtesy of Dr. A. M. Mio; b) Comparison of Raman spectra for the samples grown with different Φ_{Ge} [same color code as in fig. 3.8 a)].

of smaller average Te-Te layer distance for increasing ordering, consistent with literature^[93]. The ratios between the fluxes in this series of samples changes from $\Phi_{\text{Te}/\text{Ge}} = 2.6$ to 8.4, while $\Phi_{\text{Te}/\text{Sb}}$ varies from 0.9 to 3. $\Phi_{\text{Sb}/\text{Ge}}$ stays constant at 2.8.

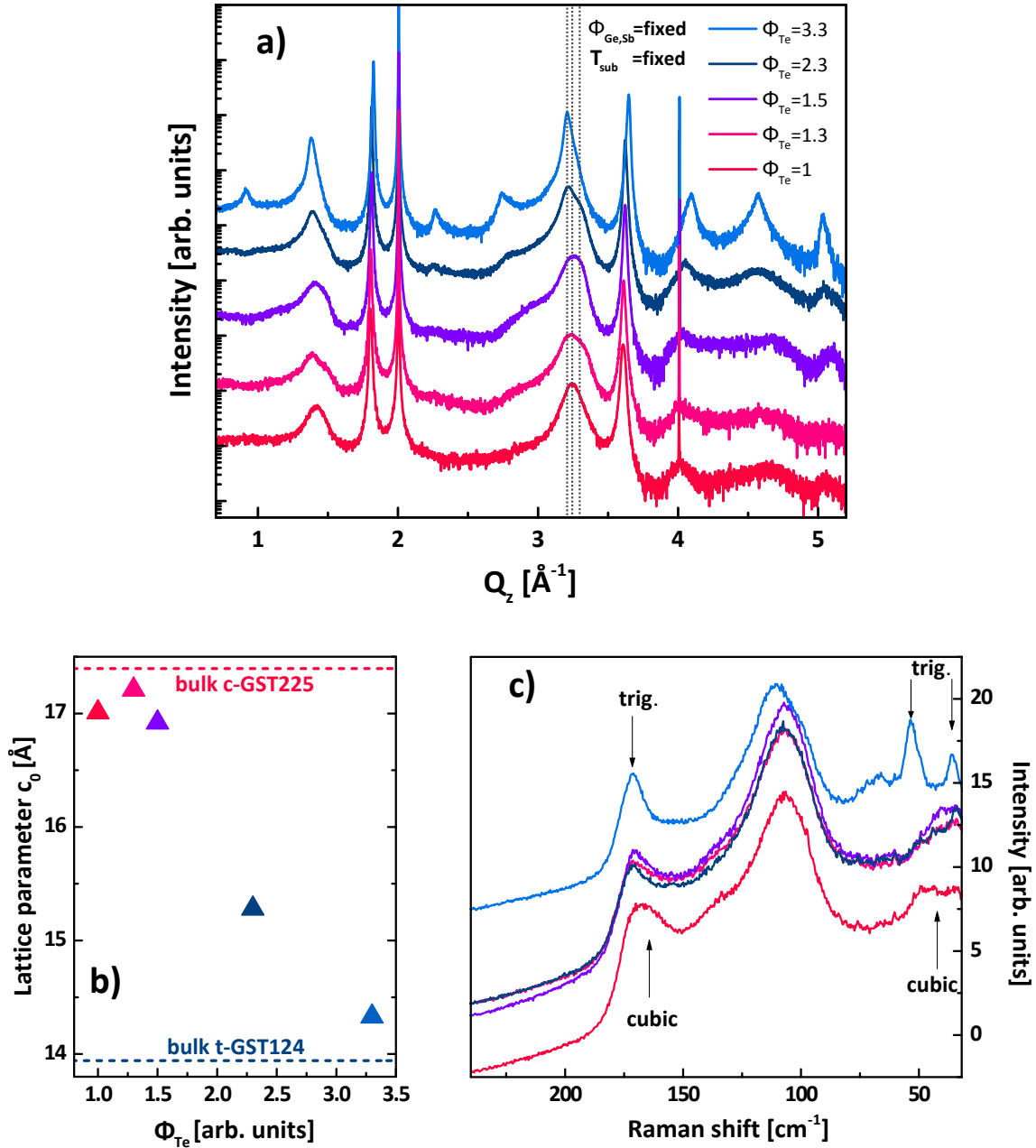


Figure 3.10: GST samples grown at different Φ_{Te} : a) Superposition of XRD profiles, expected positions of VLP are shown as guide to the eye for GST326,225 and 124 from higher to lower Q_z ; b) Lattice parameter as a function of Φ_{Te} , bulk references can be found elsewhere^[14]; c) Comparison of Raman spectra.

The Raman spectra corresponding to the lowest and highest Φ_{Te} are shown in fig. 3.10 c). For the lowest flux (red curve), no double peak at low wavenumber is present and the characteristic cubic mode at 160 cm^{-1} is still dominant. The spectra corresponding to the highest Φ_{Te} instead, presents all the modes typical of a good trigonal phase. Again the intermediated curves can be considered owing to mixed phases not yet fully trigonal.

Also the effect of the variation of the substrate temperature on the GST film was investigated. T_{sub} was lowered from 250°C to 120°C . The three cells fluxes were kept constant at $\Phi_{\text{Ge}} = 0.055 \text{ nm/min}$, $\Phi_{\text{Sb}} = 0.193 \text{ nm/min}$ and $\Phi_{\text{Te}} = 0.252 \text{ nm/min}$. For the lowest $T_{\text{sub}} = 120^\circ\text{C}$, a tuning of the fluxes was necessary to avoid amorphous growth. Fluxes were considerably reduced to $\Phi_{\text{Ge}} = 0.122 \text{ nm/min}$, $\Phi_{\text{Sb}} = 0.128 \text{ nm/min}$ and $\Phi_{\text{Te}} = 0.235 \text{ nm/min}$. XRD profiles are plotted in fig. 3.11 a) with an offset for clarity. GST films change composition as suggested by the shift of the VLP in respect to the GST reflection, which is itself slightly shifting toward higher Q_z for decreasing T_{sub} . In fig. 3.11 b) lattice parameter c_0 is plotted as a function of T_{sub} . Stoichiometric GST326 and GST225 together with non stoichiometric compositions are obtained (see bulk references in graph^[14]).

Raman measurements in fig. 3.11 c) is used to asses the phases. The samples grown at 250°C and 200°C are c-GST, with very pronounced modes, the sample grown at 120°C instead, shows characteristic spectra of t-GST. The sample grown at 180°C shows a splitting of the low frequency mode into two, even if no high frequencies trigonal mode is visible at all, we can tentatively assign it to a mixed phase.

In general, a decrease of substrate temperature implies an increase of the sticking coefficient of each element. In this case the element that is mostly affected is Te. Thus, by decreasing the growth temperature, there is an increase of Te flux participating to the adsorption. In other words, with decreasing T_{sub} , both $\Phi_{\text{Te/Ge}}$ and $\Phi_{\text{Te/Sb}}$ increase, the last in particular could be the key point in the ordering process during growth.

For completeness, a series of samples with T_{sub} between 200 and 280°C has been prepared. In this case fluxes of $\Phi_{\text{Ge}} = 0.069 \text{ nm/min}$, $\Phi_{\text{Sb}} = 0.196 \text{ nm/min}$ and $\Phi_{\text{Te}} = 0.37 \text{ nm/min}$ ($\Phi_{\text{Te/Ge}} = 5.4$, $\Phi_{\text{Sb/Ge}} = 2$, $\Phi_{\text{Te/Sb}} = 1.9$) were used. Fig. 3.12 a) shows the respective XRD profiles. It is found that between 230 and 260°C the samples show similar compositions and trigonal phase, as can be clearly seen in fig. 3.12 b) and c). For very high T_{sub} instead, GST becomes cubic (orange curves) probably due to an increase of disordering during the growth. At 200°C the sample is still in the trigonal phase, even if in the low energy range of the Raman spectrum the two peaks are less defined than for the samples grown at 250 and 260°C .

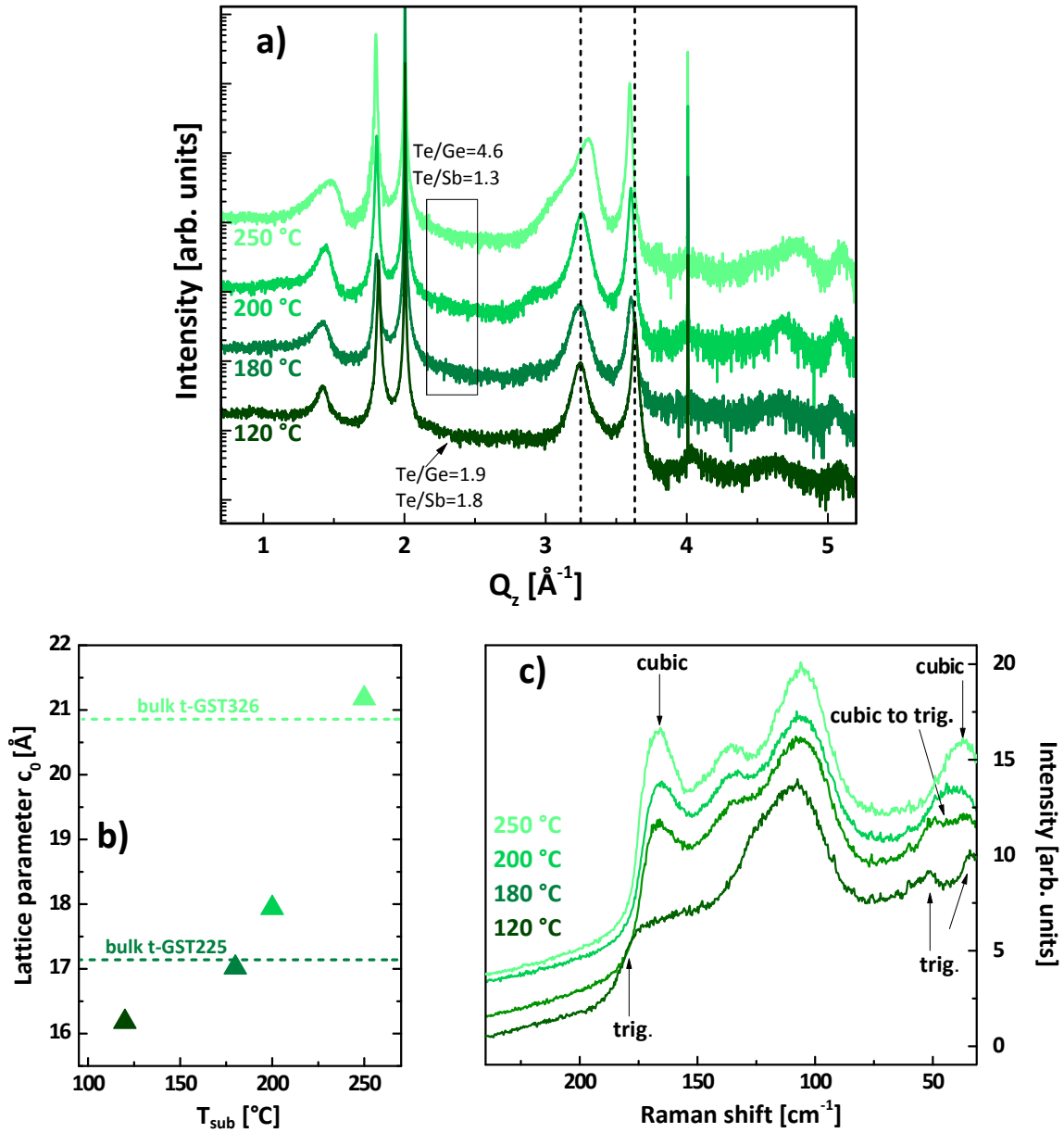


Figure 3.11: Samples grown at different T_{sub} : a) Superposition of XRD profiles; b) Lattice parameter as a function of T_{sub} , bulk reference found elsewhere^[14]; c) Comparison of Raman spectra.

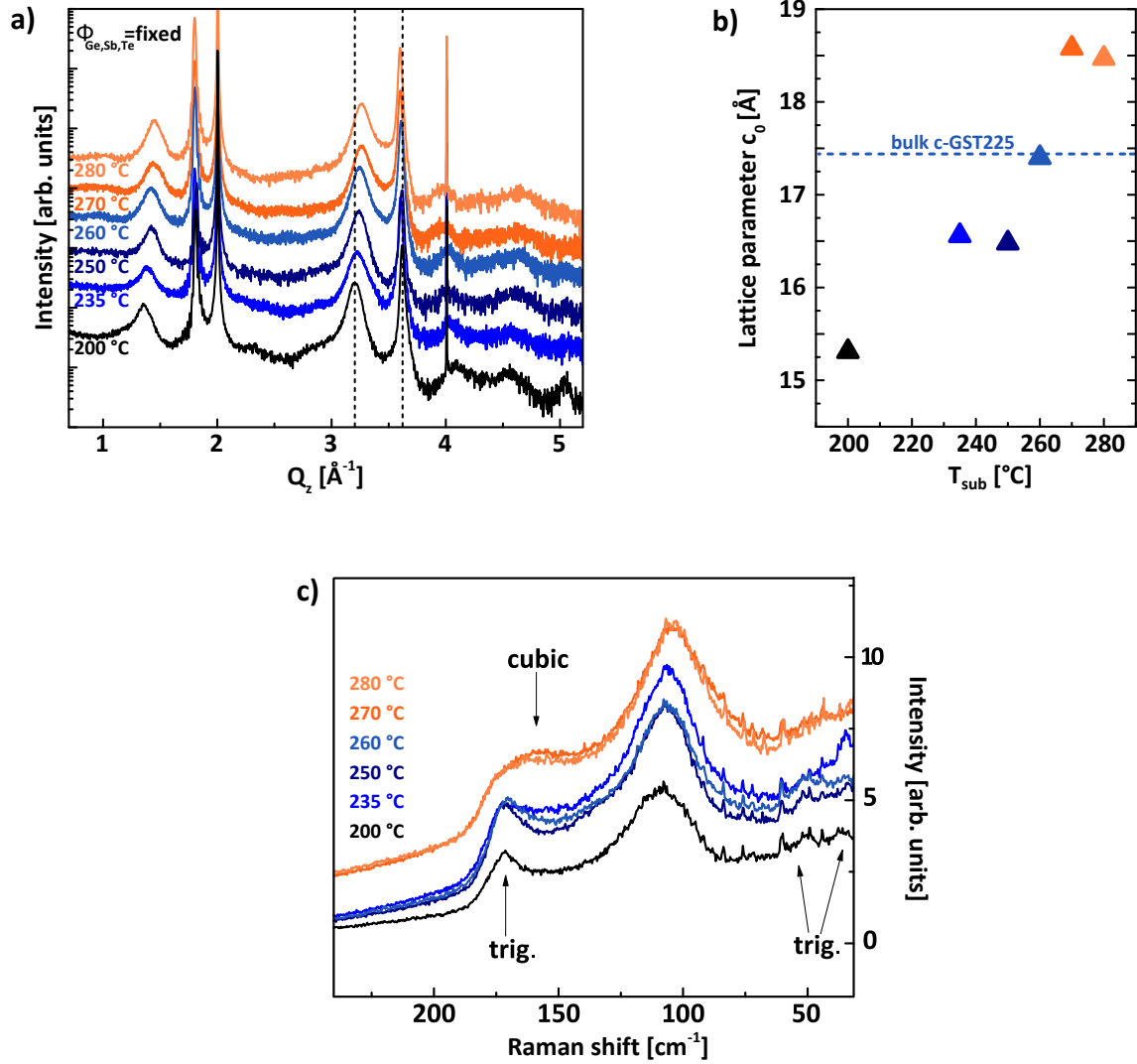


Figure 3.12: Samples grown at different T_{sub} : a) Superposition of XRD profiles; b) Lattice parameter as a function of T_{sub} , bulk reference found elsewhere^[14]; c) Comparison of Raman spectra.

Discussion of the Results and Phase Diagram Realization

In the range of T_{sub} investigated, Te is very volatile if compared to Ge. Thus, it results that Te and T_{sub} are strongly interlinked. For this reason, a phase diagram with Φ_{Te} as function of T_{sub} (x-axes) is shown in fig. 3.13. All reported samples are comparable in terms of Φ_{Ge} and Φ_{Sb} . The samples are discriminated in terms of phase (c-, mixed- and t-GST) and composition.

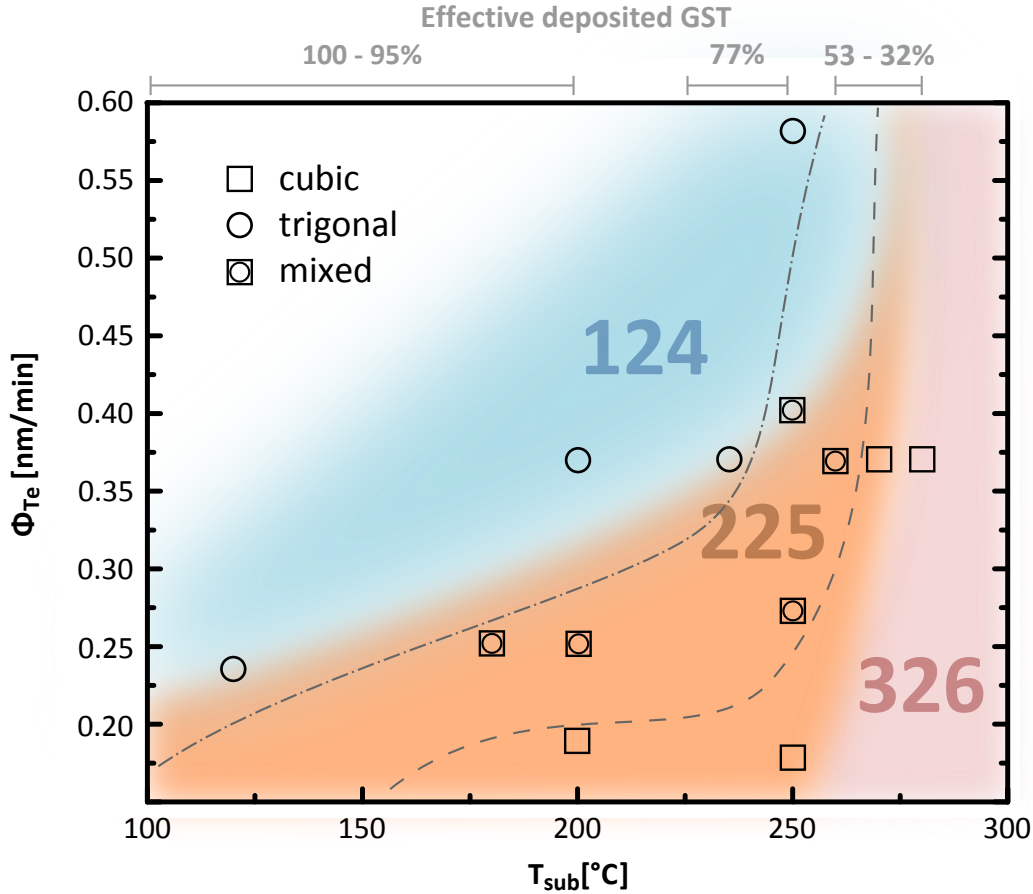


Figure 3.13: Phase diagram displaying crystalline phases and composition of GST upon Φ_{Te} and T_{sub} variation. Square symbols stay for cubic, circles for trigonal phase and mixed phases are represented by both symbols. Dashed and dot-dashed lines are drawn as a guide to the eye to delimit the different phase regions. GST124, 225 and 326 are distinguished by three colors, blue, orange and pink, respectively. On the top part of the diagram, the effective deposited GST material is given in percentage in respect to the nominal thickness.

Three main regions can be identified depending on the crystalline phase. Squares are associated to samples in the cubic phase, while circles to the trigonal phase. Mixed samples are represented by both symbols. Dashed and dot-dashed lines are drawn as a guide to the eye to delimit the different phase regions. For completeness, the effective deposited GST in the different T_{sub} windows is reported on top of the diagram. This quantity is calculated by dividing the total thickness of each sample by the growth time, then the percentage is given depending on the expected nominal GR. I recall that nominal GR is calculated by summing the fluxes of the three elements.

In a large range of T_{sub} range (180 to 250 °C), vacancy ordering is improved for increasing Φ_{Te} (transition c- to t-GST). Increasing T_{sub} a higher Φ_{Te} is necessary to implement Te-Te planes. In fact, considering Φ_{Te} of 0.37 nm/min, the samples are c-GST at $T_{\text{sub}} > 250$ °C and transform to t-GST lowering T_{sub} .

For even lower Φ_{Te} , it is more difficult to maximize the ordering in the samples, e.g. at $\Phi_{\text{Te}} \sim 0.25$ nm/min there is a larger growth window in which mixed phase is obtained. The stable phase is obtained only at $T_{\text{sub}} = 120$ °C. Particularly evident it is the case of the samples grown with $\Phi_{\text{Te}} < 0.20$ nm/min, for which only the c-GST is obtained.

Both the Φ_{Te} and T_{sub} experiments strongly suggest that it is the amount of Te flux governing the kinetic during the GST growth, in particularly in terms of ordering degree of the samples. A deficit of Te leads to a growth in which disorder prevails on order, with more favorable cubic phase. Please note that in this phase diagram we are discussing ordering in terms of crystalline phases (cubic and trigonal), without going into each crystalline phase and specifying the degree of ordering, which has been already discussed in chapter 4. It is noteworthy to clarify that the presence of mixed phases in some regions of the growth windows is not surprising, due to the fact that the energy difference between highly ordered cubic GST and trigonal GST is very small (~ 5 meV^[16]).

If we now focus on the compositions, several considerations can be done. Also in this case three different regions can be identified. Stoichiometric GST124, 225 and 326 are obtained and can be distinguished in the diagram by blue, orange and pink colored regions, respectively. It is important to note that samples with mixed compositional components are also obtained, and are represented on the boundaries of the colored regions in fig. 3.13; these boundary regions are not sharp, probably due to the fact that in these cases, the growth kinetic is not decisive for driving the growing GST into one specific favorable composition. Therefore, the GST intrinsic compositional disorder results favored, as introduced in chapter 3.1.1.

Within the range of the choosen growth parameters, GST225 results to be the most favorable composition, followed by GST124 and GST326. GST225 is mostly obtained in its metastable or mixed crystalline phases, GST124 instead, is in trigonal phase. Interestingly, similar result has been observed during annealing of a-GST225 (see Bragaglia *et al.*^[103]) which crystallizes into metastable c-GST225 first, and then t-GST124, again suggesting the stability of such composition in the most ordered phase. This finding is in agreement with literature based on poly-GST^[15], in which segregation of GST124 starting from a GST225 composition has been reported as a mechanism to lower the total energy of the system toward the trigonal phase. It is now meaningful to specify that the effect of temperature in the MBE growth and annealing experiment cannot be trivially compared. Vacuum conditions are completely different in the two cases, e.g. MBE deposition happens in UHV conditions, while annealing is performed under Nitrogen flux. During the annealing experiment, a sample with a given composition is annealed for increasing T_A , and the effect of the temperature is mostly to activate diffusions of the elements, which is dominant if compared to desorption. Elements diffusivity, together with the overcoming of the phase transitions activation energies, lead to an increase of ordering degree in annealed GST, till it turns into its trigonal phase. Instead, during the MBE growth, asymmetric desorption of the three elements

and their binary molecules, is expected to play a more significant role for increasing temperature, if compared to diffusion, adding a complicated kinetic component to the thermodynamic of the GST system. Therefore, the independence of the result on the fabrication technique might be a stronger demonstration of the fact that GST124 is the most stable composition in the trigonal phase.

If the compositional change is studied depending on the Φ_{Te} , it emerges that for fixed substrate temperature, increasing the Te flux leads to Sb_2Te_3 rich compositions in the order 326, 225 and 124. In table 3.1, the theoretical atomic percentage of the Ge/Sb/Te elements in GST compounds is listed. If we look at the change of atomic content within the three different compositions, we clearly see that the Te is changing the less, if compared to Sb and in particular Ge, which decreases from 27.27 % in GST326 to 14 % in GST124.

Compositions	at. % Ge	at. % Sb	at. % Te
GST124	14.28	28.57	57.14
GST225	22.22	22.22	55.56
GST326	27.27	18.18	54.45

Table 3.1: Theoretical atomic percentage of Ge/Sb/Te elements in GST compounds.

Coming back to the MBE growth, an explanation of the GST composition formation and of how the ordering take place is desirable. For a quantitative analysis of the microscopic growth processes, the use of a QMS could help to do specific assumption on the main mechanisms going on during the deposition, therefore useful growth parameters could be obtained by solving rate equations, which take into account the growth kinetics in specific conditions. The reliability of the same parameters would be further tested by comparing QMS data with expected one. Unfortunately, a QMS was not available for this thesis work. Nevertheless, in a previous study^[88,104], desorption rate of Ge, Sb, Te atoms and their binary molecules GeTe and Sb_2Te_3 have been measured. For convenience of the reader, a reprint of the desorption curves is shown in fig. 3.14. The epitaxial growth of GeTe and Sb_2Te_3 is between 200-260 °C, basically at T_{sub} where Sb and Te atoms singularly do not stick, but as a molecule they remain stable on the surface to form epitaxial layers. Ge atoms instead, would have sticking coefficient which can be assumed to be ~ 1 if evaporated alone [see fig. 3.14 b)]. In particular, at $T_{\text{sub}} = 250$ °C, GeTe molecules have a desorption rate of ~ 30 %, Ge acts as growth limiting species and a stoichiometric compound is formed as long as an excess of Te is present. Sb_2Te_3 instead, has a higher desorption rate of ~ 80 %. Based on these data, it emerges that an excess of Te flux respect to the Ge and Sb ones has to be used when the ternary alloy is grown. In other words, the choice of the elemental flux ratios to obtain the different GST compositions is not trivially determined by mathematical arguments, therefore a study of calibration using different Φ_{Te} is necessary. It is reasonable to assume that when the Ge, Sb and Te cells are open, for a given amount of Ge flux, a given amount of Te is quickly used to form Ge-Te molecules, all the remaining Te flux is used to form Sb-Te which amount determines

whether the final GST composition is more Sb_2Te_3 or GeTe rich (see table 3.1) and consequently the ordering degree. These results suggest that the growth kinetic in GST is strongly determined by the Φ_{Te} .

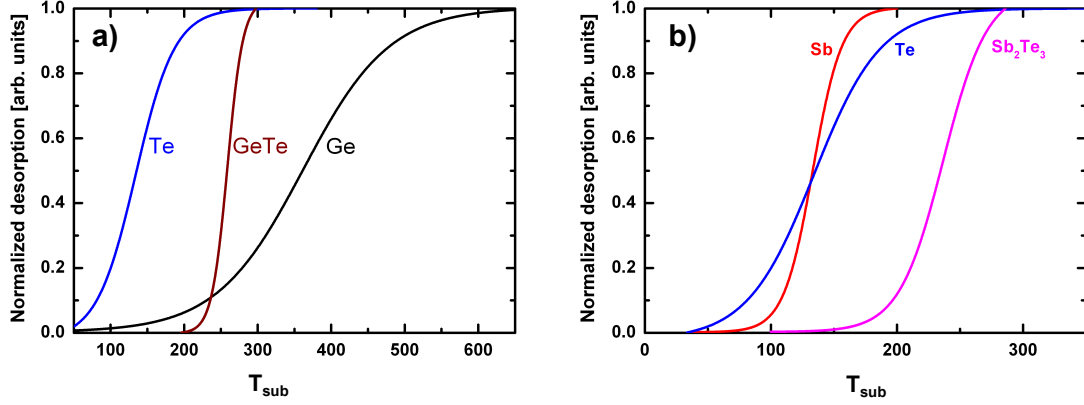


Figure 3.14: a) Sticking/desorption curve for Ge, Te and GeTe as observed by a QMS. b) Sticking/desorption curve for Sb, Te and Sb_2Te_3 . The maximum desorption is normalized to 1. Reprints from^[104].

As a general remark of the study, compositions and ordering in the MBE grown GST result to be not completely decoupled: Sb_2Te_3 rich compositions are easier to be grown into their stable crystalline phase if compared to the GeTe rich ones. Nevertheless by directly changing the Te flux, or indirectly if substrate temperature is modified, it has been possible to obtain different growth windows in which compositional tuning and different crystalline phases can be fabricated.

***In situ* RHEED Monitoring of the Growth**

In situ RHEED has been employed withing this study and resulted particularly useful to monitor the substrate reconstruction state before growth (see upper panels in fig. 3.15), and the GST film in terms of crystallinity at different stages of the deposition. In fig. 3.15, RHEED images corresponding to samples grown with different Φ_{Te} are shown as indicated by label. Three different stages of the growth are shown: Beginning of the deposition after 90 sec [images a), d), g), l)], intermediate stage at which interesting changes in the growth dynamics were observed [see time label in b), e), h), m)] and end of the growth after 2 h [c), f), i), n)]. RHEED images along the azimuth $\langle 11-2 \rangle$ are shown for the first three samples (from row one to three) and along $\langle 1-10 \rangle$ for the last one, for completeness. Initial Si surfaces are reported in the upper panel for both azimuths (see labels), showing well defined RHEED reconstruction patterns with Kikuchi lines indicating high quality of the substrate surface.

In all the images of fig. 3.15 acquired after 90 sec deposition [a), d), g), l)], it can be observed that GST is already deposited on the substrate, since the Si reconstruction is not visible anymore.

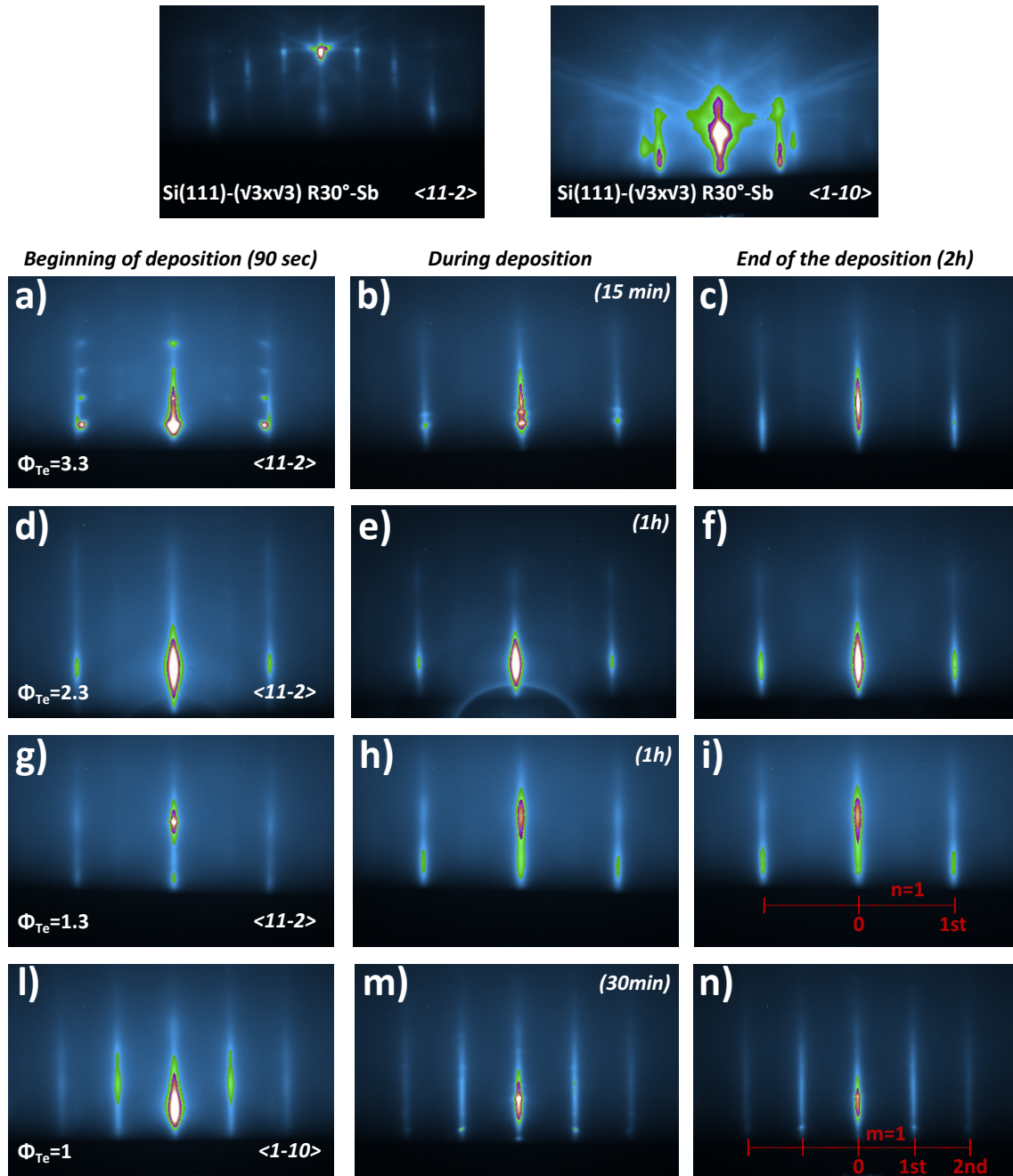


Figure 3.15: RHEED images of Si(111)-($\sqrt{3} \times \sqrt{3}$)R30°-Sb reconstruction along $\langle 11-2 \rangle$ and $\langle 1-10 \rangle$ azimuths. RHEED images of four GST samples grown at different Φ_{Te} (upper panels) for beginning of deposition [a), d), g), l)], intermediate stage [b), e), h), m)] and end of deposition [c), f), i), n)]. Red labels are guide to the eye indicating Laue orders along the two azimuths superimposed to RHEED images i) and n).

To estimate the GR of those samples, even if for excess, it is useful to consider that the highest nominal GR expected is 0.85 nm/min at RT, which becomes 0.65 nm/min taking into account the 77 % effective GST deposition at 250 °C (see fig. 3.13). The RHEED patterns appear streaky in d), g) and l), indication of a smooth surface. However, if the surface contains large smooth islands with monolayer range roughness, the RHEED intensity will still show a streaky pattern but with some intensity modulation. If we look carefully at the RHEED streaks in g), an intensity modulation is visible, and could indicate that the growth is actually proceeding by coalescence of big flat islands. Completely different it is the initial stage of deposition of the sample grown with $\Phi_{\text{Te}} = 3.3$. RHEED pattern shows intense spots on top of a streaky pattern, indication of a growth process dominated by three-dimensional (3D) structures. Interestingly, for the same sample, during deposition (15 min) in b), the film growth process seems to change, with a consistent 3D pattern reduction favoring a bi-dimensional (2D) smooth growth. At the end of the growth in c), the film shows a very good streaky pattern, indication of a smooth film. The GST samples grown with intermediate Φ_{Te} of 2.3 and 1.3 display a streaky RHEED pattern till the end of the growth. The sample grown with the lowest flux ($\Phi_{\text{Te}} = 1$) instead, shows a change in the growth regime after 30 min, as can be seen by comparing RHEED patterns l) and m). Spots appears on top of the streaks, indication of rough surface probably due to a 2D-3D transition during the growth. Also in this case, the film quality recovers significantly toward the end of the growth. From the RHEED pattern stability it is possible to identify a growth window for Φ_{Te} between 1.3 and 2.3. Within this growth window, high quality GST with different degrees of ordering, as found by the Raman and XRD study shown in fig. 3.10 can be obtained. Therefore, *in situ* RHEED results a powerful technique for monitoring the growth of GST. Similar *in situ* RHEED studies have been performed for the other series of samples (not shown).

Another interesting consideration concerns with the identification of all RHEED streaks. From the streak position analysis along $\langle 11-2 \rangle$ and $\langle 1-10 \rangle$ azimuths, a clear 1×1 GST reconstruction can be identified, according to the surface reconstruction nomenclature " $n \times m$ ", where n and m are the number of streaks within the first Laue order that can be observed along the two different azimuths. A red scale as guide to the eye with indicated Laue orders is superimposed to RHEED images in fig. 3.15 i) and n); $n = 1$ and $m = 1$ along azimuth $\langle 11-2 \rangle$ and $\langle 1-10 \rangle$ are also shown. Interestingly, by careful observation of RHEED images taken along azimuth $\langle 11-2 \rangle$, additional weak streaks can be identified within the first order Laue diffraction for some samples [see fig. 3.15 d) and g)]. Nevertheless these streaks are not equidistant from the 0 and 1st order, but actually correspond to the same distance of the $m=1$ streak observed along the azimuth $\langle 1-10 \rangle$. In other words, a very faint contribution of streaks characteristic of one azimuth ($\langle 1-10 \rangle$) is visible also along the other azimuth ($\langle 11-2 \rangle$). From previous works^[89,104], it is known that the additional streaks are due to the contribution of in-plane 30° rotational domains which are expected to contribute to the RHEED pattern, as shown by the Ewald sphere construction in fig. 3.9 of Perumal's thesis works^[104]. If bulk sensitive technique such as XRD is used, they are not visible. Only if synchrotron light is employed, they are accessible, as shown in fig. 3.19 of the same work^[104]. Remarkably, the presence of such domains compared to the unrotated is less than 1 % (based

on XRD peaks relative intensity calculation of fig. 3.9 in Perumal's thesis^[104]). Thus, conventional laboratory XRD ϕ -scan is not able to resolve such a small percentage of rotated domains. In contrast, RHEED proves to be a highly sensitive technique.

3.2 Fabrication of GeTe/Sb₂Te₃ Chalcogenide Superlattices

Within this thesis work, GeTe/Sb₂Te₃ based CSLs have been fabricated in order to be investigated dynamically on ultrafast time scale from our group and collaborators. The epitaxial CSL are grown based on a previous study which has been developed within the thesis work of R. Wang^[52].

The principle of growth consist in stacking together the two materials, i.e. GeTe and Sb₂Te₃ on a Si(111) substrate. Sb₂Te₃, due to its intrinsic tendency to texture in the out-of-plane direction, owing to its 2D nature, is reported as the ideal "buffer layer" for superlattices growth^[105]. By MBE, due to the epitaxial option, CSLs growth could also be initiated by GeTe, but lower interface roughness and narrower XRD peaks were still obtained for the CSL starting with Sb₂Te₃^[52]. As a result, these films possess the highest degree of ordering achievable experimentally, with interfaces that are clearly imaged using HAADF-STEM, and the individual atomic columns discriminated by their isotopic mass^[54]. Combined with more global characterization methods, such as XRD and Raman, the tendency of GeTe and Sb₂Te₃ to intermix into GST at the interface has been demonstrated^[52,54]. This result suggests how thermodynamically unlikely it is for the two materials to maintain a clear and well defined interface between them, as opposed to what is suggested in the existing models in the literature^[48] (see chapter 1.3.1).

In literature it is reported that the most efficient CSLs in terms of switching performances, are the one in which 1 nm of GeTe is intercalated within 3 nm Sb₂Te₃, i.e. one QL^[106]. Since the phase-change properties of CSLs are predicted to be linked to the interfaces between GeTe and Sb₂Te₃, for this thesis work, different CSLs have been grown by changing the staking of GeTe and Sb₂Te₃, in order to reduce the thickness of each SL period, increasing the proportion these interfaces occupy in the film. An example of growth scheme is given in fig. 3.16.

Before growing a GeTe/Sb₂Te₃ heterostructure, the two binary constituents need to be calibrated. This means that for fixed growth temperature and constituent fluxes, the deposition time has to be adjusted to obtain the desired thickness for GeTe and Sb₂Te₃ films. At this point the two materials can be staked on top of each other. In fig. 3.16 the schematic of the growth process is illustrated. On the left of the figure the three Ge, Sb and Te fluxes are reported. Within each constituent layer, Sb₂Te₃ (blue) and GeTe (orange) on top of the figure, the presence of the fluxes is indicated by the presence or not of different colors (gray for Te, light blue for Sb and yellow for Ge). On the bottom, an axis indicating the growth time, or in other words the opening time of the Ge, Sb, Te shutters in each layer, is shown. SL periodicity is labeled on top of the figure. During the whole growth, the

Te shutter is open, since Te is the element present in both the binary alloys. As mentioned above, the growth starts by depositing Sb₂Te₃, as soon as the expected thickness of Sb₂Te₃ is deposited, the Sb shutter suddenly closes and the Ge one opens. The Ge shutter stays open for the estimated time needed to obtain the desired thickness of GeTe. In this way the SL periodicity is created (see fig. 3.16). The growth proceeds alternating opening and closure of Ge and Sb shutters, till the SL periodicity is repeated the desired numbers of time. With this in mind, it is clear that growing CSLs with different periodicity means changing the time of growth of each binary constituent. CSLs with 3 nm Sb₂Te₃/1 nm GeTe 3-1, 3-2, 3-3, 6-4 periodicity have been fabricated in this thesis work. In general the total thickness ranges between 20 and 80 nm, depending on the experimental techniques that will be employed on the sample. For optical experiments or XRD, a thicker sample is preferable.

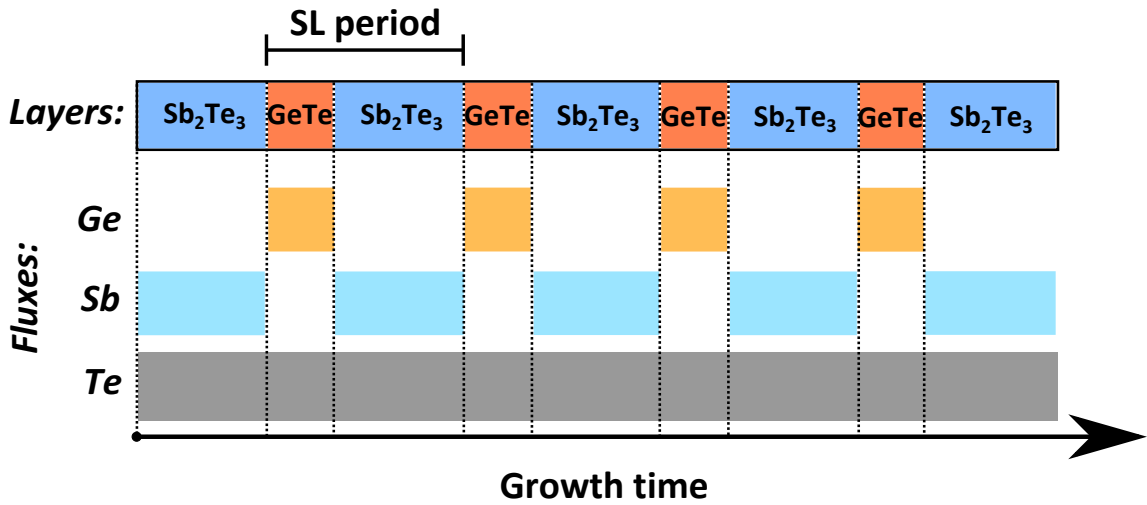


Figure 3.16: Schematic of a CSL growth process. Single elements are reported on horizontal lines. On the bottom, an axis indicates the growth time. Te shutter is open for all the growth duration (grey color), Ge and Sb alternate (yellow and light blue, respectively). The forming constituent layer, Sb₂Te₃ (blue) and GeTe (orange), are reported on top in correspondence of each opening and closure of the shutters. SL periodicity is labeled on top of the figure.

In fig. 3.17, symmetric ω -2 θ scans are shown for CSLs grown with different periodicities. We focus around the second order region of the whole XRD profiles. The red curve corresponds to the CSL with 3-1 periodicity, repeated 20 times, for a total thickness of 80 nm. The sharpest peak at $Q_z = 4.01 \text{ \AA}^{-1}$ is the Si(222). Next to it, there is a group of reflections (small black arrows), centered on a most intense peak at 3.65 \AA^{-1} . This is the superlattice peak [labeled CSL(222)], surrounded by its satellite peaks with a symmetrically distance (pSL) from the CSL(222) and related to the superlattice periodicity. For the specific sample, as expected, the calculated periodicity is $2\pi/\text{pSL} = 4 \text{ nm}$. Since the second order CSL(222) occurs exactly at twice the Q_z value of the first order CSL(111) (not shown), these are Bragg reflections. Its position is determined by the periodic distance between Te layers [p1 in fig. 3.17 b)] in the CSL, which can change depending on what is inserted in the other sublattice: Either Ge, Sb, or vdW gap. Therefore, we observe an average Te periodicity. The peak at $Q_z = 3.1 \text{ \AA}^{-1}$ has been assigned to the Sb₂Te₃. For reference, the Sb₂Te₃(00015) peak position is reported. It arises from the periodicity (p3) of 1 QL, or

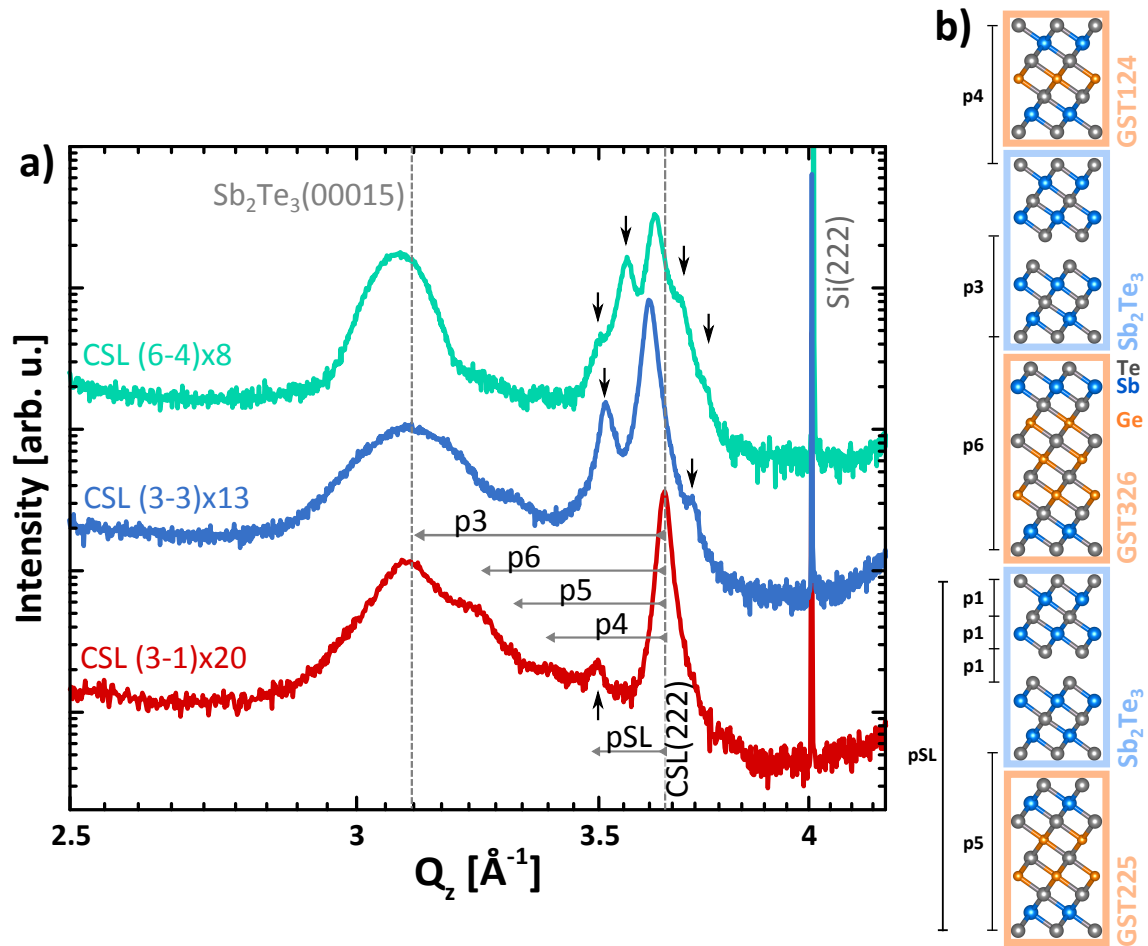


Figure 3.17: a) Symmetric ω - 2θ scans around second order reflections for CSLs grown with 3-1, 3-3 and 6-4 periodicities. $\text{Sb}_2\text{Te}_3(00015)$ reflection is reported as reference, and several periodicities in the scans are labeled and explained in the text; b) Simplified model structure of the obtained CSL (2 nm Sb_2Te_3 /2 nm GST). Te atoms are in gray, Sb in blue, and Ge in orange. p1 corresponds to the distance between two successive Te layers, p3, p4, p5, and p6 correlate to 3, 4, 5, and 6 time p1. Sb_2Te_3 and GST compounds are highlighted within blue and orange frames, respectively. Structure is taken from Wang *et al.* [53]

3.2 Fabrication of GeTe/Sb₂Te₃ Chalcogenide Superlattices

in other words from the periodicity of two vdW gaps in the Sb₂Te₃ [see fig. 3.17 b)]. If we now carefully look at the right shoulder of the peak, broad features can be identified. Those have been assigned to the presence of GST of different compositions in the CSL. In the specific, p6, p5 and p4 correspond to 6, 5 and 4 Te layer block size, i.e. to the different distance between vdW gaps in GST₃₂₆, GST₂₂₅ and GST₁₂₄, respectively. Such assignment is confirmed by the TEM investigation and EXAFS measurements conducted on our CSLs^[54,55] in which the intermixing of GeTe and Sb₂Te₃ into GST at the interfaces has been observed.

Similar considerations hold for each of the others XRD profile shown in fig. 3.17. Nevertheless, several clarifications need to be done. Concerning the CSLs satellite peaks, they clearly shift away from the main peak with decreasing thickness, matching the respective CSLs periodicity. As a consequence, more orders satellite peaks are distinguishable for the CSL 6-4 if compared to the 3-1. The position of the CSL(222) peak, which is an indication of the average composition of the superlattices, lays between the GeTe (222) peak (at 3.61 Å⁻¹, not shown) and Sb₂Te₃(00018) (at 3.72 Å⁻¹ not shown), and differs in the three curves. If we consider the Sb₂Te₃/GeTe ratio for the three CSL, i.e. 1, 1.5 and 3 for CSL (3-3), CSL (6-4) and CSL (3-1), respectively, the CSL(222) shifts consistently toward the Sb₂Te₃ peak direction, indicating that the CSLs are becoming more and more rich in Sb₂Te₃. Furthermore, GST reflections seem to become more intense as the sublayer thickness decreases, showing that intermixing is localized at the interfaces.

It is important to point out that sharp XRD features for these GST blocks cannot be expected because they are intercalated between Sb₂Te₃ blocks and never successively repeated, therefore, the envelope of their Fourier transform can only be very broad. This is also the reason why only one order of these superstructure peaks is observed; the lack of repetition of the GST blocks, coupled with the dispersion in the CSL periodicity due to temperature changes during growth, strongly suppress the higher order reflections.

3.3 Crystallization by Thermal Annealing of GeSbTe

Alloys

Effects of thermal crystallization on the structure of the GST alloy, have been already extensively studied^[107–109]. In general, the films are produced by sputtering techniques and grown on Si substrates covered by native SiO₂. The compound is deposited in the amorphous phase and subsequently switched to the crystalline phase by annealing it around the crystallization temperature^[107,108] leading to the formation of polycrystalline grains. On another end, in 2014 Bragaglia *et al.*^[103] demonstrated that both the metastable cubic and stable trigonal crystalline GST phases can be obtained by annealing an amorphous GST film deposited by MBE on a Si(111) substrate. As shown by the profiles of fig. 3.18, the substrate and the film share an out-of-plane epitaxial relationship: for the metastable phase [111] Si \parallel [111] GST and for the trigonal phase [111] Si \parallel [00.1] GST, respectively. In both cases then, the GST film presents a higher degree of texture in the out-of-plane direction if compared with the GST deposited by sputtering on SiO₂. Symmetric ω -2 θ scans of samples as deposited and annealed at different temperatures (T_A) are plotted with an offset for better comparison. In addition to the fact that both cubic and trigonal phases are obtained, it is important to underline how the ordering of vacancies takes place, appearing in the XRD profiles of metastable phase (135 °C) first, and gradually increasing in intensity and decreasing in FWHM for higher T_A [see VLp (00.21) development, as marked in blue in fig. 3.18].

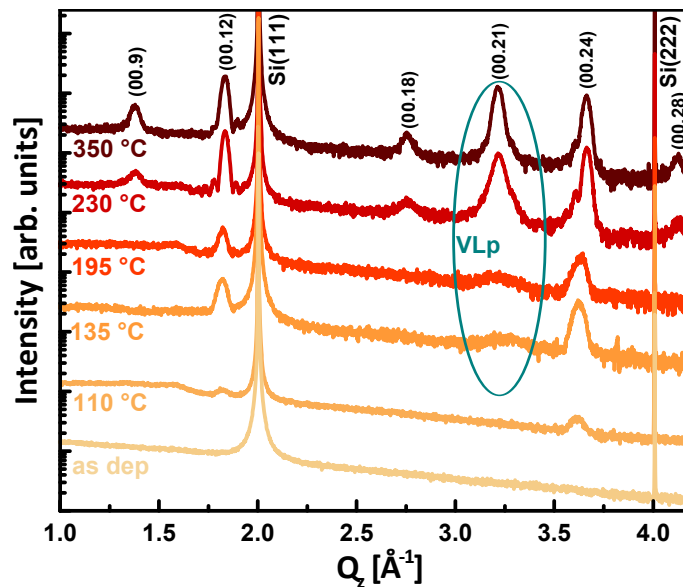


Figure 3.18: XRD profiles of GST/Si(111) as deposited by MBE and annealed at different T_A .

A further evidence of the ordering process has been given by HAADF STEM for a sample annealed at 170 °C for 1 h. In the micrograph of fig. 3.19 a), two sets of vacancy planes can clearly be identified: One is parallel to the substrate surface, the other is at an angle of 70 ° compared to the previous one. The VLs parallel to the substrate are oriented along the [111] direction and are measured by the ω -2 θ XRD scans, as shown in fig. 3.2 and fig. 3.18. The other set of VLs belong to

3.3 Crystallization by Thermal Annealing of GeSbTe Alloys

the equivalent $\{-111\}$ family of planes. In a STEM cross section we can only observe two of these equivalent planes even if for symmetry reasons vacancy layers should occur in all four directions. In fig. 3.19 b) a zoom on the vacancy planes at 70° in respect of the substrate surface is shown, and an integrated line profile is extracted in order to highlight the Te-Te layers distance across the gap. Distances of 3.4-3.5 Å indicate that the VLs are not fully depleted, therefore they are not vdW gaps as shown by the trigonal phase in fig. 3.9 a). Such result is in agreement with former literature^[16,110]. In addition, the stacking is that of the rocksalt phase (ABCABC), as shown regarding fig. 3.7. As opposed, the crystalline phase formed by annealing of a-GST at 110°C for 10 min does not show any VLP in the XRD profile (as shown in fig. 3.18), and STEM analysis confirms that the sample is in a disordered rocksalt phase with vacancies randomly distributed. Further details can be found in our dedicated publication^[110].

Note that these two specific samples are employed for the experiment in 4.1.1 where electrical and structural properties are directly compared.

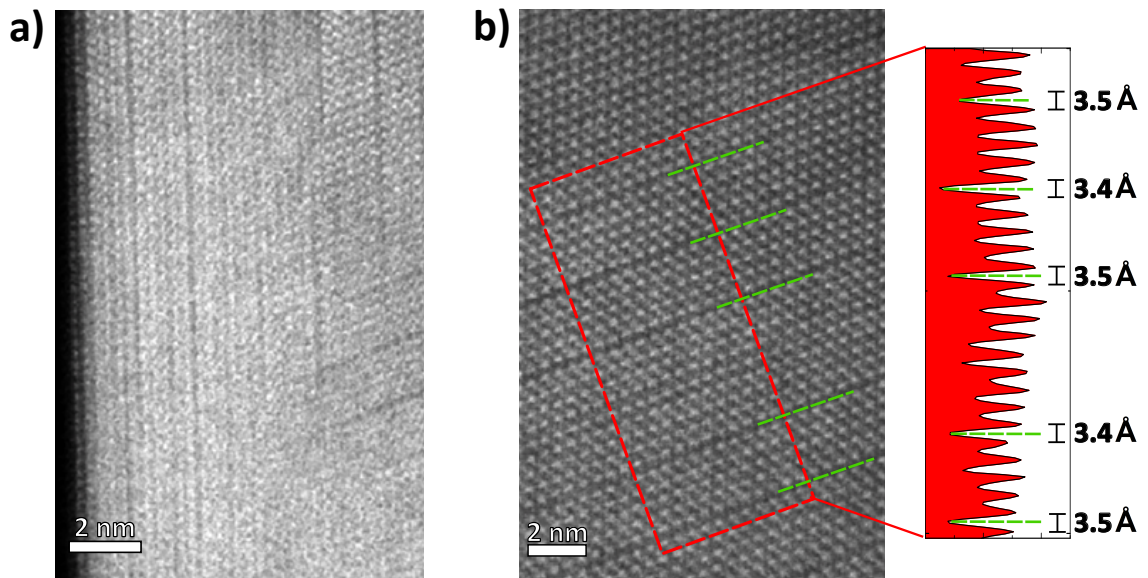


Figure 3.19: Cross-view [11.0] high resolution HAADF STEM micrograph of epitaxial (00.1) GST. Corresponding integrated line profile is highlighted (in red). Courtesy of Dr. A. M. Mio.

As largely discussed in section 3.1.1, periodicity of VL can be obtained from XRD profiles, i.e. out-of-plane lattice parameter c_0 , which is directly linked to the average composition of GST. In fig. 3.20 the behavior of c_0 from the cubic to the trigonal phase is shown. It is clearly visible that the sample composition slowly changes from average GST225 value towards the GST124. However, up to the complete crystallization at 130°C strain effects could not be completely ruled out, thus the estimation of the composition in the cubic phase is not precise, but it delivers the information that the first crystallites have a GST225 composition. The change of composition during annealing from a GST225 to GST124 is clearly visible in the graph and can be ascribed to the constituent elements segregation, singularly or in binaries alloys, as reported in former studies^[15,111].

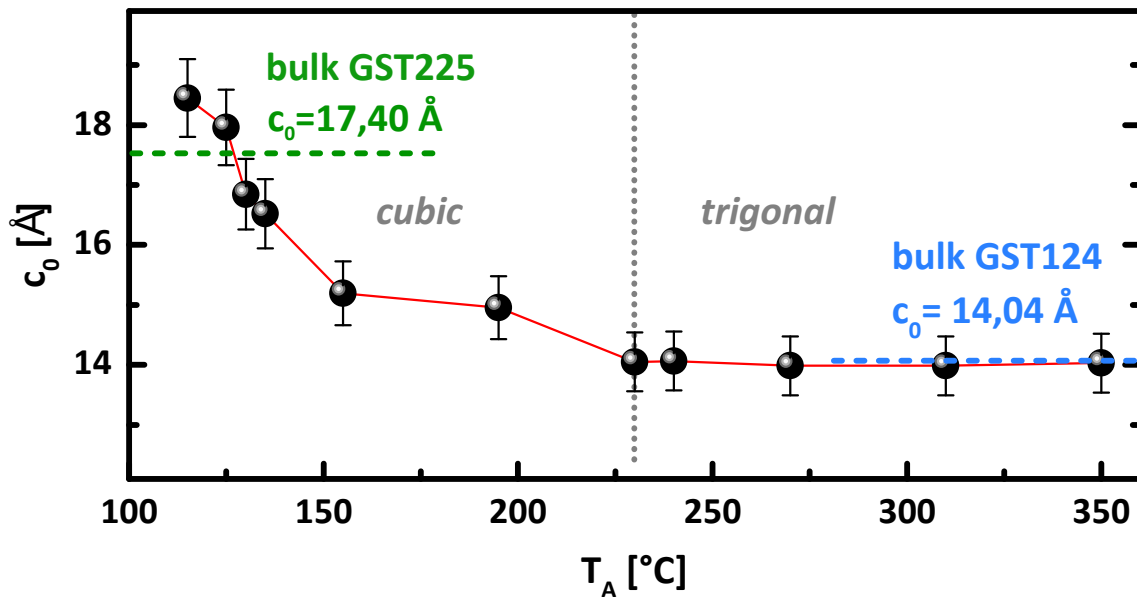


Figure 3.20: Lattice parameter c_0 evolution as function of T_A for crystallizing a-GST225. This is indication of compositional rearrangement upon annealing.

From the annealing experiment shown in fig. 3.18 and the study of Bragaglia *et al.*^[103], which systematically combines AFM, XRR and XRD measurements, it emerges that the preparation of the Si(111) substrate, acting as a template, plays a fundamental role on the crystallization of a-GST. Crystallization is prevalently of heterogeneous nature, starting at the Si/GST interface, with consequent formation of a propagating front. Homogeneous nucleation in the a-GST film could not be excluded within the investigations of the mentioned study, even if it is reasonably not dominant if compared to heterogeneous one.

In order to clearly address this point, a study on the effect of additional interfaces to the Si/GST was performed. Note that this experiment is of relevance in order to identify optimal samples to use in the temperature dependent spectroscopy and pump-probe experiments, as described in chapters 4 and 5. A crystallization experiment is performed on two pieces of the same c-GST sample grown by MBE. The starting composition is 326. The only difference between the two samples is that one is capped by Zn-SiO₂ and named "c-GST_capped", while the other is "c-GST_uncapped". In fig. 3.21 the XRD profiles are plotted with an offset for sake of clarity. The two metastable samples were annealed simultaneously at the same temperature for increasing T_A .

After each annealing, *ex situ* XRD was performed on both samples. In fig. 3.21 a) the profiles of "c-GST_uncapped" are shown. The c- to t-GST transition takes place at 265 °C, with a trigonal phase characterized by high structural quality according to the presence of many superior order peaks, with an increase in peak intensity and a decrease of its FWHM. On the contrary, for "c-GST_capped" [see fig. 3.21 b)] first the c- to t-GST transition temperature is around 370 °C, much higher than in the case of the not capped sample (100 °C difference); second, the crystalline quality of the t-GST is lower if compared to the case without capping, as can be seen by the asymmetric shape, low intensity and larger FWHM of the peak. For even higher $T_A = 405$ °C, the peaks become even more asymmetric, indication of possible segregation or more compositional disorder.

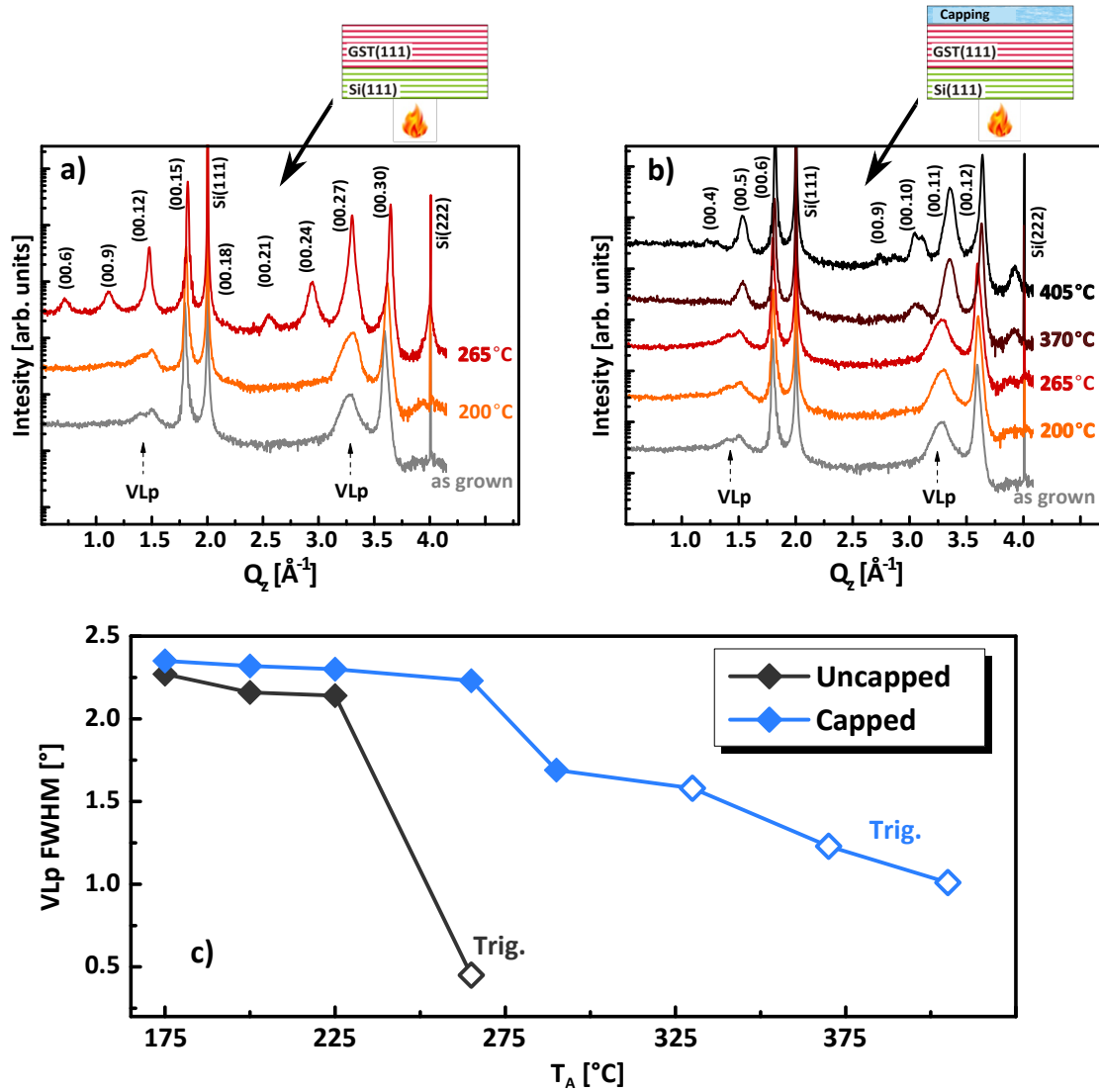


Figure 3.21: a) XRD profiles of "c-GST_uncapped" as grown and annealed at different T_A ; b) XRD profiles of "c-GST_capped" as grown and annealed at different T_A ; c) VLP FWHM evolution for capped (blue) and uncapped (black) samples. Filled symbols stay for c-GST, empty for t-GST phase.

To strengthen this last point, in fig. 3.21 c) the VLp FWHM evolution as a function of T_A is plotted for the uncapped (black) and capped (blue) samples. In particular the chosen peak for the analysis is the (00.27) for "c-GST_uncapped" and (00.11) for "c-GST_capped" (the zero order on the left of the main GST peak, if we consider the XRD profile in terms of a superlattice one). The FWHM of the VLp peak related to the uncapped sample shows a plateau till 225 °C with an abrupt decrease till a value of 0.45° for the trigonal phase. On the contrary, the capped sample shows a plateau till 265 °C and then starts gradually to decrease, indication of the fact that ordering is increasing in the sample, nevertheless the minimum value of 0.9° in the trigonal phase is higher than the previous case. This corroborate the assumption that in uncapped samples ordering is faster and in addition the sample spontaneously transforms into a higher quality trigonal phase if compared to the capped case. This result is in agreement with a recent STEM based study on our epitaxial samples, in which it is shown that by properly choosing the substrate and the capping layers, it is possible to promote or prevent the vacancies ordering in the rocksalt structure or the conversion into the trigonal phase^[110].

The study of periodicity evolution upon annealing is now discussed. In fig. 3.22, the average distance between Te-Te layers (d_{GST}) and the periodicity of the vacancy layers (Λ_{VL}), in other terms the size of the GST unit building blocks, are plotted as function of T_A . As expected, the periodicity decreases for increasing T_A ^[93]. Both capped and uncapped samples reach a minimum value around 3.45 Å.

If we look at the Λ_{VL} periodicity instead, interesting information is found. The uncapped sample shows a decrease of lattice periodicity with maximum change of 12 %, while instead the evolution of Λ_{VL} in case of the capped sample goes in the opposite direction, increasing consistently till a value of 22 Å, with a total percentage change of 8 % once the trigonal phase is obtained.

The capped sample presents less change in composition if compared to the uncapped, which drifts from an average GST326 into GST225 composition. According to our previous study, desorption really starts to play a role for T_A only above 300 °C^[103], which is not reached for the "c-GST_uncapped" sample. In addition, the fact that both samples present a percentage of compositional change, may indicate that segregation of the material might also plays an important role in order to lower the energy of the system in the trigonal phase.

Summarizing, higher structural quality in terms of texture and vacancy ordering is obtained for annealing without capping layer, thus all studies based on annealing experiments or crystallization performed by application of fs pulsed laser are conducted on uncapped samples (see chapter 4). Dynamic pump/probe experiments instead, are performed on samples with capping layer, in order to avoid oxidation upon strong laser pulses application.

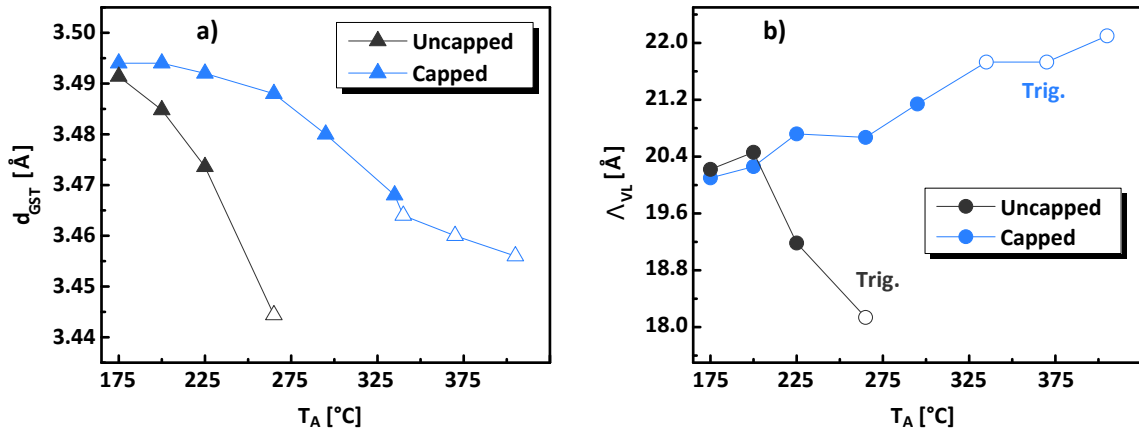


Figure 3.22: a) Periodicity d_{GST} of the Te-Te layers of Te sublattice for not capped (black triangle) and for capped (blue triangles) samples; b) Vacancy layer periodicity Δ_{VL} for not capped (black circles) and for capped (blue circles) samples. Filled symbols stay for c-GST, empty for t-GST phase.

3.4 Crystallization by Application of Femtosecond laser Pulses of GeSbTe Alloys

Thermal annealing is a slow process (min to hours timescale)^[103], while the switching in PCM devices occurs on a time scale of about 100 ns. In order to achieve faster crystallization, fs laser pulses have been employed. It is of fundamental importance then, to be aware of the structural properties (texturing and the ordering) of the crystalline phase obtained by laser irradiation. On another hand, also the control on the amorphization process has to be optimized in order to enable the pump-probe experiments where the reversible switching between the two phases is used to access the ultrafast dynamics in GST (see chapter 5)^[112,113].

The crystallization experiment of a-GST layers through laser irradiation was performed employing as a pump the pulsed laser described in chapter 2.1.1. In order to monitor *in situ* the change in reflectivity upon amorphous to crystalline phase transition, a He-Ne laser, is coupled with the pump, its signal is detected and sent to the oscilloscope (see schematic in fig 3.23). The thickness of the a-GST sample was chosen in such a way to match the penetration depth of the laser, so that the Si substrate can act as a template as demonstrated for the crystallization (see section 3.3)^[64,103] (fig 3.23). The fluence of 14 mJ/cm² resulted optimal in order to maximize the relative reflectivity change upon phase transition ($\sim 10\%$). Due to the X-ray beam detection size (1×10 mm²) of the diffractometer, a matrix of adjacent laser induced crystalline spots of 400 μ m in diameter was written on the a-GST. For each spot of the matrix, a sequence of fs pulses was delivered and the change of reflectivity as a function of time was monitored by an oscilloscope connected to the probe laser. Considering the pump repetition rate and the time it takes to reach the total relative reflectivity change (300 ms), it was estimated that the needed number of fs pulses for crystallization is ~ 300 . In addition, if we consider the time separation of 1 ms between two fs pulses, it is reasonable to assume that the crystallization process is faster than 300 ms with a lower limit of 45 ps.

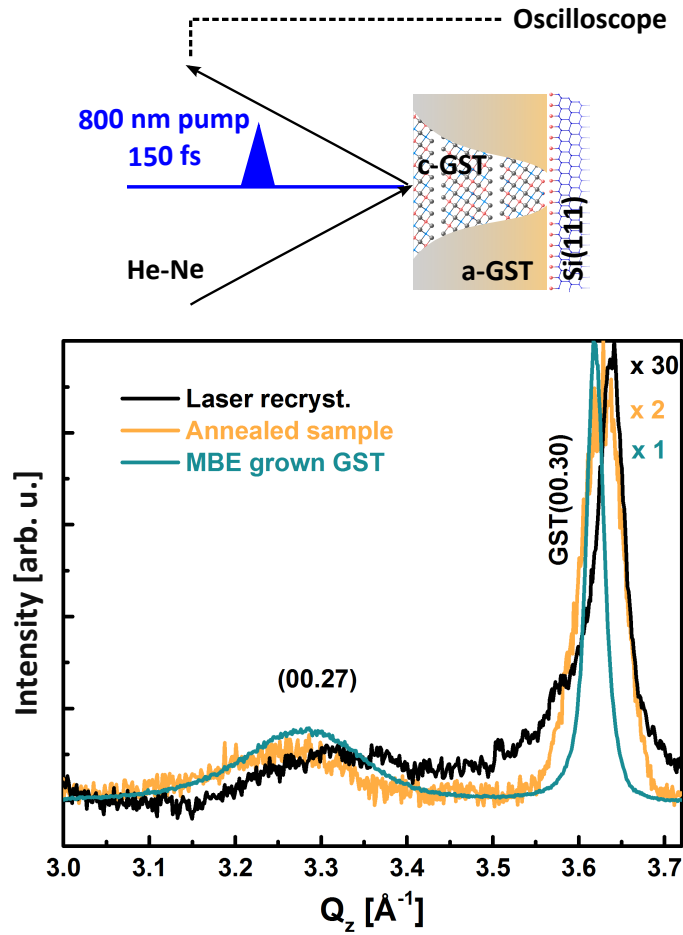


Figure 3.23: Superimposed ω - 2θ scans for crystalline GST on Si(111) grown by MBE (blue), a-GST crystallized by isothermal annealing (orange) and by fs laser pulses (black). All the curves are normalized to the GST peak and the multiplication factors are reported on the side. Schematic of the laser crystallization experiment is shown on top of the graph.

In fig. 3.23 a superimposition of XRD profiles for MBE grown (blue), annealed (orange) and laser crystallized GST (black curve) are shown. High texture and a faint vacancies ordering are obtained also in the case of a-GST crystallized by applying fs laser pulses. The tiny difference in GST (00.30) peak position after both recrystallization experiments is due to slight changes in composition. The samples were intentionally left uncapped to avoid strain and heterogeneous nucleation sites and thus a preferential desorption may occur, as shown in previous results^[103]. The overall lower intensity of the peaks in the laser annealed sample is attributed to a smaller percentage of crystallized volume, and to laser induced local damage of the film. Note that the crystallization into ordered crystalline phase may proceed via a two-step process, involving the initial formation of a disordered cubic phase and the subsequent ordering of the vacancies, as indicated by the ab initio molecular dynamics simulations of crystallization of GST in the presence of a two dimensional crystalline template^[114].

Another important advantage of working without capping layer consists in reducing the mechanical stress induced by the volume changes between the GST phases upon laser pumping in dynamic experiments. This aspect will be discussed in chapter 5.

3.5 Summary and Conclusions

In this chapter the three different fabrication methods to produce quasi-single-crystalline GST and CSLs grown by MBE have been presented, together with a deep structural characterization of the samples.

The first section has been dedicated to the growth by MBE of GST alloys and GeTe/Sb₂Te₃ chalcogenide superlattices. Structural characterization based on XRD simulations, DFT, and TEM microscopy, allowed to unequivocally assess the vacancy ordering in the GST samples, which was so far only predicted by theoretical calculations^[17,93]. The understanding of the ordering process enabled the realization of a fine tuning of the ordering degree, by changing growth parameters like Ge, Sb, Te fluxes and substrate temperature. Different growth windows have been explored by employing *in situ* RHEED and samples characterization by *ex situ* XRD and Raman spectroscopy. A phase diagram has been realized as output of the study. It has been demonstrated that the Te flux plays a fundamental role in the growth kinetic, determining the composition, crystalline phase and ordering in the GST. The three mentioned effects are not completely decoupled. Nevertheless by directly changing the Te flux, or indirectly if substrate temperature is modified, it has been possible to obtain different growth windows in which compositional tuning and different crystalline phases can be fabricated.

In the second section, a more simple fabrication method is presented and it is based on annealing of a-GST. Effect of multiple interfaces on the crystallization process has been investigated. Higher structural quality in terms of texture and ordering is obtained for annealing without capping layer. As a consequence, all studies requiring annealing experiments or crystallization by application of fs pulsed laser were performed without use of capping.

In the last section, in order to achieve faster crystallization, fs laser has been employed. It has been shown that also this techniques allows to crystallize a-GST into ordered x-GST. Crystallization process has been estimated to be faster than 300 ms with a lower limit of 45 ps.

As a general conclusion of the whole chapter, we have unequivocally demonstrated that vacancy ordering is achieved by MBE growth and by crystallization of an a-GST film deposited on a crystalline substrate by either thermal annealing or application of short laser pulses. This finding is remarkable as it demonstrates that it is possible to create an ordered crystalline GST layer using different fabrication procedures. One could ask which is the best technique to use, but the answer is not trivial. For these reasons, the three techniques are all necessary. MBE growth, although expensive, guarantees the highest control on composition, quality and ordering. Annealing of a-GST is a very simple and inexpensive technique, but requires a first step of MBE deposition of a-GST on a reconstructed and passivated Si surface. Furthermore, even if the x-GST obtained by laser crystallization results in a lower structural quality if compared to MBE grown and thermally annealed material, such technique is necessary for both optical applications and pump/probe based experiments (see chapters 2.1.1 and 5).

4 Metal-Insulator Transition Driven by Vacancy Ordering in GeSbTe Phase Change Materials

In order to study the correlation of the vacancy ordering with the MIT in GST (see chapter 1.2.2), it was of fundamental importance to be able to fabricate highly ordered quasi-single-crystalline material that facilitates the direct experimental observation of the vacancy layers. In addition, the possibility to fine tuning the disorder in the material with both MBE growth and thermal annealing (as discussed in chapter 3), might allows to control the MIT transition in GST alloys.

In the current chapter, employing global characterization methods such as XRD, Raman and FIR spectroscopy, phase and ordering degree of GST are assessed, and unequivocally correlated to the MIT.

In the first part of the chapter 4.1.1, the resistivity behavior of GST samples fabricated with different ordering degree is studied by low temperature electrical measurements and directly compared to their XRD profiles, allowing to identify the MIT.

In the second part 4.1.2, a combination of FIR and Raman spectroscopy is employed to investigate vibrational modes and carrier behavior in a- and x-GST phases, enabling to extract activation energies for the electron conduction of both c- and t- phases. Most importantly, by employing FIR spectroscopy to investigate the carrier evolution upon crystallization, a MIT is clearly determined corroborating the electrical studies.

4.1 *Correlation of Electrical and Structural Properties*

4.1.1 Electrical Characterization

In the previous chapter 3.1.1, it has been demonstrated how quasi-single-crystalline material allowed the direct observation of the VLs via XRD, as found by simulation of experimental XRD profiles through crystalmaker software. Direct observation of vacancy distribution by TEM characterization additionally corroborates the result^[94]. Most interestingly, the degree of ordering can be tuned in a controlled fashion depending on the sample fabrication, i.e. choice of growth

parameters in case of MBE growth, or choice of the annealing temperature, in case of fabrication by crystallization of a-GST. This last point is of relevance for the following experiment where the structural properties of the GST are directly compared to the electrical properties.

The ordering of vacancies into VLs and vdW gaps is expected to provide a reduction in the film resistivity^[16,26]. To this end, in fig. 4.1 the in-plane resistivity of different samples is compared as a function of temperature. a-GST annealed at 110 °C for 10 min (empty blue squares), which is crystalline but not yet ordered in term of vacancy planes, shows a negative temperature coefficient slope, indication of a non metallic behavior. Instead, the GST annealed at 170 °C for 1 h (filled blue squares), the as-grown highly-ordered GST studied in chapter 3.1.1 (filled orange squares) and the GST in trigonal phase obtained by annealing at 270 °C for 1 h (filled blue triangles), all show a positive temperature coefficient slope (metallic behaviour) with systematically decreasing resistivity. As given by the XRD intensity ratio (I_{VLp}/I_{GST}) between the VLp and the GST (00.30) peak, this indicates a progressive increase in vacancy ordering. I_{VLp}/I_{GST} ranges from zero for the disordered GST (empty blue squares) up to 1 for the t-GST (filled blue triangles). As already pointed out by Siegrist *et al.*^[26], the MIT in GST is not due to a c- to t- phase transition but, as proposed by Zhang *et al.*^[16], it relates to the ordering of localized vacancy clusters into layers. For comparison measurements taken from Siegrist *et al.*^[26] relative to polycrystalline c-GST (empty black squares) and t-GST (filled black triangles) are shown. It is evident that the resistivity values for poly-GST are systematically higher as compared to the highly ordered quasi-single-crystalline counterpart. In particular, as-grown highly-ordered GST shows resistivity value similar to the polycrystalline t-GST, displaying a metallic behavior with a low DC-resistivity value of $10^{-3} \Omega \text{ cm}$ and mobility value of $\mu = 12 \text{ cm}^2/\text{Vs}$ at RT. The range of resistivity by employing epitaxially grown GST is thus enlarged.

An important point concerns the role of grain size and the mechanisms characterizing the expected higher resistivity values at very low T for insulating samples. As discussed by Siegrist *et al.*^[26], the MIT results to be an intra-grain effect due to the small mean free path of electrons (not exceeding 21 Å). Both for poly-GST and for epitaxial samples the grain size largely exceeds the 21 Å. According to the same study, the most pronounced increase of the resistivity at low temperatures is ascribed to a hopping mechanism for conduction^[26]. Limited by the used setup (see chapter 2.2.3), samples with higher resistivity than the one annealed at 110 °C, or the amorphous sample (which presents resistance values in the range of MΩ) were not possible to be measured.

With the present study a direct link between ordering in GST and the MIT is definitely established and thus provides the experimental confirmation of theoretical prediction^[16]. In addition it was shown that the MIT is not due to a common phase transformation, i.e. a- to c-GST or c- to t-GST, but it occurs within the onset of non ordered cubic phase formation (annealed at 110 °C for 10 min) and slightly ordered one (annealed at 170 °C for 1 h and $I_{VLp}/I_{GST} = 0.01$).

STEM analysis by Dr. A. Mio of these samples corroborate the last result by showing that the sample annealed at 110 °C for 10 min is a disordered rocksalt phase, instead the one annealed at 170 °C for 1 h is rocksalt but with vacancy ordered into layers (see discussion about fig. 3.19 in chapter 3.3)^[110].

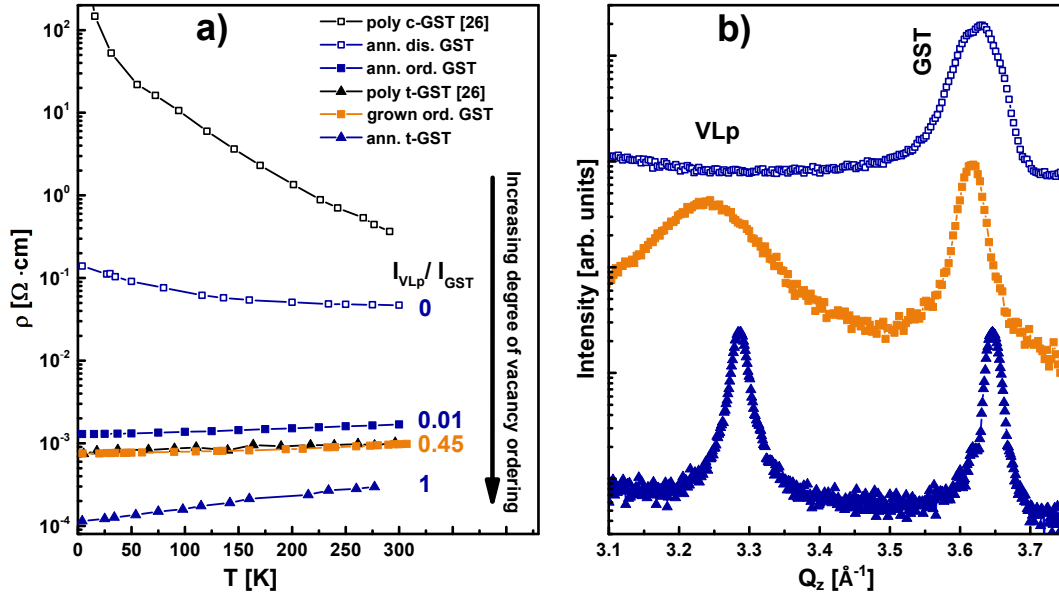


Figure 4.1: a) Resistivity as a function of temperature for quasi-single-crystalline GST samples (blue and orange) compared with poly-GST (black)^[26]. Empty and filled symbols denote disordered and ordered GST, while triangles t-GST. Intensity ratio ($I_{\text{VLP}}/I_{\text{GST}}$) of VLP and GST peak is reported for the epitaxial samples. b) $\omega/2\theta$ scans around the VLP and GST peak for different degrees of ordering. Reprints from^[94].

4.1.2 Far-Infrared and Raman Spectroscopy Investigation

The study of both the phase transition a- to x-GST and the disorder to order transition in GST is accompanied by changes in bonding as well as in crystal symmetry, which result perfectly suited to be investigated by Raman scattering as well as FIR spectroscopy. In addition, the included THz spectral range is particularly sensitive to conductivity changes depending on the phase. However, while Raman spectroscopy was often employed for such alloys^[115–119], the latter technique was mostly applied to Sb_2Te_3 ^[118], with the exception of dynamic experiments^[60]. In this section the combination of FIR and Raman spectroscopy is employed to investigate vibrational modes in amorphous and crystalline epitaxially grown as well as annealed GST samples. The observed phonon modes are assigned to the different crystalline phases by comparing temperature dependent FIR and Raman spectra. By FIR absorption we discriminate between the contributions of phonons and free carrier delocalization upon sample annealing for both amorphous to crystalline and insulating to metal transitions^[102].

In fig. 4.2 Raman spectra of a- and c-GST326 samples are presented in the spectral range from 30 cm^{-1} to 250 cm^{-1} . The a-GST spectrum is characterized by the Bose peak ($30\text{--}100 \text{ cm}^{-1}$)^[117], and two modes centered at 120 and 148 cm^{-1} assigned to vibrations of defective octahedra^[120]. The broad feature at 210 cm^{-1} is ascribed to vibrations of tetrahedra^[120]. In the c-GST spectrum two strong broad modes centered at 105 and 160 cm^{-1} are present. Polarization dependent measurements (not shown) combined to theoretical studies on our material systems^[120], help to assign the modes respectively to E_g (105 cm^{-1}) and A_{1g} (160 cm^{-1}).

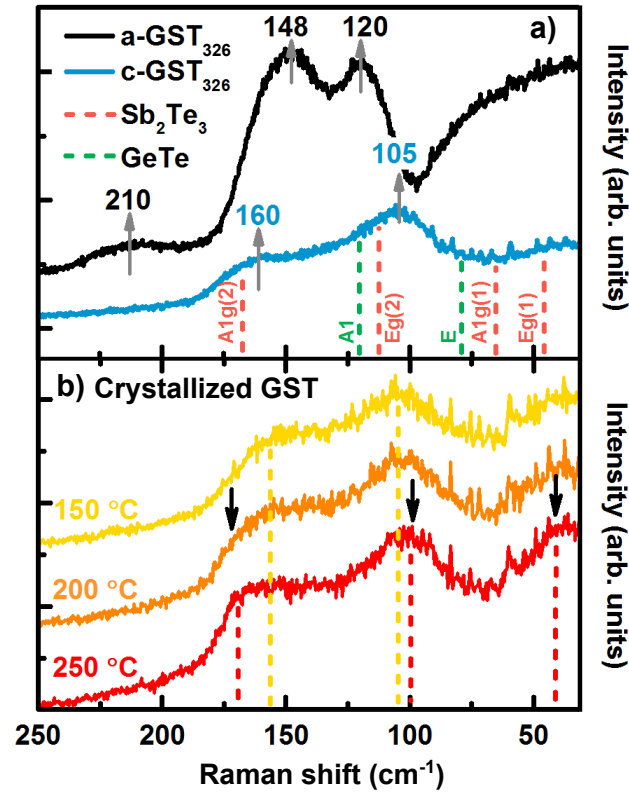


Figure 4.2: a) Comparison of Raman spectra for a-GST326 (black) and as grown c-GST326 (blue); Sb_2Te_3 (red) and GeTe (green) Raman mode positions are plotted as references. b) Raman spectra of crystallizing a-GST326 for three different temperatures. Modes of metastable c-GST326 are highlighted with yellow dashed lines. Upon increasing the temperature new modes appear, indication of the transition from c- to t-GST. At $T = 200^\circ\text{C}$ the characteristic mode of t-GST ($\sim 170\text{ cm}^{-1}$) appears (red dashed lines). In the red curve ($T = 200^\circ\text{C}$) the two arrows highlight the other two modes of the t-GST. Reprints from^[102].

Such modes are characteristic of the metastable cubic c-GST phase (point group $m\bar{3}m$ in accordance with previous studies^[120].

According to the $Fm\bar{3}m$ space group expected for metastable c-GST, and the sites occupancy given from Nonaka *et al.*^[37], no Raman active modes should be allowed, and only the T_{1u} (IR active mode, see later in the text) is expected. The fact that such vibrations (E_g and A_{1g}) are observed and are broad, is attributed to the presence of vacancies and defects that are responsible for the local symmetry breaking^[120]. The fluctuation of compositions^[94] and is intrinsic for certain GST compositions (see chapter 3.1.1). Due to the broad nature of c-GST vibrational modes, the treatment of such fluctuation is not obvious. Both binary compounds constituting GST are measured for reference purposes and the peak positions are displayed in fig. 4.2 with green (α -GeTe- $R\bar{3}m$ space group) and red (Sb_2Te_3 $R\bar{3}m$ space group) dotted lines. The Raman modes of the metastable c-GST326 [see fig. 4.2 a) blue curve] are prevalently arising from the Sb_2Te_3 modes $A_{1g}(2)$ and $E_g(2)$ slightly shifted (7 cm^{-1}) toward lower energies, while the modes of GeTe do not strongly contribute, due to their lower polarizability if compared to Sb_2Te_3 , as already reported in literature^[117,120] (see Table 4.1 for peak positions, mode assignments and their IR and Raman activities). In particular the mode at 160 cm^{-1} has a one-mode behavior (Sb_2Te_3 -like) while the mode at 105 cm^{-1} has a two modes behavior (Sb_2Te_3 -like and GeTe-like). The mode position shift of the c-GST326, compared to the binary constituents, is the indication of mode wavenumbers compositional dependence, similarly as for transition metal di-chalcogenides^[121].

In order to study the temperature dependence of the vibrational modes, annealing of a-GST326 was performed *in situ* during Raman data acquisition. A representative selection of the resulting spectra is plotted in fig. 4.2 b). At $T = 150\text{ }^\circ\text{C}$ (yellow curve) characteristic modes of the cubic phase (dotted yellow lines) compare well with those reported in fig. 4.2 a) for the as grown c-GST326. At $T = 250\text{ }^\circ\text{C}$ the film transforms into t-GST (red curve), for which two evident modes are identified^[122]: One at 170 cm^{-1} (A) and a second one at 100 cm^{-1} (E). A third faint mode at 45 cm^{-1} is also detected, nevertheless, the employed set up for the *in situ* annealing and the reduced thickness of the sample (30 nm), make the attribution of peaks in the low frequency range not trivial. We tentatively assign it to an A mode^[122].

The mode at 170 cm^{-1} starts to be visible in the spectra at $T = 200\text{ }^\circ\text{C}$ (see arrow on the orange curve), and is associated to vacancies ordering into layers which breaks locally the cubic symmetry, and will transform into vdW gaps once the t-GST is achieved (red curve)^[110]. The progressive creation of ordered vacancy layers obscures the unequivocal assignment of a specific space group within the transition region. As reported in our previous studies^[103], it is not possible to exclude compositional rearrangement in the stable phase (see chapter 3.3).

Fig. 4.3 a) shows the FIR absorbance of MBE grown a-GST326 (black curve) and c-GST326 (blue curve) [Absorbance = $-\text{Log}(T_{\text{GST}}/T_{\text{Si}})$ where T_{GST} and T_{Si} are the GST and Si transmitted intensities]. Within the resolution of the measurement, no absorption in the whole spectral range is measured for a-GST326, in line with the absence of free carriers and low mobility in the amorphous phase, and due to a random distribution of local dipoles. On the contrary, c-GST326 shows a strong absorption on the whole spectral range, which is an indication of metallic behavior with high free carrier concentration ($\sim 10^{20}\text{ cm}^{-3}$) and a broad (FWHM $\sim 40\text{ cm}^{-1}$) absorption fea-

	Mode	(cm ⁻¹)	IR	Raman
a-GST	A1	120	no	yes
	A1	148	no	yes
		210	no	yes
c-GST	T _{1u}	70	yes	no
	E _g	105	no	yes
		120	yes	no
	A _{1g}	160	no	yes
t-GST	A-type	45	no	yes
	E-type	100	yes	yes
	A-type	170	no	yes
Sb ₂ Te ₃	E _g (1)	48	no	yes
	A _u (1)	62	yes	no
	A _{1g} (1)	67	no	yes
	E _g (2)	113	no	yes
	A _{1g} (2)	165	no	yes
GeTe	E	79	yes	yes
	A1	119	yes	yes

Table 4.1: Vibrational mode assignment and position for a-GST326, c-GST (both 225 and 326), t-GST, Sb₂Te₃ and GeTe. IR and Raman activity are specified. Note that the position of T_{1u} for c-GST is reported as the convolution of the two peaks at 60 cm⁻¹ (GST225) and 80 cm⁻¹ (GST326), according to fig. 4.3. See text for details.

ture around 70 cm^{-1} . In a-GST carriers are localized^[3,62,94] while in c-GST delocalized electrons allow for the conduction^[16,26]. For c-GST the spectral range can be divided into two main regions: the phonon dominated region between 30 and 150 cm^{-1} , that is assumed to be sensitive to the lattice transformations upon phase transitions, and the free carrier dominated region above 150 cm^{-1} . Fig. 4.3 b) shows a dedicated measurement with high resolution around the phonon related absorption feature for MBE grown c-GST326 (blue), GeTe (green) and Sb_2Te_3 (red). Sb_2Te_3 displays a peak at 62 cm^{-1} , which corresponds to the A_{1u} mode for the symmetry $R\bar{3}m$, while α -GeTe presents two peaks at 79 cm^{-1} and 119 cm^{-1} (grey dashed line in the plot), attributed to the E and A_{1u} modes, respectively (see also Raman spectrum). In the case of c-GST326, the IR phonon mode centered at $\sim 70 \text{ cm}^{-1}$, according to the $m\bar{3}m$ point group of the cubic symmetry, is attributed to a T_{1u} . However, as already mentioned, vacancies, defects and distortion of bonds could break the inversion symmetry predicted by the space group, leading to a mixed nature of the phonon modes^[123]. The broad mode T_{1u} of c-GST is composed by the superposition of the phonon modes of the binary constituent compounds, E and A_{1u} for GeTe and Sb_2Te_3 , respectively, [see fig. 4.3 c) and d)] since it is possible to best fit the peak with two Lorentzian functions centered at the experimental positions of the GeTe and Sb_2Te_3 modes, indicating a two-modes type behavior (Sb_2Te_3 and GeTe-like). As opposed to Raman spectroscopy, the two binary component modes show no wavenumber dependency on GST composition. The latter is accounted only in the relative intensities of the two modes. In particular, the main contribution for c-GST326 is the E mode of GeTe [see fig. 4.3 c)], where more Ge-Te than Sb-Te bonds are expected. Instead, for the c-GST225 case [see fig. 4.3 d)] a slightly higher intensity of the Sb_2Te_3 component is visible. FIR spectroscopy thus helps in the quantification of compositional changes.

Crystallization by annealing of a-GST326 was also studied by *in situ* temperature dependent FIR spectroscopy (see chapter 2.3.1). The phonon dominated region is shown in fig. 4.4 a) where the absorption [Absorption = $1 - (T_{\text{GST}} - T_{\text{Si}})/T_0$, with T_0 the incident intensity] increases with the annealing temperature from a value close to zero till a maximum value of 14 %. Please note that at high resolution, a faint mode at 80 cm^{-1} is visible in a-GST326, indicative of the presence of short range ordering. In addition, starting at 206°C the main peak at 80 cm^{-1} (P1, see grey dotted line) attributed to c-GST326 decreases while a new mode at $\sim 100 \text{ cm}^{-1}$ ascribed to t-GST emerges [P2 black arrow and grey dotted line in fig. 4.4 a)]. P2 becomes more evident at higher annealing temperature [red curve in fig. 4.4 a)] when the film is completely trigonal ($T > 225^\circ\text{C}$), in accordance with Raman spectra in fig. 4.2 b). As-grown c-GST326 as well as a-GST326 crystallized at low annealing temperatures [$T = 150^\circ\text{C}$ in fig. 4.2 b)] belong to the $m\bar{3}m$ point group with the exclusion (IR vs. Raman) selection rule preserved. Once the cubic to trigonal phase transition takes place, if we exclude a transition region where both modes characteristic of the two phases (P1 at 80 cm^{-1} for the cubic and P2 at 100 cm^{-1} for the trigonal) coexist and the symmetry determination is not possible, the exclusion selection rule seems not to hold and the mode at 100 cm^{-1} appears in both Raman [see fig. 4.2 b)] and IR spectra (clearly evident in the completely t-GST annealed at 250°C). According to literature, symmetry change between the two phases takes place from the $m\bar{3}m$ to the expected $\bar{3}m$ point group, with t-GST belonging to the space group $R\bar{3}m$ or $P\bar{3}m1$ depending on the composition^[1], for which mutual exclusion selection

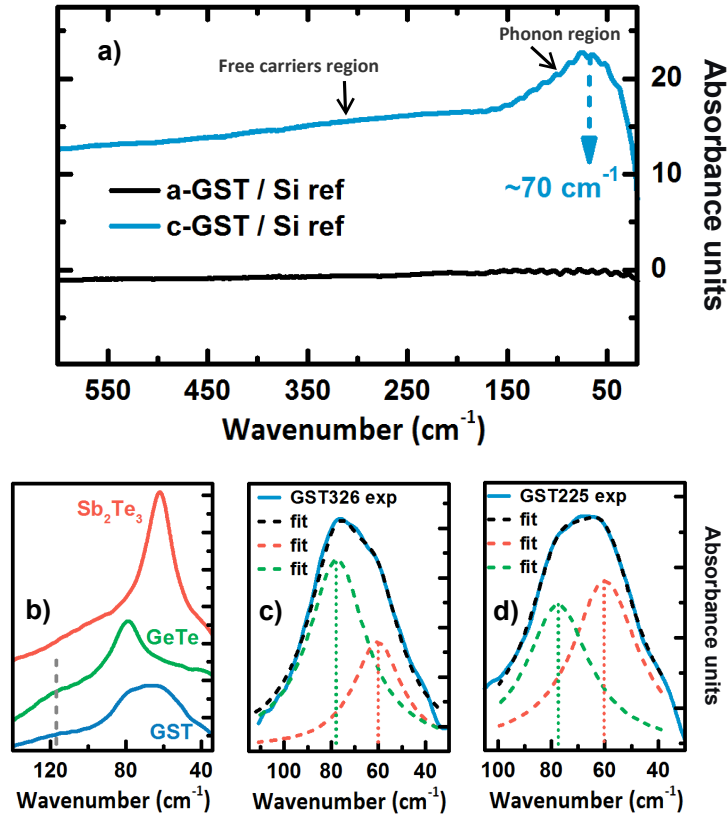


Figure 4.3: a) FIR absorbance spectra for a-GST326 and c-GST326 (black and blue curves, respectively). The spectra are normalized to the Si substrate. b) Zoom around absorption feature of GST225 (30 to 140 cm^{-1}) (blue), with Sb_2Te_3 (red) and GeTe (green) spectra as references. c) Fit of the GST326 experimental curve using two Lorentzian peaks centered at the position of the Sb_2Te_3 (red) and GeTe (blue) modes. d) Fit of GST225 for comparison. Reprints from^[102].

rules are valid. However, in Sosso *et al.*^[122] the effect of mixed Ge/Sb layers is shown to induce a partial break of the symmetry, from $P\bar{3}m1$ to a lower symmetry state, where the Pm symmetry is preserved, allowing the double character (both Raman and IR) of the modes.

Several Arrhenius plots are extracted from the absorption spectra and plotted as a function of $1/k_B T$ in fig. 4.4 b) and c). The contribution arising from phonons is shown by circles [see fig. 4.4 a)], blue for P1 (c-GST326) and red for P2 (t-GST). Four main regions can be identified: White for a-GST, blue for the transition region from a-GST to c-GST, orange for the transition from c- to t-GST and red for t-GST. The annealing temperature ranges are in agreement with our previous XRD studies^[94,103] (see chapter 3.3). Please note that a full disordered c-GST326 is obtained at 130 °C^[103] and it is ordered at about 183 °C^[94], while t-GST is present already at 225 °C. From the slope of the curves in the linear blue region an activation energy for the conduction of c-GST326 is extracted, this giving $E_A = 0.43$ eV, a value which compares well with literature^[124,125]. In the red region (t-GST) the slope of P2 has an activation energy of $E_A = 0.08$ eV, indication of an enhanced metallic behavior. Additional information can be obtained if we consider the difference [triangles in fig. 4.4 b)] between the absorption of phonons (P1 and P2) and free carriers [at 330 cm^{-1} , see fig. 4.3 a)]. For temperatures lower than 183 °C the P1 phonon evolution, indication of a-GST326 to c-GST326 phase transformation, is dominant, as the two curves (circles and triangles) display the same shape.

Above 220 °C, the free carriers are screening the P2 phonon, suggesting longitudinal nature for P2 in the trigonal phase. In the transition region between c- and t-GST the progressive ordering of vacancies into layers, till the formation of van der Waals gaps, leads to free carrier delocalization and metallic behavior with an activation energy $E_A = 0.07$ eV (orange line). In fig. 4.4 c) we display the Arrhenius plot of the reflectivity at 330 cm^{-1} . Although the absolute values could be unreliable as the measured sample is very thin (30 nm), we clearly see that the reflectivity increases continuously during annealing induced transition from c-GST to t-GST, indication of the enhanced metallic behavior of the sample. The reflectivity increases significantly only at about $T = 176$ °C that is identified as the temperature for the MIT to occur, as it corresponds to the sudden increase in conduction^[94]. Above $T = 183$ °C a second trend can be identified, and is ascribed to the cubic to trigonal phase transition that proceeds gradually. Furthermore, the increase of reflectivity above 220 °C reflects the increase of free carrier delocalization and confirms their dominant role in screening the phonon.

In summary, within this section the symmetries to the crystalline phases of GST326 by comparing FIR and Raman temperature dependent spectra were assigned. Ordered c-GST is ascribed to the $Fm\bar{3}m$ space group, while as for t-GST the inversion selection rules do not hold, a partial symmetry breaking due to Ge/Sb mixed anion layers^[122] occurs. It was also demonstrated that FIR spectroscopy is sensitive to composition difference in as grown crystalline GST samples and helps in quantification of conduction enhancement/carrier behavior upon phase transitions. Furthermore, by studying the FIR absorption evolution upon annealing, the contributions of phonons, and free carrier delocalization for the conduction of c-GST326 and t-GST, as well as for the transition regions a-GST326 to c-GST326 and c- to t-GST is discriminated. In addition, from the reflec-

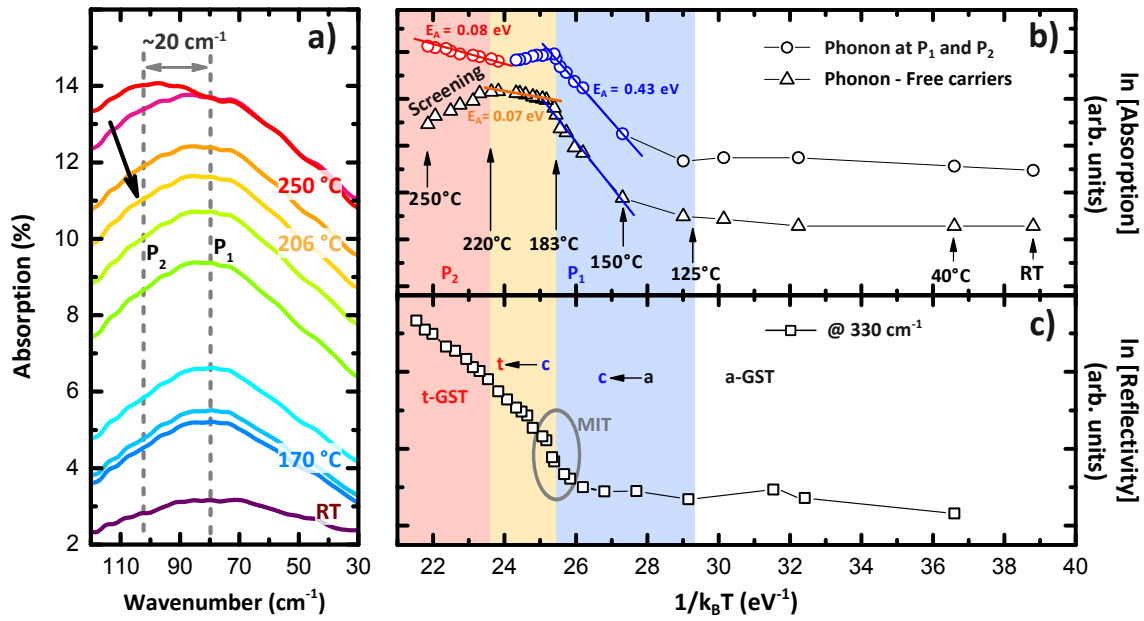


Figure 4.4: a) Temperature dependent absorption spectra of crystallizing a-GST326 around the main absorption feature. b) Arrhenius plot based on the intensity evolution of the phonon dominated region: peak P_1 for c-GST326 and P_2 for t-GST (empty circles), and difference between phonon and carrier dominated region (at 330 cm^{-1}) intensities evolution (empty triangles). Activation energy of the conduction process (blue for cubic- and red for t-GST) are obtained after fitting. c) Arrhenius plot of the evolution of the reflectivity at 330 cm^{-1} . Four main regions are visible in b) and c): white for a-GST326, blue for c-GST326, orange for the transition from c- to t-GST and red for t-GST. Reprints from^[102].

tivity change the MIT is clearly identified and occurs at the onset between disordered to ordered cubic phase, in line with the results shown in the previous section and contained in our published work.^[94]

4.2 Summary and Conclusions

In conclusion, within the context of phase transition and metal-insulator transition in GST, light was shed on several aspects^[94,102], which were till now only theoretically predicted^[16] or not fully understood^[26]. Phase and ordering degree of the GST were assessed, and it was unequivocally demonstrated that MIT is driven by vacancy ordering in GST. In particular, first by comparing electrical measurement to XRD, the transition from insulating to metallic behavior is obtained as soon as vacancies start to order, still within the cubic phase, evolving from a c- disordered to a c- ordered GST. In the second part of the study, a combination of FIR and Raman spectroscopy was employed to investigate vibrational modes and the carrier behavior in amorphous and crystalline phases, enabling to extract activation energies of for the electron conduction for both c- and t-GST phases. Most important within both investigations, a MIT is clearly identified to occur at the onset of the transition between the disordered and the ordered cubic phase, demonstrating the consistence of the results.

5 Time-Resolved Studies of Laser-Driven Dynamics

GeTe/Sb₂Te₃ based CSLs resemble in their structure that of ordered GST due to the presence of periodic vdW gaps in between building blocks alternating Te, Sb and Ge layers. For this reason it is surprising that the switching mechanism of GST and CSLs is so different (see chapter 1.3).

Driven by the necessity to understand the mechanism at the base of CSL switching, investigations of ultrafast dynamics in GST alloys and CSLs have been performed by employing two different approaches: Time-resolved X-ray absorption and THz spectroscopy under fs-pulsed laser excitation.

The first section 5.1 of the chapter deals with the XAS attempt for dynamic investigations of GST alloys. The goals of the study, together with the experimental methodology used, will be discussed. The second section 5.2, instead, is dedicated to the investigation performed by time-resolved THz spectroscopy. Comparison between ordered c-GST and CSLs dynamics will be discussed.

5.1 X-Ray Absorption Spectroscopy for Dynamic Investigations of GeSbTe Alloys

As introduced in chapter 1.4, in a previous study of our group on the 100 ps timescale^[64,126], the structural properties of as-grown epitaxial and fs laser-switched single-crystalline samples have been investigated at the ESRF ID9B beamline. Using pump (fs-laser irradiation)/X-ray probe technique it has been clearly shown that the low ps to fs time regime is of interest for the structural response of GST. Mainly, due to the lack of X-ray probes of sufficient time resolution, the sub-ps dynamics of the switching processes has been uncharted territory for long time. In recent years, Krbal *et al.*^[127] have shown that there is a contrast between the XAS at the Ge L3 edge of a- and x-PCM. They have attributed this contrast difference to a change in the structural environment of Ge during switching. We decided to use such a contrast to study the dynamics of the switching process, performing pump/probe study with an X-ray pulse length in the fs range, as supplied by the Femtoslicing-beamline at BESSY II (see chapter 2.3.3 for details).

To allow for XAS measurement using a transmission geometry, x-GeTe and c-GST thin films with a thickness of ~ 30 nm were grown on $5\ \mu\text{m}$ thick Si(111) membranes (Norcada Inc.) using MBE. Growth parameters can be found elsewhere^[112]. The samples were capped with 7 nm Si_xN_y by *in situ* radio-frequency magnetron sputtering.

The Static XAS Signal Determination

At first static XAS measurements of x-GeTe were performed. Subsequently crystalline spots were amorphized by exposure to multiple fs-laser pulses with a fluence of $50\ \text{mJ}/\text{cm}^2$. The amorphization of the crystalline spots resulted in a change in optical contrast that could be observed by eye using a CCD camera mounted for inspection of the sample. In fig. 5.1 a), the normalized XAS spectra of x- and a-GeTe are compared. It can be seen that a-GeTe has a slightly lower X-ray absorption for X-rays with energies between 1220 and 1240 eV, and a shoulder below the L3 edge. This spectral feature is not present in the spectrum of x-GeTe. Therefore, we conclude that the difference in XAS contrast between 1225 and 1230 eV can be used to identify x- and a-GeTe, in agreement with Krbal *et al.*^[127].

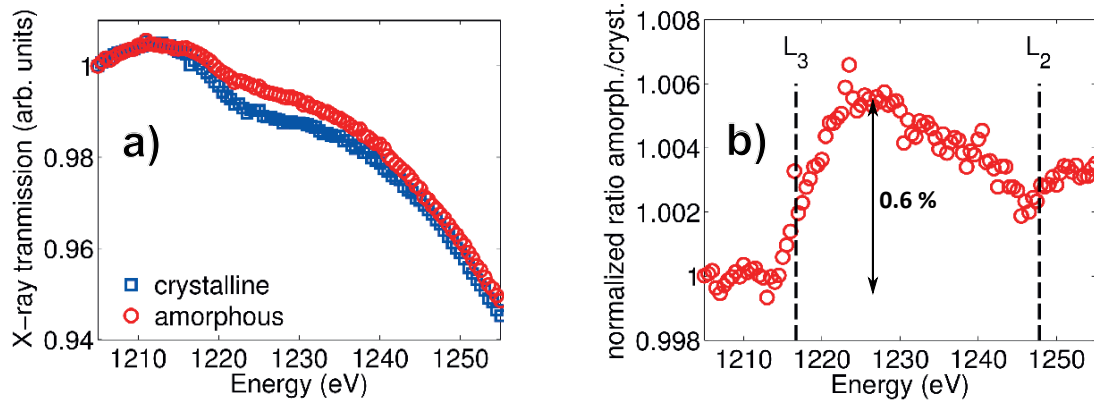


Figure 5.1: a) normalized X-ray transmission as a function of X-ray energy for x- (blue squares) and a-GeTe (red circles). b) normalized ratio between the amorphous and crystalline spectra. L2 and L3 Ge edges are reported. Reprints from^[112].

For the pump/probe measurements, it is necessary to determine the largest difference between the crystalline and amorphous spectra. Therefore, the ratio between the two spectra, which is calculated and plotted in fig. 5.1 b). It can be seen that the largest difference, occurs between 1225 and 1230 eV and amounts to 0.6 %. It should be noted that we decided to work in the sub-threshold regime: The laser fluence is large enough to induce a dynamical change in the material and on the other hand is small enough to prevent irreversible amorphization. This last point is not trivial, in fact if a permanent sample change is induced (i.e. amorphization from a crystalline sample), a reversible switching has to be cyclically performed on the timescale of the probing X-rays, which is experimentally difficult to realize. Therefore it is more convenient to first start from

dynamic changes in sub-threshold considered as precursors of amorphization and crystallization. In these conditions, the percentage of a dynamic effect is even smaller than the static one, making the detection of ultrafast dynamics quite challenging.

Time-Resolved Study in Sub-Threshold Regime

We determined the laser fluence at which dynamical changes occur. Preliminary fluence dependency study was already performed in the laboratory in order to identify fluence values that induce amorphization and crystallization in GST and GeTe grown on conventional Si(111) substrates and membranes (which present different values due to a change in the temperature dissipation within the substrate). However, due to the change of the set up (from the laboratory to the beam line), a fine *in situ* recalibration of the needed fluences for the time-resolved experiment has been performed. Fig. 5.2 shows the dependence of the ratio between the pumped and the unpumped signal as a function of the laser fluence applied on a crystalline part of the sample. Measurements were taken at a constant delay time between the laser pump and X-ray probe pulses of 1225 eV in order to probe the sample after the excitation of the laser pump. It can be seen that this ratio increases above 22 mJ/cm². This change in the ratio between the X-ray transmission of the pumped and unpumped sample is taken as an indication of a change in properties of the sample. Such a change can be dynamical and thus due to an excitation of the material or static and due to amorphization. Furthermore, a decrease in the ratio can be observed around 36 mJ/cm², probably due to ablation, as confirmed by the bleaching on the sample observable by eyes. Based on these considerations and assuming that the measured change in the pump/unpump ratio in fig. 5.2 is due to a dynamical effect, a pump/probe experiment on a single spot was performed at a laser fluence of 28 mJ/cm².

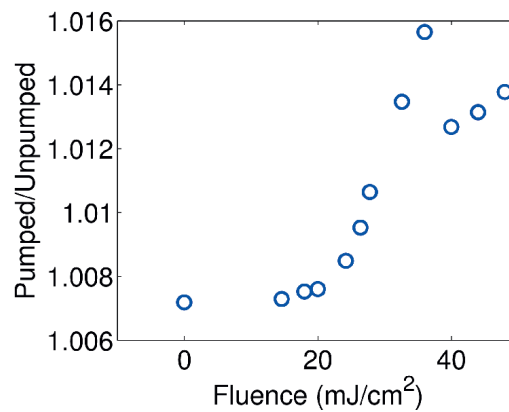


Figure 5.2: The ratio between the pumped and unpumped transmission signal as a function of laser fluence on x-GeTe. Reprints from^[112]

Fig. 5.3 a) shows the dynamic measurement in terms of ratio between the pumped and unpumped signals as a function of delay. The first 20 measurements are averaged. Time zero (τ_0) has been previously measured and is at 800 ps. No dynamic response can be resolved. In

order to study whether the sample is affected by the irradiation with fs laser pulses, the average pump/unpump ratio over the measured range of delays is calculated and plotted for each successive measurement in fig. 5.3 b). It can be seen that the averaged ratio increases (initially stepwise) with the increase in measurement time. The measurement of 20 scans took approximately 70 min. This implies that around 12 million pulses were applied on the crystalline sample during these measurements, which resulted in change in optical contrast as observed by eye. Furthermore, a similar increase is observed when the laser fluence was reduced to 8 mJ/cm^2 (red squares). The increase of the averaged ratio between pumped and unpumped both with laser fluence and with the number of applied pulses, is interpreted as a sign of gradual amorphization of the crystalline phase, which was not reversibly switched back within this experiment. Therefore dynamics detection has not been successful.

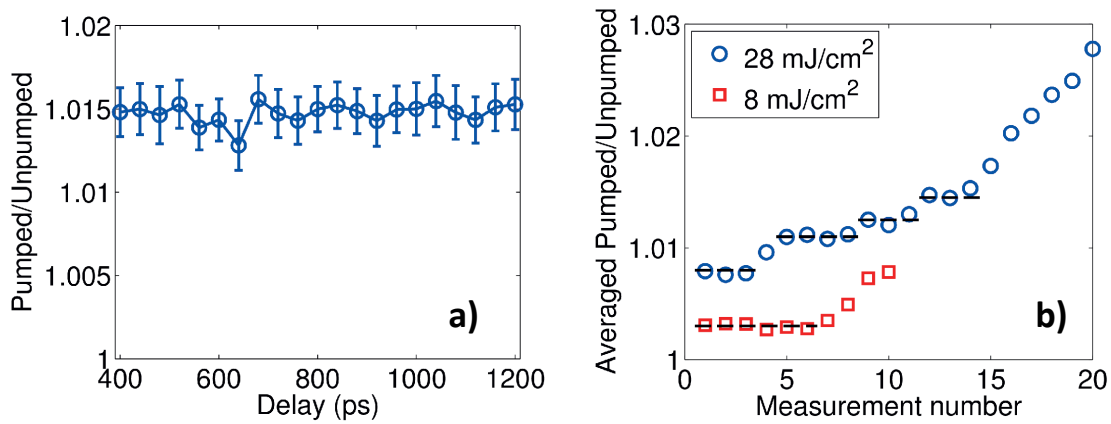


Figure 5.3: a) The ratio between the pumped and unpumped transmission signal as a function of delay time for 20 delay scans using a laser fluence of 28 mJ/cm^2 . τ_0 is at 800 ps. b) The ratio between the pumped and unpumped transmission signal as a function of the number of delay scans using laser fluence of 28 mJ/cm^2 (blue circles) and 8 mJ/cm^2 (red squares). The dashed lines are guides to the eye. Reprints from^[112]

Time-Resolved Study Inducing Reversible Switching

The main problems found in the aforementioned experiment, consisted in the difficulty to remain in a sub-threshold regime during the pumped and unpumped signal acquisition; in sub-threshold regime long integration times were required for a good signal to noise detection (low static signal contrast). Thus, permanent amorphization induced by exposition to the pumping laser could not be avoided. This implied the absence of reversible cycling between the two states.

As shown in chapter 3.4, epitaxial GST films maintain their crystalline orientation during an amorphization-recrystallization cycle using fs-laser irradiation. This is also found in a previous work on our epitaxial material^[64]. Furthermore, it is known that sub-nanosecond recrystallization can occur in device structures^[12] and that it occurs in μs at temperatures around 250°C ^[128]. This implies that if, while we cycle between the amorphous and crystalline phase we heat the

sample, we can recrystallize the amorphous within μs . Such approach could make it possible to overcome the problem of not reversible amorphization due to long time laser exposure. In addition, it could in principle improve the signal-to-noise ratio, since it is no longer necessary to use sub-threshold regime.

Therefore, prior to the laser pump/X-ray probe experiment, accurate amorphization-recrystallization tests have been performed employing a pump/probe scheme. A He-Ne (probe) and a 800 nm (pump) beams are sent on the sample and detected with a photodiode connected to the oscilloscope [see fig. 5.4 a)]. This configuration allows for reflectivity monitoring of the sample upon pumping (as described in chapter 3.4). *In situ* annealing of the sample induces recrystallization of the amorphized sample. The challenge is to find the optimal amorphization power combined to an annealing temperature which ensures recrystallization speed fast enough to be matched to the laser pump/X-ray probe experiment at the beam line. Note that the limitation is given by the pump repetition of $\sim 333 \mu\text{s}$ (3 kHz). This could be achieved by employing a temperature of 190 °C which allows recrystallization within 250 μs , sufficient for the X-ray pulse to probe the amorphized and recrystallized spot on the sample and then start again with the same cycle for the duration of the whole XAS measurement. In fig. 5.4 b) an example of the reflectivity change upon laser amorphization and recrystallization due to annealing at 190 °C is shown. Therefore, time-resolved XAS measurements on GST films were performed at this temperature.

This approach has been employed during a dedicated beamtime, however no time-resolved change in the XAS signal was observed. The signal-to-noise ratio did not show a significant increase, requiring long integration times as in the previous approach in sub-threshold regime. During the measurement, the long time exposure at a repetition rate of 3 kHz caused bleaching of the sample (as clearly observable by CCD camera) due to cap layer deterioration, compromising the switching effect of the GST layer.

5.1.1 Determination of the Experimental Limits

No time dependent change in the electronic structure was observed either working in sub-threshold regime or by inducing reversible switching in the material which expected to improve reproducibility and signal-to-noise ratio. Impact of pump effects at the Ge L3 edge seems to be extremely small or occurs only on a very short timescale $< 100 \text{ fs}$.

These results suggest few main reasons limiting the experiment: First the insufficient signal-to-noise ratio which is due to the large X-ray absorption of the Si membrane, together with the already limited number of X-ray photons per pulse (see chapter 2.3.3). Second, sample stability must be taken into account. A long time exposure at a repetition rate of 3 kHz shows a detrimental effect to the cap layer that result in a non switchable layer. This can possibly be overcome by using a ZnS/SiO₂ capping layer instead of Si_xN_y. Improvements in the measurements geometry (e.g. reflectance configuration) might overcome the problem of photons being absorbed by the Si membrane, since samples could be grown on conventional Si(111) substrates and only the

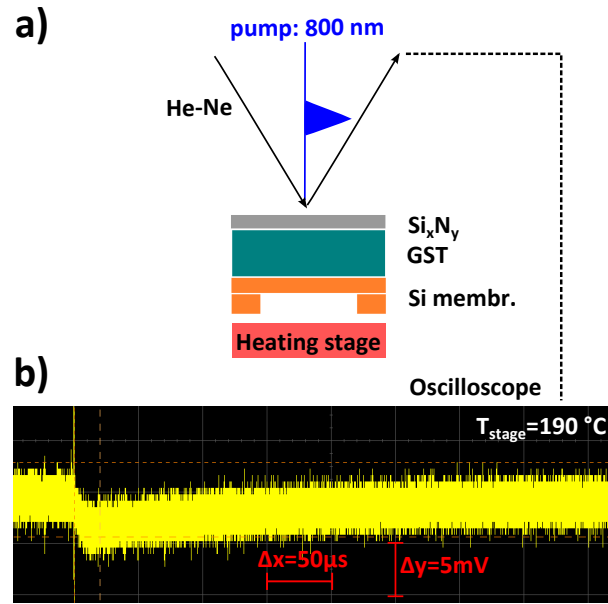


Figure 5.4: a) Schematic of the *in situ* recrystallization experiment after amorphization by application of 800 nm laser pump. He-Ne laser is overlapped to the pump in order to monitor the reflectivity change on the sample. Signal is detected and sent to the oscilloscope b) Example of typical oscilloscope image showing reflectivity drop and recovering due to recrystallization by annealing.

pumped GST film would contribute to the detected X-ray signal by properly choosing a good combination between incidence angle, penetration depth of pump and probe and thickness of the film itself.

5.2 Terahertz Spectroscopy for Dynamic Investigations of GeSbTe Alloys and Chalcogenide Superlattices

As already mentioned in chapter 2.3, a collaboration with the THz beamline at Bessy II was pursued to realize the first ultrafast dynamic investigation of PCM in a optical-pump/THz-probe scheme. Exploiting THz light sensitivity to free carriers and phonon modes, we aimed at discriminating conductivity changes in PCM and CSL.

5.2.1 Static Terahertz Contrast between Amorphous and Crystalline GeSbTe Alloys

Following the procedure of the XAS pump/probe experiment presented in previous section, also in this case static spectroscopy has first been performed on the different GST and CSL samples in order to test the suitability of the measurement for our material system. This led to a series of

optimization of both sample preparation and beamline setup in order to maximize the signal-to-noise ratio. In addition such static measurements resulted in the comprehension of fundamental open questions, as discussed in chapter 4.1.2.

In the static measurements shown in fig. 5.5, the used a- and c-GST films of 60 nm thickness and GST225 nominal composition were grown by MBE on highly insulating Si wafers, ensuring highly textured and ordered material as compared to conventionally used poly-GST. The details on growth and XRD characterization of a- and c-GST have been discussed in chapter 3 and can be found in Bragaglia *et al.*^[94,103]. A highly resistive bare Si wafer (5 k Ω cm) is used as a reference. All the samples were capped with with 35 nm ZnS-SiO₂ to prevent oxidation.

The THz transmittance measurements taken with the FTIR spectroscopy (see chapter 2.3.1) on a- and ordered c-GST films (blue and orange curves, respectively) are shown in fig. 5.5 a). The spectra are normalized to the Si substrate. The a-GST film (ble curve) shows almost no absorption owing to its low concentration of free carriers and low mobility, which is in agreement with the insulating nature of the amorphous state. On the contrary, the crystalline state (orange curve) shows a strong absorption over the whole spectrum with a broad feature centered at 70 cm⁻¹, resulting in ~ 60 % difference in transmittance. In a-GST, carriers are localized^[3,26,62] while in c-GST delocalized electrons allow for conduction^[26,62]. Such strong absorption is in accordance with low temperature electrical measurements, displaying a metallic behavior with a low DC-resistivity value of 10⁻³ Ω cm and mobility value of $\mu = 12$ cm²/Vs at RT (see chapter 4). Static transmittance for a 80 nm CSL 3-1 is also shown for completeness (green curve). The heterostructure, similarly to the GST alloy (orange curve), shows a strong metallic behavior with consequent small transmission in the whole spectral range and a the minimum of ~ 0.2 at ~ 70 cm⁻¹ [fig. 5.5 a)]. The latter can be explained similarly to the case of GST IR-active mode presented in chapter 4.1.2 (see discussion about fig. 4.3), with a superposition of Sb₂Te₃ and GST modes. Nevertheless, mode assignment and Raman study of CSLs has not been the objective of this thesis work. Dedicated CSL time-resolved study follows in section 5.2.3.

5.2.2 Time-Resolved Ultrafast Dynamics in GeSbTe Alloys

Upon laser pumping, a signal increase is expected when full switching from c- to a-GST is induced [see blue arrow in fig. 5.5 a)]. For pulse energies too low to drive the c- to a-GST phase transition (sub-threshold pumping), the transmittance must instead drop (orange arrow), as excess photo-induced carriers lead to additional absorption. Pumping a-GST can only cause a transmittance drop due to either photo-excited carriers or a- to c-GST transition [opposite direction of blue arrow in fig. 5.5 a)]. These considerations are supported by the dedicated study on absorption change upon *in situ* annealing of GST that have been shown in chapter 4.1.2. a-GST showed a general increase in absorption for increasing T_A , with phonon appearance as fingerprint of the structural transition and free carrier evolution as an indication of the metallic properties of the crystallized GST (see discussion about fig. 4.4). If the transmittance is considered, for increasing T_A a-GST transmittance drops from 1 to a lower value comparable with the orange curve corresponding

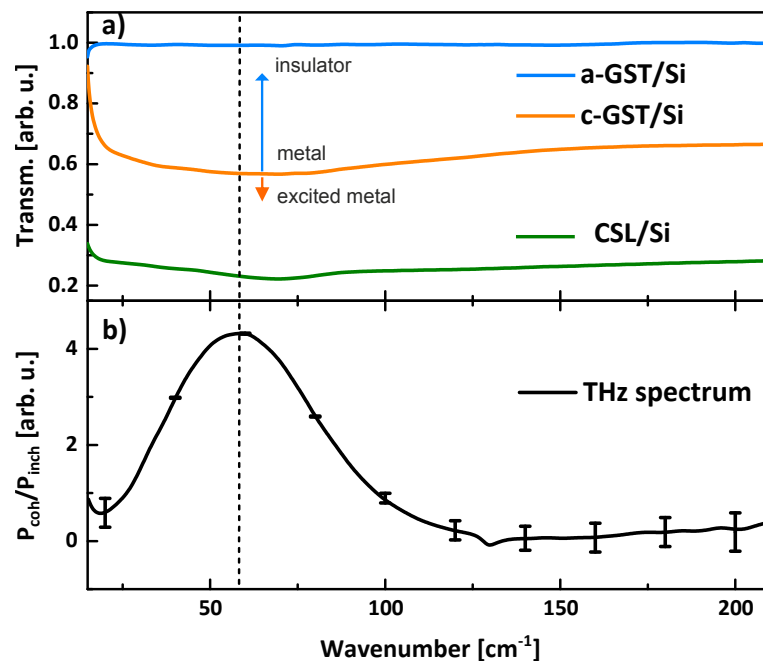


Figure 5.5: a) Measured transmission of the as grown a-GST (blue) and ordered c-GST (orange) films. CSL 3-1 is also shown in green. b) Measured intensity spectrum of the THz probe pulse chosen for the current study. All measurements are obtained from the FTIR spectroscopy with a 4.2 K Si-bolometer at the Bruker IFS 125HR spectrometer with 6 μm Mylar beamsplitter. The probe pulse spectra in b) is normalized to the incoherent background spectrum, as emitted from all the other bunches in the laser-OFF case. Reprints from^[102].

to as grown c-GST (not shown). It is important to recall, that even if the annealing experiments clearly suggest a transmittance drop upon crystallization, those experiments occur within several minutes.

Several preliminary steps have to be realized before performing the pump/probe experiment. In the ideal case, for such kind of experiment an insulating substrate is used to ensure the total transparency to both laser-pump and THz-probe. This has not been possible within our study, since optimization of c-GST growth on different substrate lead to the result that Si(111) is the optimal choice to obtain quasi-single-crystalline GST with highly-ordered distribution of vacancies (see chapter 3.1). Therefore a different solution has been adopted in order to optimize the signal detection, consisting in choosing the right thickness of the GST films. It has to be taken into account that the penetration depths of both pump and probe in the a- and c-GST are different. On the one hand we need the probe to pass through the excited samples and be detected, on the other we need to ensure that we are exciting only the film.

For c-GST, 60 nm thickness resulted to be ideal compromise in order to have high crystalline quality sample and good pump/probe signal detection. For clarity, in the scheme below (fig. 5.6), the result of a multilayer model simulation based on the method by K. Ohta *et al.*^[129] is shown (n and k , real and imaginary refractive indexes, respectively, are taken from literature^[130]), in order to evaluate the absorbed/transmitted power of the 800 nm laser pump in the c-GST sample. We clearly see that the pump power is only absorbed by the 60 nm c-GST layer. In addition such thickness is expected to avoid the injection of electrons from the GST into the silicon, which might alter the GST dynamics.

For a-GST larger penetration depth of the laser-pump and high transparency to the THz-probe was found during first calibration experiments (for a-GST thickness 100 nm still Si excited carriers dominate the dynamics). Therefore, 60 nm thick a-GST was grown on quartz substrate, which does not represent a problem from a growth point of view, as opposed to the c-GST. Samples were capped with 35 nm ZnS-SiO₂ to prevent oxidation.

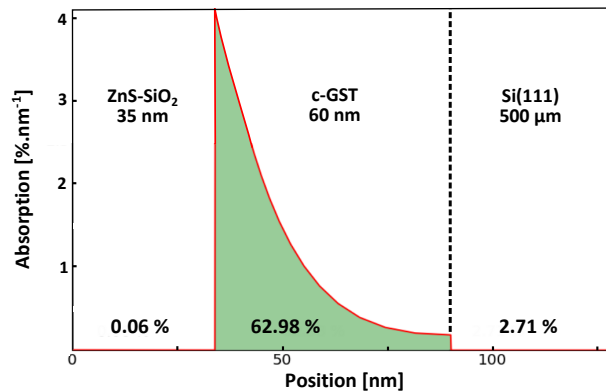


Figure 5.6: The power absorption [%·nm⁻¹] of the 800 nm laser in a multilayer system composed by 35 nm ZnS-SiO₂ capping, 60 nm c-GST and 500 μm Si(111).

Fig. 5.5 b) shows measured intensity spectrum of the THz probe pulse chosen for the current study. In order to discriminate whether the dynamics in our material system are influenced by being resonant or not with the IR phonon, time-resolved curves for Sb_2Te_3 , which presents the strongest IR phonon contribution respect to GST and GeTe (shown in chapter 4.1.2), have been compared by changing the position of the THz spectra in respect to the phonon (see chapter 2.3.2 for the method). No changes have been found, indication of the fact that the carrier dynamics are dominating the THz signal evolution (not shown).

THz time traces up to 15 ps delay time for the x- and a-GST at incident fluence of $1.5 \text{ mJ}/\text{cm}^2$ are shown in fig. 5.7 (orange and blue symbols, respectively). The THz transmittance curves are normalized to the unpumped case. Both phases show a sub-ps drop of the signal at τ_0 , which is attributed to the photo-injection of carriers, on a time scale much shorter than the temporal resolution of the experiment [$\sim 0.7 \text{ ps}$; see the gray peak at τ_0 in fig. 2.8 b) of chapter 2.3]. The THz dynamic signal for a-GST practically fully recovers within 7 ps following a single exponential decay with a recovery time of $\tau_{\text{short}} = 2 \text{ ps}$. In c-GST for the same incident sub-threshold fluence, more carriers are excited in accordance with its metallic behavior. In addition, the THz-transmittance can be fitted by a double exponential decay function multiplied with a Heavyside function and both are convoluted with a Gaussian (gray pulse in fig. 5.7), to account for the temporal resolution. From the fit, two recovery times are extracted: a short one and a long one. The short one with a recovery time constant $\tau_{\text{short}} = 0.8 \text{ ps}$ is faster than the value previously reported in the literature^[65]. The long one stems for a recovery time of $\tau_{\text{long}} = 90 \text{ ps}$ and indicates a slow dissipation of the remaining excess carriers. In the inset, the c-GST transmission change is shown for delay times up to 120 ps revealing the longer recovery time τ_{long} .

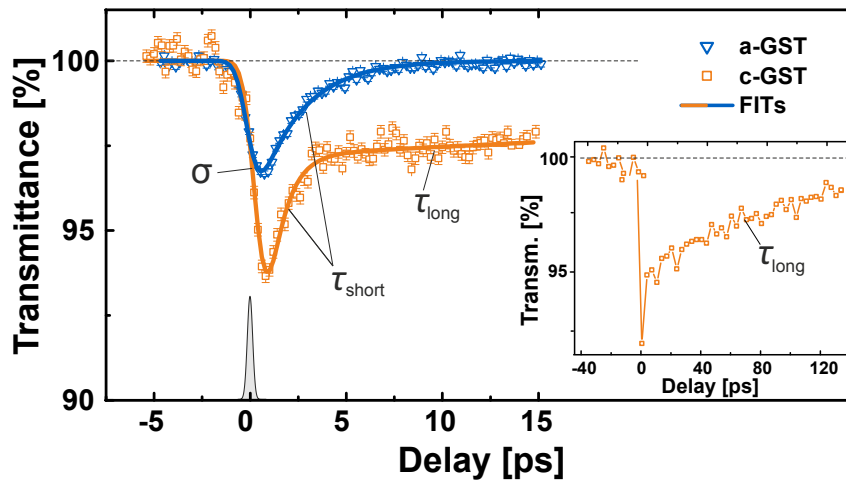


Figure 5.7: THz transmission change of the as grown a- (blue triangles) and c- (orange squares) GST225 films. Fits of the experimental data are superimposed. Measurements are done with short delay scans (15 ps) to resolve the instantaneous excitation and the short recovery time τ_{short} . In the inset, the c-GST transmission change is shown for delay times up to 120 ps revealing the longer recovery time τ_{long} .

Series of delay scans for different incident fluence values have been measured and are shown in fig. 5.8 a) and b) for a-GST and c-GST, respectively. The curves are plotted with an offset for clarity. For a-GST, in the range of fluences investigated, i.e. from 0.1 to 1.7 mJ/cm², an increase of photo-excited carrier is observed for increasing laser fluence, with a total transmittance change of $\sim 3\%$ [see inset in fig. 5.8 a)]. The transmittance change as function of fluence shows a linear trend. Similar argument holds for c-GST, where increase of fluence corresponds to a even bigger drop in transmittance. Nevertheless, in a similar range of employed powers as in the a-GST case, higher percentage of total transmittance change is observed [$\sim 8\%$, as shown in the inset of fig. 5.8 b)]. In fact, in accordance with its metallic behavior, more carriers are excited. Let's recall that a pump-induced decrease of the THz transmission, or increase of the THz absorption, can be phenomenologically attributed to an increase of the conductivity in the material.

If we focus on the recovery of the transmittance in both cases, several distinctions can be done: a-GST shows only one recovery time τ_{short} , and its value as a function of fluence is plotted in fig. 5.8 c). Recovery τ_{short} decreases for increasing fluences, nevertheless, all corresponding curves show a total recover to the initial transmission value within ~ 10 ps. This can be interpreted in terms of carriers scattering rate increase, i.e. for increasing density of carriers, more carriers scatter and relax per ps. Instead, for c-GST both short and long recovery coexist. The τ_{short} presents sub-ps time scale with a maximum value of 0.85 ps for fluence of 2.1 mJ/cm²; note that for very low fluences τ_{short} has values at the limit of the time resolution. The τ_{long} values instead, show an increase from 30 ps to 90 ps for increasing fluence values. This means that recovery is slower for increasing density of carriers. Similar carrier behavior has been observed on a short time scale (< 3 ps) in a full optical pump/probe study on poly-GST^[4]. The opposite time constant behavior between a- and c-GST might suggest that depending on the phase, different physical processes come into play.

It is well established that laser pumping perturbs the initial Fermi distribution of free carriers in a system: The laser pulses create hot carriers that are not in thermal equilibrium and within a few hundred fs, a new Fermi distribution is reached via strong carrier-carrier scattering, resulting in a thermalized free carrier gas with higher temperature than the lattice (hot carriers). Subsequently within the following ps the carriers cool down and relaxes by releasing its excess energy to the lattice through different possible mechanisms such as carrier-phonon coupling and/or a combination of phonon emission, Auger recombination, radiative recombination, and diffusion. As a consequence, lattice temperature rises. The degree of lattice heating also depends on the injected laser power in the system, and can result in both the expansion of the lattice and the increased of vibrational motion. Cooling of accumulated thermal heating is expected to happen on ns timescale^[65], which is out of our investigated time range.

Optical excitation of GST at 800 nm (1.55 eV) generates free carriers by interband transitions. The enhanced free-carrier density increases the plasma frequency, which decreases ϵ_1 and increases ϵ_2 , the real and imaginary part of the dielectric function ϵ of a material, respectively. Such changes are small in a full optical pump/probe at 800 nm^[131]. Within our experiment, instead, the low frequency range (see chapter 2.3) is free carrier sensitive^[132], and resonant to IR-active phonons in the material.

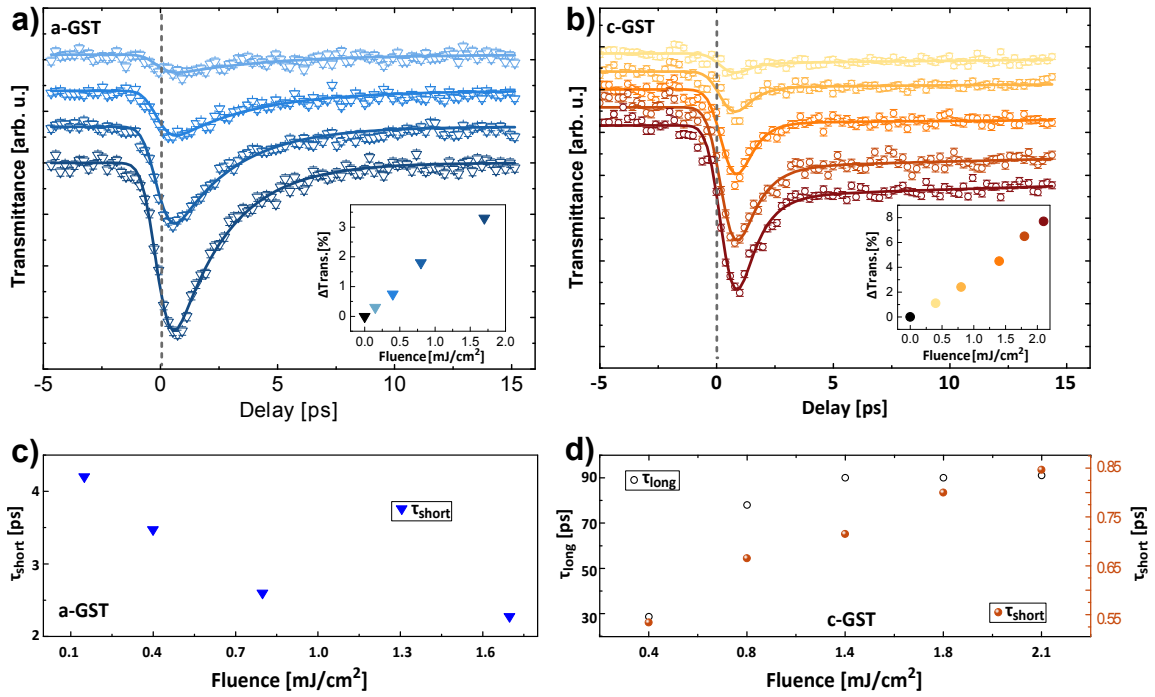


Figure 5.8: Short delay scans (15 ps) of THz transmission change for different applied laser fluences are shown for: a) a-GST (blue triangles) and b) c-GST (orange squares). Fits of the experimental data are superimposed. The percentage of transmittance change as function of fluence for a- and c-GST are plotted in the corresponding insets. Recovery times as function of fluence are plotted in c) for a-GST and d) for c-GST.

In our specific case, within the short carrier recombination time shown in fig. 5.8, it is reasonable to assume an interplay between different fast recombination pathways. These may contain electron-phonon scattering as well as recombination via traps and defects. In particular, traps and defects play a fundamental role in a-GST due to its band structure, as introduced in section 1.2.1^[2,57]. Possible fast recombination pathways for both phases through Raman and IR active phonons are also expected, as the measurements are performed in a spectral region where Raman and IR modes activity have been evidenced (see study in chapter 4.1.2^[102]). Their oscillations are not visible in the THz signal probably due to small oscillation period in respect to the resolution of the experiment, e.g. the IR active mode oscillation period is ~ 0.5 ps, according to $T = 1/\nu$, where ν is the frequency of the phonon mode. Discrepancies in the short time scales between the present work and Ref.^[65] are attributed to the improved epitaxial sample quality. The long recovery for the crystalline phase was not observed before in the poly-GST samples^[65]. Furthermore, heating effects can be excluded as the origin of such long recovery due to the fact that they should happen on ns timescale^[65]. Based on the studies presented in chapters 3.1.1 and 4, which shows how structure and conduction properties of epitaxially grown ordered c-GST^[94,102] are strongly connected, we speculate that the longer recovery might be linked to the presence of ordered vacancy layers. The latter could represent another recombination channel for photo-excited carriers that cannot recombine through alternative faster path ways. Furthermore, within the employed fluences, no ultrafast amorphization of c-GST is evidenced (increased transmittance expected) as discussed before for fig. 5.5 a).

5.2.3 Time-Resolved Ultrafast Dynamics in Chalcogenide Superlattices

In this section the results of the optical-pump/THz-probe investigation of CSLs are presented. Similarly to the case of GST, multilayer model simulations have been performed in order to evaluate the absorbed/transmitted power of the 800 nm laser-pump in the samples and determine the optimal thickness for the time resolved experiments. An example for CSL (3-1) \times 15 is shown in fig. 5.9. In the simulation n and k are taken from literature^[130], and the heterostructure is simulated according to its really obtained structure, i.e. 2 nm Sb₂Te₃ and 2 nm GST, as discussed in chapter 3.2. For CSL (3-1) \times 15, 60 nm thickness resulted to be ideal compromise in order to have high quality sample and good pump/probe signal detection, with a 63.04 % absorbed power in the film and negligible 1.37 % of transmitted power. Same simulations have been performed also on other CSLs with different periodicities (3-2, 3-3 and 6-4); as a result, a minimum thickness of 60 nm is desirable to have negligible transmitted laser power through the Si substrate (< 1.7 %).

In fig. 5.10 a) THz transmittance change of CSL (3-1) \times 15 as function of delay time is shown for different pump fluence (see labels). The curves are plotted with an offset for clarity. It is interesting to note that different transmittance evolution is present if compared with the study on a- and ordered c-GST [fig. 5.8 a), b)].

A first remarkable consideration concerns the fluence range employed, which is much lower if

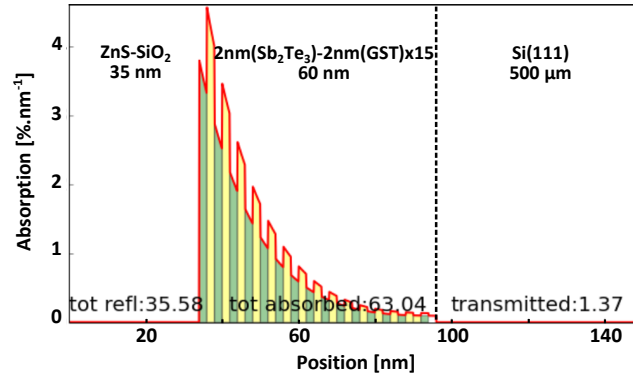


Figure 5.9: The power absorption [%·nm⁻¹] of the 800 nm laser in a multilayer system composed by 35 nm ZnS-SiO₂ capping, 60 nm nominal CSL (3-1)×15 and 500 μm Si(111).

compared with a- and c-GST: Up to 1 order of magnitude lower fluences with 0.02 mJ/cm² for CSL, 0.1 mJ/cm² for a-GST and 0.4 mJ/cm² for c-GST.

Immediately after excitation (τ_0), the three curves corresponding to fluences from 0.02 to 0.1 mJ/cm² show an increase of transmission above the 100 % starting value (indicated for each curve by horizontal dotted lines) from 0.3 to 0.5 % of the initial value, indicative of a small effect. Such transmittance increase subsequently decreases till the original 100 % value within few ps (8 ps for the highest fluence of 0.1 mJ/cm²). A pump-induced increase of the THz transmission, or a decrease of the THz absorption corresponds to a decrease of the THz conductivity. When incident fluence is further increased (0.13 mJ/cm²), a drop in the signal is visible after τ_0 (0.4 % decrease) followed by a recovery, which actually leads to an increase of transmittance above 100 % and a further drop, as for the lower fluence cases. A long recovery for $t > 8$ ps is also visible. Similar transmittance evolution is found for 0.19 mJ/cm² too. Here, however, the higher number of excited carriers (larger drop of signal 0.9 %) does not lead to an increase above the starting value. The transmittance maximum observed for 0.02 mJ/cm² at 1.1 ps shifts toward 4.1 ps for 0.19 mJ/cm².

Two major time constants have been considered to describe the carrier dynamics: τ_1 is the time constant which stems for the increase of transmittance [see label in fig. 5.10 a)], τ_2 describes the recovery from the previous transmittance increase [see label in fig. 5.10 b)]. The change of τ_1 and τ_2 depending on the applied fluence is shown in fig. 5.10 b). Both display a non linear increase for increasing fluence values.

The interpretation of the transmittance evolution is not trivial, especially due to the fact that for higher fluence values different dynamics seem to come into play. If we start from the first three curves, which present only one characteristic feature, a first complication arises from the fact that an increase of transmittance above the 100 % line might be ascribed to an amorphization of the CSL upon laser pumping. However, the reversibility of the process (signal recovery to 100 % line), strongly suggests that it is more reasonable to assume an ultrafast "disordering" that leads to a decrease in conduction, without invoking a permanent phase transition. Based on the structural knowledge we have on the as grown CSL, it is reasonable to assume that such disordering is

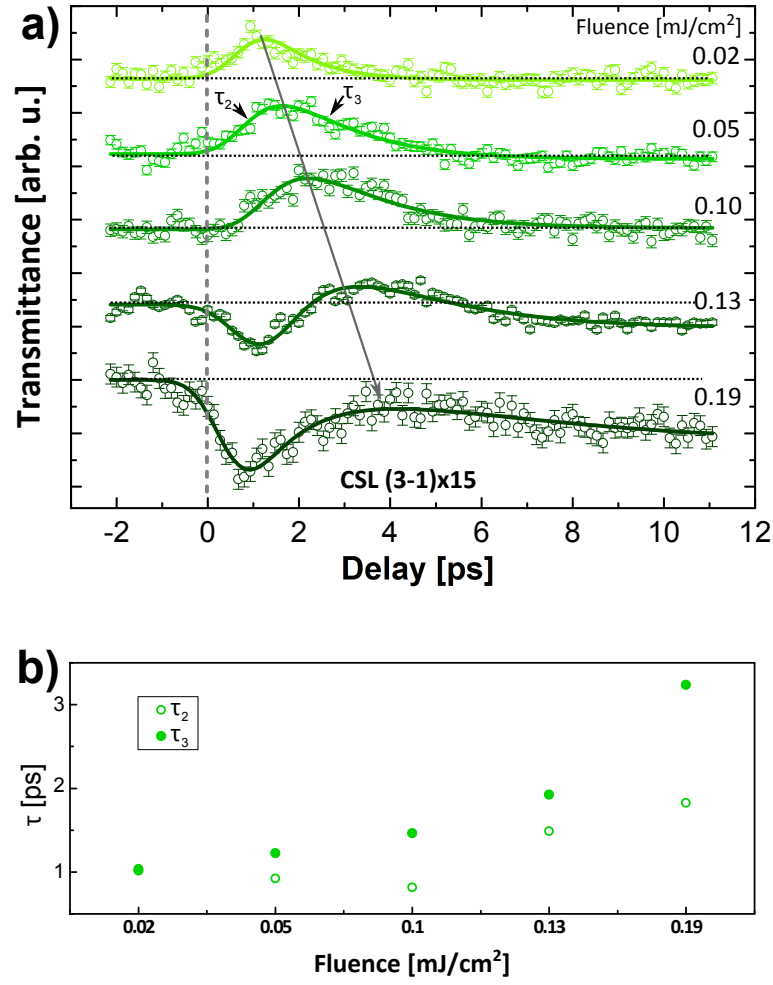


Figure 5.10: a) THz transmittance change in CSL (3-1)×15 for different applied laser fluences is shown. Fits of the experimental data are superimposed; b) time constants τ_1 and τ_2 as function of applied fluence are shown.

happening at the interfaces between Sb_2Te_3 and GST blocks, which presents many discontinuities of the vdW gaps^[53,54] (see chapter 3.2). At higher fluence values, a sub-ps transmittance drop, and a very long recovery time above 8 ps occur [see last two curves in fig. 5.10 a)]. Such behavior has been observed also in c-GST. All these observations suggest that the CSL transmittance evolution might be arising from a competing bulk/interface effect. Let us recall that GST shows dynamics only starting from $0.4 \text{ mJ}/\text{cm}^2$ [see fig. 5.8 b)], same holds for bulk GeTe and Sb_2Te_3 (not shown). Transmittance drop and immediate recover through single τ_{short} characterizes both GeTe and Sb_2Te_3 (not shown). If a transmittance drop and recovery is the sign for a bulk-like behavior, we have to notice that for CSLs this effect can be achieved at lower fluences and follows that of c-GST with two recovery time constants.

In a CSL annealing study of R. Wang^[52], it has been shown that for 400°C , the CSL transforms into ordered GST. This highlights an intrinsic thermodynamic tendency toward intermixing, as found already during MBE growth^[53,54], above a certain energy barrier. This result and the evolution of the curves in fig. 5.10 suggest that for increasing fluences, if enough heat is accumulated into the lattice, the CSL would start to transform into GST, and the corresponding THz signal would be comparable with the one of fig. 5.8. Such intermixing and consequent loss of the CSL structure is therefore expected to happen earlier than a permanent amorphization of the heterostructure. Within the employed fluences, reproducibility of the measurements shown in fig. 5.10 a) indicates that intermixing can be excluded.

A CSL with 6-4 periodicity and 70 nm thick has also been measured for comparison. In this sample we increase the bulk at the expenses of the interface. In addition, the relative presence of the two constituents changes from 3 (CSL 3-1) to 1.5 (CSL 6-4). The result of the time-resolved measurement is shown in fig. 5.11 for two fluences in which also a rise and drop are obtained. Curves are plotted with an offset and smoothed with an adjacent-average method for clarity. 100 % transmittance lines are shown as guide for the eye. For fluence of $0.08 \text{ mJ}/\text{cm}^2$, a total transmittance increase of $\sim 0.1 \%$ is obtained (see label in fig. 5.11). By increasing the fluence $0.13 \text{ mJ}/\text{cm}^2$, the signal drops $\sim 0.3 \%$ (see label in fig. 5.11), and subsequently rises above the 100 % original transmission. A recovery to the original value follows. The overall lower effect made the measurements of such CSL more challenging, requiring longer integration times compared to the CSL 3-1. In particular, the smaller effect of the interface disordering might support the fact that a superlattice with higher proportion of interfaces in the film is desirable for switching application. This is in agreement with the result reported by the group of Tominaga that suggest the 3-1 sequence to be the best in terms of performances.

Furthermore, also electrical switching results from the PASTRY project support such interpretation. Within this project, MBE grown CSL memory cells were produced: The growth recipe on silicon presented in chapter 3.2 was adapted by Dr. J. Boschker in order to grow the CSLs in test vehicles engineered in collaboration with Micron Microelectronics^[11]. The switching performances in terms of programming currents of MBE grown CSLs are on par with, or better, than the ones of state of the art CSL cells, if 3-1 periodicity is considered (see fig. 4.22 in R. Wang thesis^[52]). MBE grown CSLs 6-4 instead, do show lower performances if compared to the CSL 3-1 and to MBE grown poly-GST.

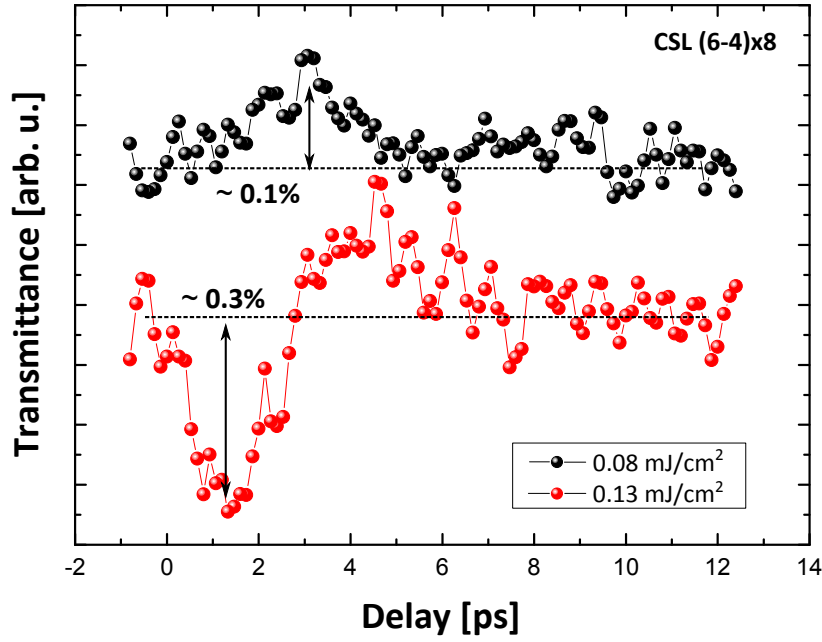


Figure 5.11: THz transmittance change in CSL (6-4)×7 for 0.13 and 0.08 mJ/cm² applied laser fluences is shown. 100 % transmittance line are shown as guide for the eye.

In addition, as introduced in chapter 1.3.1, switching in CSL happens between two crystalline states, i.e. one conducting (*LRS*) and the other highly resistive (*HRS*), as opposed to conventional GST where switching occurs between amorphous and crystalline phases. Electrical characterization show that MBE grown CSL 3-1 memory cells as grown display a resistance value of $10^4 \Omega$, instead, *HRS* of $10^7 \Omega$ is obtained after electrical switching with a programming current (I_{prog}) at least 1/3 lower than that necessary to switch GST (unpublished data). Therefore, interface response might represent the key to understand the *HRS* in PCMSLs.

Further analysis and conductivity simulations taking into account structural properties are necessary to reach a deeper understanding of the switching mechanism which makes PCMSL more superior compared to conventional PCM.

The comparison of electrical data with optical pump/probe reveals that in both cases lower power (low I_{prog} , low fluences) is used to induce the switching or its precursor. In both cases we do not amorphize the sample, but induce a disordering process. The latter, as from pump/probe data, is possibly arising at the interface, thus it explains why CSLs with relatively too high bulk contribution do not switch as nicely as those with larger interface contribution.

5.3 Summary and Conclusions

In this chapter we focused on the time-resolved investigations of PCM materials performed employing synchrotron based radiation. The optically induced ultrafast dynamics have been studied within two different spectroscopy methods, i.e. XAS and THz light absorption. In the first case by X-ray with energies between 1220 and 1240 eV, we were aiming at probing electronic DOS changes in Ge atom environment and link them to the structural difference between a- and x-

phases, exploiting the sensitivity of such technique to electronic structure. Instead, by using THz spectroscopy, we aimed at identifying conductivity changes between a- and ordered c-GST phase and CSLs, exploiting FIR-THz frequency range sensitivity to free carrier dynamics.

In the first section 5.1, samples suitable for XAS in transmission mode have been successfully fabricated and the difference in XAS spectra at the Ge L3 edge between crystalline and laser amorphized GeTe has been confirmed. The possible impact of pump effects at the Ge L3 edge seems to be extremely small or occurs only on a very short timescale < 100 fs, which makes optical-pump/XAS-probe extremely challenging: No time dependent change in the electronic structure was observed either working in sub-threshold regime or by inducing reversible switching in the material. Limits in the experiment are the sample damage upon laser-pump exposure and the insufficient signal-to-noise ratio which is due to the large X-ray absorption of the Si membrane together with the low number of X-ray photons per pulse.

In the second section 5.2, a successful optical-pump/THz-probe approach is presented, and the obtained results are here summarized. It has been shown that 800 nm optical-pump and THz-probe measurements by tunable THz-CSR pulses in combination with static THz-FTIR spectroscopy provide a powerful tool to study the ultrafast light induced conductivity changes in PCM materials. Benefiting from the properties of a THz-CSR based set-up, we could tune the probe pulse to a specific energy window, thereby providing ultimate sensitivity to the transient transmittance changes in the ps-regime. Measuring the THz transmittance following a 100 fs optical pulse, we revealed that within the employed range of fluences (0.1 to 2.1 mJ/cm²) a decrease in transmittance, indication of strong free carrier absorption, is observed for both a- and c-GST. Furthermore, no ultrafast amorphization of c-GST is evidenced (increased transmittance expected). As deposited, a-GST is dominated only by a short recovery time of excited carriers τ_{short} , as opposed to c-GST that exhibits a bi-exponential decay: A short one with τ_{short} of a sub-ps timescale followed by a long one with $\tau_{\text{long}} > 30$ ps, a clear indication of the fact that for epitaxially grown crystalline structures at least two channels for carrier dissipation are present. The longer recovery time, which is not observed in the poly-GST, might be due to the presence of vacancies ordered into layers, which strongly affect the electronic and conduction properties of c-GST, as demonstrated in chapters 3.1.1 and 4^[94,102].

CSLs have also been investigated by optical-pump/THz-probe. Range of fluences employed to resolve dynamics is lower than in the GST alloy (up to 1 order of magnitude lower fluences with 0.02 mJ/cm² for CSL, 0.1 mJ/cm² for a-GST and 0.4 mJ/cm² for c-GST). The major difference in respect to the GST alloy consists in the presence of a feature, in which an increase of the transmitted signal above the 100 % original value followed by a recovery is observed. Such feature persists in the curves for all the employed fluences, even if for increasing fluences, a competing carrier excitation followed by a very long recovery time starts to be resolved and dominate the THz response. The overall effect percentage are lower if compared to the bulk a- and c-GST (not exceeding 0.9 % change in transmittance in CSL and ~ 8 % in c-GST). The feature leading to an increase of transmittance followed by a recovery has been attributed to an ultrafast reversible "disordering" located at the interfaces of the CSL. Instead, the carrier excitation followed by the

long recovery time presents similarities with the ordered c-GST response, and not with GeTe or Sb₂Te₃, measured as references. The comparison between CSLs with less interface as compared to the 3-1 sequence leads to a strong reduction of the measured effect. Therefore we hypothesize that CSL response is characterized by bulk/interface competing mechanisms.

Conclusions and outlook

This thesis work fundamentally advances the understanding of the role of intrinsic vacancies on the conduction properties of the Ge-Sb-Te alloys (GST). Global characterization methods such as XRD, Raman and FIR spectroscopy have been used in concert, complementing and corroborating each other in unequivocally showing that vacancy ordering into layers drives the metal-insulator transition (MIT) in GST.

This result has been obtained by first assessing the vacancy ordering in MBE grown GST samples employing TEM and XRD characterization, which has been compared to DFT simulations of the GST crystal structures. The understanding of the ordering process enabled the fine tuning of the ordering degree by changing growth parameters, such as the Ge, Sb, Te fluxes and the substrate temperature. Different growth windows have been explored, employing *in situ* RHEED and *ex situ* sample characterization by XRD and Raman spectroscopy. A phase diagram has been realized as output of this study. It is shown that the Te flux plays a fundamental role in the growth kinetics, determining the composition, crystalline phase and ordering of the GST. These three effects are not completely decoupled. Nevertheless, by changing the Te flux, either directly or indirectly by modifying the substrate temperature, it is possible to obtain different growth windows in which compositional tuning and different crystalline phases can be fabricated. A high degree of vacancy ordering in GST is also obtained through annealing and via fs-pulse laser crystallization of amorphous GST (a-GST) deposited on a crystalline substrate, which acts as a template for the crystallization. This finding is remarkable as it demonstrates that it is possible to create ordered cubic GST (c-GST) layers using different fabrication procedures.

The possibility to tune the degree of vacancy ordering in GST has been combined with a study of its transport properties, by comparing electrical measurements with XRD for GST samples annealed at various temperatures, and hence different degrees of vacancy ordering. A transition from insulating to metallic behavior is observed as soon as the vacancies start to order into layers. MBE grown samples are found to be in the metallic state with different resistivity values depending on the degree of ordering. Vibrational modes and carrier behavior in amorphous and crystalline phases have also been studied by temperature dependent Raman and FIR spectroscopy, enabling the extraction of activation energies for electron conduction for both cubic and trigonal GST phases, and the determination of the MIT in a temperature range corresponding to the onset of the disordered to ordered cubic transition, consistently with the electrical study.

Therefore, within the context of phase transition and MIT in GST, light was shed on many points, which were till now only theoretically predicted^[16] or not fully understood^[26].

Conclusions and outlook

The results obtained in the study of ordered GST laid the groundwork for the investigation of crystalline superlattices (CSLs), which resemble the ordered GST structure due to the presence of periodic vdW gaps in between building blocks of alternating Te, Sb and Ge layers. Dynamic investigations of both GST and CSLs have been performed, employing complementary time-resolved techniques. This work was driven by the necessity to understand the mechanism at the base of CSL switching, expected to be by far more efficient than melting in conventional phase-change-material (PCM) based memories, and to enable ultra-low energy consumption, .

In chapter 5 is shown how within a first optical-pump/XAS-probe investigation, samples suitable for XAS in transmission mode have been successfully fabricated. Furthermore, the difference in XAS spectra at the Ge L3 edge between crystalline and laser amorphized PCM has been confirmed. Such contrast could in principle be used for dynamic investigation, in order to reveal the change in the electronic structure around the Ge atoms in PCM. However, no time dependent change in the electronic structure was observed either working in the sub-threshold regime or by inducing reversible switching in the material. This suggests that the impact of pump effects at the Ge L3 edge is extremely small or occurs only on a very short timescale < 100 fs, which makes optical-pump/XAS-probe extremely challenging. The main limitations of the experiment were the insufficient signal-to-noise ratio, which was due to the large X-ray absorption of the Si membrane together with the low number of X-ray photons per pulse, and the sample damage upon laser-pump exposure. For the future it would be interesting to change the measurements geometry (to reflectance or electron detection) or to perform single-shot pump/probe measurements on samples mounted on rotating holders.

Another major result of this thesis work is the realization of successful optical-pump/THz-probe experiment. The sensitivity of THz-probe to sample conductivity has been exploited to investigate both GST and CSLs grown by MBE.

Measuring the THz transmittance of both a- and ordered c-GST following a 100 fs optical pulse, we revealed a decrease in transmittance within the employed range of fluences (0.1 to 2.1 mJ/cm²), indication of strong free carrier absorption. As deposited a-GST is dominated only by a short recovery time of excited carriers τ_{short} , as opposed to c-GST that exhibits a bi-exponential decay: A short decay with τ_{short} on a sub-ps timescale followed by a long decay with $\tau_{\text{long}} > 30$ ps, a clear indication that for epitaxially grown crystalline structures at least two channels for carrier dissipation are present. The longer recovery time, which is not observed in the polycrystalline GST, might be due to the presence of vacancies ordered into layers.

In CSLs, the range of fluences employed to resolve the carrier dynamics is lower than in the GST alloy (up to 1 order of magnitude lower fluences). The major difference with respect to the GST alloy is the presence of a feature in which an increase of the transmitted signal above the 100 % original value followed by a recovery is observed upon pumping. Such features persist in the curves for all the employed fluences. For increasing fluences, a competing carrier excitation followed by a very long recovery time starts to be resolved and then dominates the THz response, similarly to the c-GST response. Such an increase of transmittance followed by a recovery has been attributed to an ultrafast reversible "disordering" located at the interfaces of the CSL, which

are preferential sites for disordering effects due to the presence of defects. Therefore we hypothesize that the CSL response is characterized by bulk/interface competing mechanisms. The comparison between CSLs with different number of interfaces confirmed our assumption. Further comparison of electrical data with optical-pump/THz-probe data reveals that in both cases lower power (low programming currents, low fluences) is used to induce the switching or its precursor. In both cases we do not amorphize the sample, but induce a disordering process. The latter is possibly arising at the interface, thus it explains why CSLs with a too high bulk contribution do not switch as nicely as those with a low one.

As an outlook for the future, it would be interesting to grow CLSs with controlled atomic inclusions in the vdW gaps at the interfaces, which are expected to influence the switching performances of the superlattice itself. Such atomic inclusions could be accessed by TEM and XRD characterization methods. The different CSLs would then be characterized electrically and by THz-probe. Such a strategy is expected to provide an understanding of the switching mechanism for unveiling the atomistic mechanism behind it. In fact, the expected conduction changes, accessed by the two methods, might shed light on the exact interface effect, and would offer a path for an optimization work in order to maximize the performance of CSL based memory cells.

Appendix

List of Samples Prepared by Molecular Beam Epitaxy

All MBE growths that I have performed are listed in the table below following a chronological order.

Sample ID	Description	# of samples
s2_0751, s2_0760	First c- and a-GST.	2
s2_0779	c-GST on InAs	1
s2_0781	c-GST on Si membrane for <i>ex situ</i> measurements in transmission at the BESSY II beamline tests	1
s2_0794	c-GST on InAs for collaboration with Oxford University	1
s2_0798, s2_0805	a-GST for annealing experiments	2
s2_0803	Te calibration	1
s2_0804	Sb ₂ Te ₃ Test sample on SiO ₂ for pastry	1
s2_0806	Sb ₂ Te ₃ Test sample for Pastry on SiN	1
s2_0812	Pastry Sb ₂ Te ₃ on Carbon	1
s2_0813, s2_0814	CSL for collaboration with Dr. Malvestuto	2
s2_0820, s2_0822, s2_0831, s2_0849	GST on high resistive Si for transp meas.	4
s2_0844	a-SL for Dr. Malvestuto	1
s2_0848	c-GST on Si(111) high resistive for collaboration with Dr. Privitera	1
s2_0874	GST on high resistive Si first sample after Te filling	1
s2_0875, s2_0877-s2_0879, s2_0882	GST on high resistive Si	5
s2_0881, s2_0883	ZnS-SiO ₂ capping calibration	2
s2_0884	CSL on high resistive Si	1

List of Samples Prepared by Molecular Beam Epitaxy

s2_0899, s2_0901, s2_0907	CSL (3-1)×5 with Sb ₂ Te ₃ buffer layer with Prof. Arciprete	3
s2_0908-s2_0910	CSL (3-1)×5 with Sb ₂ Te ₃ buffer layer on highly resistive Si(111) with Prof. Arciprete	3
s2_0921, s2_0923, s2_0924, s2_0928	GST for composition change study with Prof. Arciprete	4
s2_0922	Test of a-GST225 on crystalline quartz for THz measurements	1
s2_0926, s2_0942, s2_0945	Te, Sb calibration samples	3
s2_0939, s2_0940	Sb ₂ Te ₃ and GeTe on highly resistive Si(111) to use as reference	2
s2_0946, s2_0947, s2_0952	CSL 3-3, CSL 3-2 and CSL 6-4 with Sb ₂ Te ₃ buffer layer	3
s2_0971	a-GST for annealing experiments	1
s2_1001-s2_1002	CSL for EXAFS beamtime at ELETTRA	2
s2_1004-s2_1008	GST substrate temperature study	5
s2_1027, s2_1028, s2_1034-s2_1037, s2_1040-s2_1041, s2_1043-s2_1051	Ge, Sb, Te calibrations samples	17
s2_1054	c-GST on Si(111)	1
s2_1055	ZnS-SiO ₂ calibration sample	1
s2_1056-s2_1068, s2_1070, s2_1072	Sb, Te, Ge calibrations	14
s2_1069, s2_1071, s2_1073-s2_1075	c-GST samples for growth studies with Prof. Arciprete	5
s2_1080, s2_1081, s2_1095, s2_1098, s2_1099	c-GST samples for growth studies with Prof. Arciprete	7

Total count	100
--------------------	------------

Bibliography

- [1] T. Matsunaga, R. Kojima, and N. Yamada, "Overview of the GeTe-Sb₂Te₃ pseudobinary crystalline phase," *epcos.org*, **3**, 1–9 (2007).
- [2] S. Raoux, W. Wehnich, and D. Ielmini, "Phase change materials and their application to non-volatile memories.," *Chemical reviews*, **110**, 240–267 (2010).
- [3] K. Shportko, S. Kremers, M. Woda, D. Lencer, J. Robertson, and M. Wuttig, "Resonant bonding in crystalline phase-change materials," *Nature Materials*, **7**, 653–658 (2008).
- [4] L. Waldecker, T. a. Miller, M. Rudé, R. Bertoni, J. Osmond, V. Pruneri, R. E. Simpson, R. Ernstorfer, and S. Wall, "Time-domain separation of optical properties from structural transitions in resonantly bonded materials," *Nature Materials*, **14**, 1–6 (2015).
- [5] R. E. Simpson, P. Fons, A. Kolobov, T. Fukaya, M. Krbal, T. Yagi, and J. Tominaga, "Interfacial phase-change memory.," *Nature nanotechnology*, **6**, 501–505 (2011).
- [6] W. Wehnich, S. Botti, L. Reining, and M. Wuttig, "Origin of the optical contrast in phase-change materials," *Physical review letters*, **98**, 236403 1–4 (2007).
- [7] S.K.Bahl and K.L.Chopra, "Amorphous versus Crystalline GeTe Films. III. Electrical Properties and Band Structure," *Journal of Applied Physics*, **41**, 2196–2212 (1970).
- [8] S. Raoux, "Phase Change Materials," *Annual Review of Materials Research*, **39**, 25–48 (2009).
- [9] H.-S. P. Wong, S. Raoux, S. Kim, J. Liang, J. P. Reifenberg, B. Rajendran, M. Asheghi, and K. E. Goodson, "Phase Change Memory.," *Proceedings of the IEEE*, **98**, 2201–2227 (2010).
- [10] M. Wuttig and N. Yamada, "Phase-change materials for rewriteable data storage," *Nature Materials*, **6**, 824–832 (2007).
- [11] J. E. Boschker, M. Boniardi, A. Redaelli, H. Riechert, and R. Calarco, "Electrical performance of phase change memory cells with Ge₃Sb₂Te₆ deposited by molecular beam epitaxy," *Applied Physics Letters*, **106**, 023117 (2015).
- [12] D. Loke, T. Lee, W. Wang, L. Shi, R. Zhao, Y. Yeo, T. Chong, and S. Elliott, "Breaking the speed limits of phase-change memory.," *Science*, **336**, 1566 (2012).
- [13] M. Wuttig, D. Lüsebrink, D. Wamwangi, W. Wehnich, M. Gillessen, and R. Dronskowski, "The role of vacancies and local distortions in the design of new phase-change materials.," *Nature materials*, **6**, 122–8 (2007).

Bibliography

- [14] T. Matsunaga, N. Yamada, and Y. Kubota, "Structures of stable and metastable $\text{Ge}_2\text{Sb}_2\text{Te}_5$, an intermetallic compound in $\text{GeTe-Sb}_2\text{Te}_3$ pseudobinary systems," *Acta crystallographica. Section B, Structural science*, **60**, 685–91 (2004).
- [15] B. J. Kooi and J. T. M. De Hosson, "Electron diffraction and high-resolution transmission electron microscopy of the high temperature crystal structures of $\text{Ge}_x\text{Sb}_2\text{Te}_{3+x}$ ($x=1,2,3$) phase change material," *Journal of Applied Physics*, **92**, 3584 (2002).
- [16] W. Zhang, A. Thiess, P. Zalden, R. Zeller, P. H. Dederichs, J.-Y. Raty, M. Wuttig, S. Blügel, and R. Mazzarello, "Role of vacancies in metal-insulator transitions of crystalline phase-change materials.," *Nature materials*, **11**, 952–6 (2012).
- [17] Z. Sun, J. Zhou, and R. Ahuja, "Structure of Phase Change Materials for Data Storage," *Physical Review Letters*, **96**, 055507 (2006).
- [18] J. Hegedus and S. R. Elliott, "Microscopic origin of the fast crystallization ability of Ge-Sb-Te phase-change memory materials," *Nature Materials*, **7**, 399–405 (2008).
- [19] P. Jónvári, I. Kaban, J. Steiner, B. Beuneu, A. Schöps, and M. A. Webb, "Local order in amorphous $\text{Ge}_2\text{Sb}_2\text{Te}_5$ and $\text{Ge}_1\text{Sb}_2\text{Te}_4$," *Physical Review B*, **77**, 4–9 (2008).
- [20] J. Robertson, K. Xiong, and P. Peacock, "Electronic and atomic structure of $\text{Ge}_2\text{Sb}_2\text{Te}_5$ phase change memory material," *Thin Solid Films*, **515**, 7538–7541 (2007).
- [21] P. B. Littlewood, "The crystal structure of IV-VI compounds : I . Classification," *J. Phys. C*, **13**, 4855–4873 (1980).
- [22] D. Lencer, M. Salinga, B. Grabowski, T. Hickel, J. Neugebauer, and M. Wuttig, "A map for phase-change materials.," *Nature materials*, **7**, 972–7 (2008).
- [23] P. P. Edwards, T. V. Ramakrishnan, and C. N. R. Rao, "The Metal-Nonmetal Transition: A Global Perspective," *Journal of Physical Chemistry*, **99**, 5228–5239, (1995).
- [24] P. W. Anderson, "Absence of diffusion in certain random lattices," *Physical Review*, **109**, 1492–1505 (1958).
- [25] N. Mott, "Metal-insulator transitions," **382**, 1–24 (1982).
- [26] T. Siegrist, P. Jost, H. Volker, M. Woda, P. Merkelbach, C. Schlockermann, and M. Wuttig, "Disorder-induced localization in crystalline phase-change materials," *Nature Materials*, **10**, 202–208 (2011).
- [27] M. N. Touzelbaev, P. Zhou, R. Venkatasubramanian, and K. E. Goodson, "Thermal characterization of $\text{Bi}_2\text{Te}_3/\text{Sb}_2\text{Te}_3$ superlattices," *Journal of Applied Physics*, **90**, 763–767 (2001).
- [28] S. Lee, K. Esfarjani, T. Luo, J. Zhou, Z. Tian, and G. Chen, "Resonant bonding leads to low lattice thermal conductivity," *Nature Communications*, **5**, 1–8 (2014).
- [29] N. Mott and E. Davis, *Electronic Processes in Non-Crystalline Materials (Oxford Classic Texts in the Physical Sciences)*. Oxford University Press, second ed. (2012).

- [30] C. Wood, "Materials for thermoelectric energy conversion," *Reports on Progress in Physics*, **51**, 459-539 (1999).
- [31] D. Wu, L. D. Zhao, S. Hao, Q. Jiang, F. Zheng, J. W. Doak, H. Wu, H. Chi, Y. Gelbstein, C. Uher, C. Wolverton, M. Kanatzidis, and J. He, "Origin of the high performance in GeTe-based thermoelectric materials upon Bi₂Te₃ doping," *Journal of the American Chemical Society*, **136**, 11412–11419 (2014).
- [32] J. J. Gervacio-Arciniega, E. Prokhorov, F. J. Espinoza-Beltran, and G. Trapaga, "Characterization of local piezoelectric behavior of ferroelectric GeTe and Ge₂Sb₂Te₅ thin films," *Journal of Applied Physics*, **112**, 052018 (2012).
- [33] M. J. Polking, M.-G. Han, A. Yourdkhani, V. Petkov, C. F. Kisielowski, V. V. Volkov, Y. Zhu, G. Caruntu, A. P. Alivisatos, and R. Ramesh, "Ferroelectric order in individual nanometre-scale crystals," *Nature materials*, **11**, 700–9 (2012).
- [34] A. V. Kolobov, P. Fons, M. Krbal, J. Tominaga, a. Giussani, K. Perumal, H. Riechert, R. Calarco, and T. Uruga, "Local structure of epitaxial GeTe and Ge₂Sb₂Te₅ films grown on InAs and Si substrates with (100) and (111) orientations: An x-ray absorption near-edge structure study," *Journal of Applied Physics*, **117**, 125308 (2015).
- [35] G. Bruns, P. Merkelbach, C. Schlockermann, M. Salinga, M. Wuttig, T. D. Happ, J. B. Philipp, and M. Kund, "Nanosecond switching in GeTe phase change memory cells," *Applied Physics Letters*, **95**, 043108 (2009).
- [36] M. Liebmann, C. Rinaldi, D. Di Sante, J. Kellner, C. Pauly, R. N. Wang, J. E. Boschker, A. Giussani, S. Bertoli, M. Cantoni, L. Baldrati, M. Asa, I. Vobornik, G. Panaccione, D. Marchenko, J. Sánchez-Barriga, O. Rader, R. Calarco, S. Picozzi, R. Bertacco, and M. Morgenstern, "Giant Rashba-Type Spin Splitting in Ferroelectric GeTe(111)," *Advanced Materials*, **28**, 560–565 (2016).
- [37] T. Nonaka, G. Ohbayashi, Y. Toriumi, Y. Mori, and H. Hashimoto, "Crystal structure of GeTe and Ge₂Sb₂Te₅ meta-stable phase," *Thin Solid Films*, **370**, 258–261 (2000).
- [38] V. L. Deringer, M. Lumeij, and R. Dronskowski, "Ab Initio Modeling of α -GeTe(111) Surfaces," *The Journal of Physical Chemistry C*, **116**, 15801–15811 (2012).
- [39] R. Wang, D. Campi, M. Bernasconi, J. Momand, B. J. Kooi, M. A. Verheijen, M. Wuttig, and R. Calarco, "Ordered Peierls distortion prevented at growth onset of GeTe ultra-thin films," *Scientific Reports*, **6**, 32895 (2016).
- [40] R. Wang, J. E. Boschker, E. Bruyer, D. D. Sante, S. Picozzi, K. Perumal, A. Giussani, H. Riechert, and R. Calarco, "Toward truly single crystalline GeTe films: The relevance of the substrate surface," *The Journal of Physical Chemistry C*, **118**, 29724–29730 (2014).
- [41] T. C. Chong, L. P. Shi, X. S. Miao, P. K. Tan, R. Zhao, and Z. P. Cai, "Study of the Superlattice-Like Phase Change Optical Recording Disks," *Japanese Journal of Applied Physics*, **39**, 737–740 (2000).

Bibliography

- [42] Y. Cao and W. Qiang, "On the properties of GeTe/Sb₂Te₃ superlattice-like structure for phase-change optical recording," *Proc. SPIE*, **6029**, ICO20 (2006).
- [43] T. C. Chong, L. P. Shi, R. Zhao, P. K. Tan, J. M. Li, H. K. Lee, X. S. Miao, a. Y. Du, and C. H. Tung, "Phase change random access memory cell with superlattice-like structure," *Applied Physics Letters*, **88**, 122114 (2006).
- [44] C. Kim, D. Kang, T.-Y. Lee, K.-B. K. H. P. Kim, Y.-S. Kang, J. Lee, S.-W. Nam, and Y. Khang, "Direct evidence of phase separation in Ge₂Sb₂Te₅ in phase change memory devices," *Applied Physics Letters*, **94**, 193504 (2009).
- [45] T.-Y. Yang, I.-M. Park, B.-J. Kim, and Y.-C. Joo, "Atomic migration in molten and crystalline Ge₂Sb₂Te₅ under high electric field," *Applied Physics Letters*, **95**, 32103–32104 (2009).
- [46] Y. Saito, J. Tominaga, P. Fons, A. V. Kolobov, and T. Nakano, "Ab-initio calculations and structural studies of (SiTe)₂(Sb₂Te₃)_n (n : 1, 2, 4 and 6) phase-change superlattice films," *physica status solidi (RRL) - Rapid Research Letters*, **8**, 302–306 (2014).
- [47] T. Ohyanagi, M. Kitamura, M. Araidai, S. Kato, N. Takaura, and K. Shiraishi, "GeTe sequences in superlattice phase change memories and their electrical characteristics," *Applied Physics Letters*, **104**, 252106 (2014).
- [48] J. Tominaga, A. V. Kolobov, P. Fons, T. Nakano, and S. Murakami, "Ferroelectric Order Control of the Dirac-Semimetal Phase in GeTe-Sb₂Te₃ Superlattices," *Advanced Materials Interfaces*, **1**, 1300027 (2014).
- [49] X. Yu and J. Robertson, "Modeling of switching mechanism in GeSbTe chalcogenide superlattices," *Scientific Reports*, **5**, 12612 (2015).
- [50] K. Makino, J. Tominaga, and M. Hase, "Ultrafast optical manipulation of atomic arrangements in chalcogenide alloy memory materials.," *Optics express*, **19**, 1260–70 (2011).
- [51] J. Tominaga, P. Fons, A. V. Kolobov, T. Shima, T. C. Chong, R. Zhao, H. K. Lee, and L. Shi, "Role of Ge Switch in Phase Transition: Approach using Atomically Controlled GeTe/Sb₂Te₃ Superlattice," *Japanese Journal of Applied Physics*, **47**, 5763–5766 (2008).
- [52] R. N. Wang, *Epitaxial growth and characterization of GeTe and GeTe/Sb₂Te₃ superlattices*. Phd thesis, Humboldt-Universität (2016).
- [53] R. Wang, V. Bragaglia, J. E. Boschker, and R. Calarco, "Intermixing during Epitaxial Growth of van der Waals Bonded Nominal GeTe/Sb₂Te₃ Superlattices," *Crystal Growth & Design*, **16**, 3596–3601 (2016).
- [54] J. Momand, R. Wang, J. E. Boschker, M. A. Verheijen, R. Calarco, and B. J. Kooi, "Interface formation of two- and three-dimensionally bonded materials in the case of GeTe-Sb₂Te₃ superlattices," *Nanoscale*, **7**, 19136–19143 (2015).

- [55] B. Casarin, A. Caretta, J. Momand, B. J. Kooi, M. A. Verheijen, V. Bragaglia, R. Calarco, M. Chukalina, X. Yu, J. Robertson, F. R. L. Lange, M. Wuttig, A. Redaelli, E. Varesi, F. Parmigiani, and M. Malvestuto, "Revisiting the Local Structure in Ge-Sb-Te based Chalcogenide Superlattices," *Scientific Reports*, **6**, 22353 (2016).
- [56] A. Lacaïta, "Phase change memories: State-of-the-art, challenges and perspectives," *Solid-State Electronics*, **50**, 24–31 (2006).
- [57] D. Ielmini, "Threshold switching mechanism by high-field energy gain in the hopping transport of chalcogenide glasses," *Physical Review B*, **78**, 1–8 (2008).
- [58] K. V. Mitrofanov, P. Fons, K. Makino, R. Terashima, T. Shimada, A. V. Kolobov, J. Tominaga, V. Bragaglia, A. Giussani, R. Calarco, H. Riechert, T. Sato, T. Katayama, K. Ogawa, T. Togashi, M. Yabashi, S. Wall, D. Brewe, and M. Hase, "Sub-nanometre resolution of atomic motion during electronic excitation in phase-change materials," *Scientific Reports*, **6**, 20633 (2016).
- [59] P. Fons, P. Rodenbach, K. V. Mitrofanov, A. V. Kolobov, J. Tominaga, R. Shayduk, A. Giussani, R. Calarco, M. Hanke, H. Riechert, R. E. Simpson, and M. Hase, "Picosecond strain dynamics in Ge₂Sb₂Te₅ monitored by time-resolved X-ray diffraction," *Physical Review B*, **90**, 094305 (2014).
- [60] M. J. Shu, P. Zalden, F. Chen, B. Weems, I. Chatzakis, F. Xiong, R. Jeyasingh, M. C. Hoffmann, E. Pop, H.-S. Philip Wong, M. Wuttig, and A. M. Lindenberg, "Ultrafast terahertz-induced response of GeSbTe phase-change materials," *Applied Physics Letters*, **104**, 251907 (2014).
- [61] A. V. Kolobov, P. Fons, A. I. Frenkel, A. L. Ankudinov, J. Tominaga, and T. Uruga, "Understanding the phase-change mechanism of rewritable optical media," *Nature materials*, **3**, 703–708 (2004).
- [62] B. Huang and J. Robertson, "Bonding origin of optical contrast in phase-change memory materials," *Physical Review B*, **81**, 081204 (2010).
- [63] F. Gericke, T. Flissikowski, J. Lahnemann, F. Katmis, W. Braun, H. Riechert, and H. T. Grahn, "Optical switching and related structural properties of epitaxial Ge₂Sb₂Te₅ films," *Journal of Applied Physics*, **111**, 113524 1–4 (2012).
- [64] P. Rodenbach, A. Giussani, K. Perumal, M. Hanke, M. Dubsclaff, H. Riechert, R. Calarco, M. Burghammer, A. V. Kolobov, and P. Fons, "Recrystallization of an amorphized epitaxial phase-change alloy: A phoenix arising from the ashes," *Applied Physics Letters*, **101**, 061903 (2012).
- [65] M. J. Shu, I. Chatzakis, Y. Kuo, P. Zalden, and A. M. Lindenberg, "Ultrafast sub-threshold photo-induced response in crystalline and amorphous GeSbTe thin films," *Applied Physics Letters*, **102**, 201903 (2013).

Bibliography

- [66] M. Wienold, L. Schrottke, M. Giehler, R. Hey, W. Anders, and H. T. Grahn, "Low-threshold terahertz quantum-cascade lasers based on GaAs/Al_{0.25}Ga_{0.75}As heterostructures," *Applied Physics Letters*, **97**, 071113 (2010).
- [67] M. Musolino, D. van Treeck, A. Tahraoui, L. Scarparo, C. D. Santi, M. Meneghini, E. Zanoni, L. Geelhaar, and H. Riechert, "A physical model for the reverse leakage current in (In,Ga)N/GaN light-emitting diodes based on nanowires," *Journal of Applied Physics*, **119**, 044502 (2016).
- [68] M. Mandl, X. Wang, T. Schimpke, C. Kölper, M. Binder, J. Ledig, A. Waag, X. Kong, A. Trampert, F. Bertram, J. Christen, F. Barbagini, E. Calleja, and M. Strassburg, "Group III nitride core-shell nano- and microrods for optoelectronic applications," *Physica Status Solidi - Rapid Research Letters*, **7**, 800–814 (2013).
- [69] I. V. Markov, *Crystal growth for beginners: Fundamentals of Nucleation, Crystal Growth and Epitaxy*. World Scientific Publishing Company, (2003).
- [70] J. Narayan and B. C. Larson, "Domain epitaxy: A unified paradigm for thin film growth," *Journal of Applied Physics*, **93**, 278 (2003).
- [71] I. K. Robinson, "Crystal truncation rods and surface roughness," *Physical Review B*, **33**, 3830–3836 (1986).
- [72] J. Zhang, J. Neave, B. Joyce, P. Dobson, and P. Fawcett, "On the RHEED specular beam and its intensity oscillation during MBE growth of GaAs," *Surface Science*, **231**, 379–388 (1990).
- [73] C. Rulliere, *Femtosecond Laser Pulses*. Springer, second ed. (2005).
- [74] M. Birkholz, *Thin Film Analysis by X-Ray Scattering*. WILEY-VCH Verlag GmbH & Co. KGaA, 2006.
- [75] G. V. Hansson, H. H. Radamsson, and W.-X. Ni, "Strain and relaxation in Si-MBE structures studied by reciprocal space mapping using high resolution X-ray diffraction," *Journal of Materials Science: Materials in Electronics*, **6**, 292–297 (1995).
- [76] L. van der Pauw, "A method of measuring specific resistivity and hall effect of discs of arbitrary shape," tech. rep., Philips research lab, Eindhoven, (1958).
- [77] D. A. Long, *Raman Spectroscopy*. New York: Mc-Grw-Hill (1977).
- [78] K. Holldack, J. Bahrdt, A. Balzer, U. Bovensiepen, M. Brzhezinskaya, A. Erko, A. Eschenlohr, R. Follath, A. Firsov, W. Frentrop, L. Le Guyader, T. Kachel, P. Kuske, R. Mitzner, R. Müller, N. Pontius, T. Quast, I. Radu, J.-S. Schmidt, C. Schüßler-Langeheine, M. Sperling, C. Stamm, C. Trabant, and A. Föhlisch, "FemtoSpeX: a versatile optical pump–soft X-ray probe facility with 100 fs X-ray pulses of variable polarization," *Journal of Synchrotron Radiation*, **21**, 1090–1104 (2014).
- [79] K. Holldack and A. Schnegg, "THz Electron Paramagnetic Resonance/THz Spectroscopy at BESSY II," *Journal of large-scale research facilities JLSRF*, **2**, A51 (2016).

- [80] W. S. Lau, *Infrared characterization for microelectronics*. World Scientific Publishing Company (1999).
- [81] G. Bauer and W. Richter, *Optical Characterization of Epitaxial Semiconductor Layers*. Springer Berlin Heidelberg (1996).
- [82] J. C. Lindon, G. E. Tranter, and D. W. Koppenaal, *Encyclopedia of spectroscopy and spectrometry*. third ed. (2017).
- [83] K. Holldack, S. Khan, R. Mitzner, and T. Quast, "Femtosecond terahertz radiation from femtoslicing at BESSY," *Physical Review Letters*, **96**, 1–4 (2006).
- [84] A. Zholents and K. Holldack, in *Proceedings of the Free Electron Laser Conference FEL 2006, Berlin, Germany*, 725 (2006).
- [85] J. M. Byrd, Z. Hao, M. C. Martin, D. S. Robin, F. Sannibale, R. W. Schoenlein, A. A. Zholents, and M. S. Zolotarev, "Tailored Terahertz Pulses from a Laser-Modulated Electron Beam," *Physical Review Letters*, **96**, 164801 (2006).
- [86] E. E. Alp, S. M. Mini, and M. Ramanathan, "Chapter 3: X-Ray Absorption Spectroscopy: EXAFS and XANES - A Versatile Tool to Study the Atomic and Electronic Structure of Materials" *Proceedings of a workshop held at Argonne National Laboratory* (1990)
- [87] D. E. Sayers, E. A. Stern, and F. W. Lytle, "New Technique for Investigating Noncrystalline Structures: Fourier Analysis of the Extended X-Ray—Absorption Fine Structure," *Physical Review Letters*, **27**, 1204–1207, (1971).
- [88] K. Perumal, W. Braun, H. Riechert, and R. Calarco, "Growth control of epitaxial GeTe–Sb₂Te₃ films using a line-of-sight quadrupole mass spectrometer," *Journal of Crystal Growth*, **396**, 50–53 (2014).
- [89] J. E. Boschker, J. Momand, V. Bragaglia, R. Wang, K. Perumal, A. Giussani, B. J. Kooi, H. Riechert, and R. Calarco, "Surface reconstruction-induced coincidence lattice formation between two-dimensionally bonded materials and a three-dimensionally bonded substrate.," *Nano letters*, **14**, 3534–3538 (2014).
- [90] A. Koma, "Van der Waals epitaxy—a new epitaxial growth method for a highly lattice-mismatched system," *Thin Solid Films*, **216**, 72–76 (1992).
- [91] M. Grundmann, "Formation of epitaxial domains: Unified theory and survey of experimental results," *Physica Status Solidi (B)*, **248**, 805–824 (2011).
- [92] CrystalMaker, "Software Oxford, United Kingdom."
- [93] J. Da Silva, A. Walsh, and H. Lee, "Insights into the structure of the stable and metastable (GeTe)_m(Sb₂Te₃)_n compounds," *Physical Review B*, **78**, 224111 (2008).

Bibliography

- [94] V. Bragaglia, F. Arciprete, W. Zhang, A. M. Mio, E. Zallo, K. Perumal, A. Giussani, S. Cecchi, J. E. Boschker, H. Riechert, S. Privitera, E. Rimini, R. Mazzarello, and R. Calarco, "Metal - insulator transition driven by vacancy ordering in GeSbTe phase change materials," *Scientific Reports*, **6**, 23843 (2016).
- [95] W. Braun, "Epitaxy of phase change materials," in *Spring MRS 2010*, 1–32 (2010).
- [96] R. Shayduk and W. Braun, "Epitaxial films for Ge-Sb-Te phase change memory," *Journal of Crystal Growth*, **311**, 2215–2219 (2009).
- [97] A. M. Mio, S. M. Privitera, V. Bragaglia, F. Arciprete, C. Bongiorno, R. Calarco, and E. Rimini, "Chemical and structural arrangement of the trigonal phase in GeSbTe thin films," *Nanotechnology*, **28**, 065706 (2017).
- [98] E. Zallo, S. Cecchi, J. E. Boschker, A. M. Mio, F. Arciprete, S. Privitera, and R. Calarco, "Modulation of van der Waals epitaxy induced by strain control at the step edges," *Scientific Reports*, *accepted* (2017).
- [99] A. W. Searcy, "The Vapor Pressure of Germanium 1," *Journal of the American Chemical Society*, **74**, 4789–4791 (1952).
- [100] J. J. Doolan and J. R. Partington, "The vapour pressure of tellurium," *Transactions of the Faraday Society*, **20**, 342 (1924).
- [101] E. Zallo, R. Wang, V. Bragaglia, and R. Calarco, "Laser induced structural transformation in chalcogenide based superlattices," *Applied Physics Letters*, **108**, 221904 (2016).
- [102] V. Bragaglia, K. Holldack, J. E. Boschker, F. Arciprete, E. Zallo, T. Flissikowski, and R. Calarco, "Far-Infrared and Raman Spectroscopy Investigation of Phonon Modes in Amorphous and Crystalline Epitaxial GeTe-Sb₂Te₃ Alloys," *Scientific Reports*, **6**, 28560 (2016).
- [103] V. Bragaglia, B. Jenichen, A. Giussani, K. Perumal, H. Riechert, and R. Calarco, "Structural change upon annealing of amorphous GeSbTe grown on Si(111)," *Journal of Applied Physics*, **116**, 054913 (2014).
- [104] K. Perumal, *Epitaxial Growth of Ge-Sb-Te based Phase Change Materials*. PhD thesis (2013).
- [105] J. E. Boschker, E. Tisbi, E. Placidi, J. Momand, A. Redaelli, B. J. Kooi, F. Arciprete, and R. Calarco, "Textured Sb₂Te₃ films and GeTe/ Sb₂Te₃ superlattices grown on amorphous substrates by molecular beam epitaxy," *AIP Advances*, **7**, 015106, (2017).
- [106] B. Sa, J. Zhou, Z. Sun, J. Tominaga, and R. Ahuja, "Topological Insulating in GeTe/Sb₂Te₃ Phase-Change Superlattice," *Physical Review Letters*, **109**, 096802 (2012).
- [107] J. Kalb, F. Spaepen, and M. Wuttig, "Atomic force microscopy measurements of crystal nucleation and growth rates in thin films of amorphous Te alloys," *Applied Physics Letters*, **84**, 5240–5242 (2004).

- [108] I. Friedrich, V. Weidenhof, W. Njoroge, P. Franz, and M. Wuttig, "Structural transformations of $\text{Ge}_2\text{Sb}_2\text{Te}_5$ films studied by electrical resistance measurements," *Journal of Applied Physics*, **87**, 4130–4134 (2000).
- [109] S. Raoux, J. L. Jordan-Sweet, and A. J. Kellock, "Crystallization properties of ultrathin phase change films," *Journal of Applied Physics*, **103**, 114310 (2008).
- [110] A. M. Mio, S. M. Privitera, V. Bragaglia, F. Arciprete, S. Cecchi, G. Litrico, C. Persch, R. Calarco, and E. Rimini, "Role of interfaces on the stability and electrical properties of $\text{Ge}_2\text{Sb}_2\text{Te}_5$ crystalline structures," *Scientific Reports*, under review (2017).
- [111] A. Debunne, K. Virwani, A. Padilla, G. W. Burr, A. J. Kellock, V. R. Deline, R. M. Shelby, and B. Jackson, "Evidence of Crystallization–Induced Segregation in the Phase Change Material Te-Rich GST," *Journal of The Electrochemical Society*, **158**, H965 (2011).
- [112] J. E. Boschker, R. N. Wang, V. Bragaglia, P. Fons, A. Giussani, L. L. Guyader, M. Beye, I. Radu, A. V. Kolobov, K. Holldack, and R. Calarco, "Laser-driven switching dynamics in phase change materials investigated by time-resolved X-ray absorption spectroscopy," *Phase Transitions*, **88**, 82–89 (2015).
- [113] V. Bragaglia, A. Schnegg, R. Calarco, and K. Holldack, "Epitaxial $\text{Ge}_2\text{Sb}_2\text{Te}_5$ probed by single cycle THz pulses of coherent synchrotron radiation," *Applied Physics Letters*, **109**, 141903 (2016).
- [114] I. Ronneberger, W. Zhang, H. Eshet, and R. Mazzarello, "Crystallization Properties of the $\text{Ge}_2\text{Sb}_2\text{Te}_5$ Phase-Change Compound from Advanced Simulations," *Advanced Functional Materials*, **25**, 6407–6413 (2015).
- [115] W. Braun, R. Shayduk, T. Flissikowski, M. Ramsteiner, H. T. Grahn, H. Riechert, P. Fons, and A. V. Kolobov, "Epitaxy of Ge–Sb–Te phase-change memory alloys," *Applied Physics Letters*, **94**, 041902 (2009).
- [116] M. Foerst, T. Dekorsy, C. Trappe, M. Laurenzis, H. Kurz, and B. Bechevet, "Phase change in $\text{Ge}_2\text{Sb}_2\text{Te}_5$ films investigated by coherent phonon spectroscopy," *Applied Physics Letters*, **77**, 1964 (2000).
- [117] K. Andrikopoulos, S. Yannopoulos, A. Kolobov, P. Fons, and J. Tominaga, "Raman scattering study of GeTe and $\text{Ge}_2\text{Sb}_2\text{Te}_5$ phase-change materials," *Journal of Physics and Chemistry of Solids*, **68**, 1074–1078 (2007).
- [118] W. Richter, A. Krost, U. Nowak, and E. Anastassakis, "Anisotropy and dispersion of coupled plasmon-LO-phonon modes in Sb_2Te_3 ," *Zeitschrift für Kristallographie Physik B Condensed Matter*, **49**, 191–198 (1982).
- [119] E. Steigmeier and G. Harbeke, "Soft phonon mode and ferroelectricity in GeTe," *Solid State Communications*, **8**, 1275–1279 (1970).
- [120] G. C. Sosso, S. Caravati, R. Mazzarello, and M. Bernasconi, "Raman spectra of cubic and amorphous $\text{Ge}_2\text{Sb}_2\text{Te}_5$ from first principles," *Physical Review B*, **83**, 134201 (2011).

Bibliography

- [121] Y. Chen, D. O. Dumcenco, Y. Zhu, X. Zhang, N. Mao, Q. Feng, M. Zhang, J. Zhang, P.-H. Tan, Y.-S. Huang, and L. Xie, "Composition-dependent Raman modes of $\text{Mo}_{1-x}\text{W}_x\text{S}_2$ monolayer alloys," *Nanoscale*, **6**, 2833 (2014).
- [122] G. C. Sosso, S. Caravati, C. Gatti, S. Assoni, and M. Bernasconi, "Vibrational properties of hexagonal $\text{Ge}_2\text{Sb}_2\text{Te}_5$ from first principles.," *Journal of physics. Condensed matter : an Institute of Physics journal*, **21**, 245401 (2009).
- [123] A. Shalini, Y. Liu, F. Katmis, W. Braun, G. P. Srivastava, and R. J. Hicken, "Coherent phonon modes of crystalline and amorphous $\text{Ge}_2\text{Sb}_2\text{Te}_5$ thin films: A fingerprint of structure and bonding," *Journal of Applied Physics*, **117**, 025306 (2015).
- [124] S. Privitera, E. Rimini, and R. Zonca, "Amorphous-to-crystal transition of nitrogen- and oxygen-doped $\text{Ge}_2\text{Sb}_2\text{Te}_5$ films studied by in situ resistance measurements," *Applied Physics Letters*, **85**, 3044 (2004).
- [125] L. Xu, L. Tong, L. Geng, F. Yang, J. Xu, W. Su, D. Liu, Z. Ma, and K. Chen, "A comparative study on electrical transport properties of thin films of $\text{Ge}_1\text{Sb}_2\text{Te}_4$ and $\text{Ge}_2\text{Sb}_2\text{Te}_5$ phase-change materials," *Journal of Applied Physics*, **110**, 013703 (2011).
- [126] P. Rodenbach, *Switching of Epitaxial Phase Change Materials*. PhD thesis, Freie Universität Berlin (2012).
- [127] M. Krbal, A. Kolobov, P. Fons, J. Tominaga, S. Elliott, J. Hegedus, A. Giussani, K. Perumal, R. Calarco, T. Matsunaga, N. Yamada, K. Nitta, and T. Uruga, "Crystalline GeTe-based phase-change alloys: Disorder in order," *Physical Review B*, **86**, 045212 (2012).
- [128] M. Salinga, E. Carria, A. Kaldenbach, M. Bornhöfft, J. Benke, J. Mayer, and M. Wuttig, "Measurement of crystal growth velocity in a melt-quenched phase-change material.," *Nature communications*, **4**, 2371 (2013).
- [129] K. Ohta and H. Ishida, "Matrix formalism for calculation of the light beam intensity in stratified multilayered films, and its use in the analysis of emission spectra," *Applied Optics*, **29**, 2466 (1990).
- [130] W. H. P. Pernice and H. Bhaskaran, "Photonic non-volatile memories using phase change materials," *Applied Physics Letters*, **101**, 171101 (2012).
- [131] L. Huang, J. Callan, E. Glezer, and E. Mazur, "GaAs under Intense Ultrafast Excitation: Response of the Dielectric Function," *Physical Review Letters*, **80**, 185–188 (1998).
- [132] M. S. Dresselhaus, *Solid State Physics Part II: Optical Properties of Solids* (2001).